Doctoral Dissertation

Study on Elastic-Plastic Fracture Mechanics Parameters of 3D Cracks Using the Equivalent Distributed Stress Concept and a Modified Cohesive Zone Model

等価分布応力概念と修正結合力モデルに基づく三次元き裂の弾塑性破壊力学パラメータ決定法に関する研究

ZWE LETYAR HTUT

June 2025

Graduate School of Engineering
The University of Osaka

Doctor of Engineering Dissertation

submitted to

Department of Naval Architecture and Ocean Engineering

Division of Global Architecture

Graduate School of Engineering

The University of Osaka

June 2025

Supervised by

Professor Naoki Osawa

Committee members

Professor Kazuhiro Iijima

- Department of Naval Architecture and Ocean Engineering, Graduate School of Engineering, The University of Osaka

Professor Ninshu Ma

- Department of Joining Mechanics and Analysis, Joining and Welding Research Institute, The University of Osaka

Professor Akira Tatsumi

- Department of Naval Architecture and Ocean Engineering, Graduate School of Engineering, The University of Osaka

ACKNOWLEDGEMENT

First and foremost, I would like to express my deepest gratitude to my supervisor, Professor Naoki Osawa, for his invaluable guidance, encouragement, and unwavering support throughout my doctoral studies at the University of Osaka. His profound knowledge and feedback were instrumental in shaping both the direction and depth of my research. I am truly fortunate to have learned from him, not only as a researcher but also as a mentor.

I am also deeply grateful to Professor Satoyuki Tanaka of Kagoshima University for his kind guidance and thoughtful suggestions. His insights into fracture mechanics and constructive comments greatly contributed to the refinement of this dissertation.

My sincere appreciation goes to Professor Emeritus Masahiro Toyosada of Kyushu University, whose foundational work in elastic-plastic fracture mechanics has been a constant source of inspiration. I especially thank him for valuable discussions that clarified the development of the equivalent distributed stress-based approach in this dissertation.

I would like to extend my heartfelt thanks to all the members of the Osawa Laboratory at the University of Osaka. Their collaboration, stimulating discussions, and generous support made my time in the lab both productive and enjoyable.

I am deeply indebted to my family, my childhood teachers, and the faculty members of Myanmar Maritime University, whose encouragement and support sustained me throughout this journey. Their belief in my goals provided strength during the most challenging moments. In particular, I would like to thank my parents, U Aung Myat Htut and Daw Mu Mu Aye, for their sacrifices and for instilling in me the values of perseverance and curiosity.

I am also profoundly thankful to the Japanese government for awarding me the MEXT scholarship, which enabled me to pursue my doctoral program in Japan. This opportunity would not have been possible without such generous financial support. I am honored to have been a recipient of this prestigious scholarship and remain committed to applying the knowledge and skills gained in service to the global engineering community.

Lastly, sincere thanks are extended to all those who, in various ways, contributed to and supported this endeavor. This dissertation represents not only the outcome of my research but also the collective support and kindness received from many along the way.

Zwe Letyar Htut

ABSTRACT

Ship and offshore structures are constantly exposed to complex cyclic and multiaxial loading throughout their operational life. These demanding conditions often lead to localized plastic deformation, creating a high risk of fatigue crack initiation and propagation. Accurate assessment of crack opening and closure behavior is therefore essential for predicting fatigue crack growth life and maintaining structural integrity.

In the field of elastic-plastic fracture mechanics (EPFM), parameters such as plastic zone size and crack tip opening displacement (CTOD) are key indicators of crack tip behavior. While finite element (FE) analysis has traditionally been used to evaluate these parameters, its computational cost—particularly in fatigue crack propagation (FCP) problems involving numerous cycles—poses significant limitations, especially when tackling complex three-dimensional (3D) crack geometries.

To address these challenges, this study proposes an efficient and accurate method for evaluating EPFM parameters in 3D crack geometries by extending the equivalent distributed stress (EDS) concept originally introduced by Toyosada et al. The EDS method, based on a simplified analytical cohesive zone model (CZM), is adapted to a modified framework suitable for 3D crack analysis. By constructing two-dimensional (2D) substitute crack models that replicate the behavior of 3D cracks, the proposed method achieves computational efficiency without sacrificing accuracy. EDSs are applied to the substitute models to ensure consistency in crack length and stress intensity factor (SIF) between the original 3D geometry and its 2D representations.

Validation is carried out through analytical and numerical FE simulations, demonstrating satisfactory agreement between the EDS-based method and reference solutions in terms of both plastic zone size and CTOD. These results confirm the effectiveness of EDS method to provide a reliable and efficient alternative for analyzing 3D cracks under elastic-plastic conditions. By significantly reducing computational demands, this approach offers a practical tool for structural integrity assessments in marine and offshore engineering applications. The framework established in this study lays the foundation for future integration with FCP analysis, thereby enhancing its utility in the long-term performance evaluation of critical structural components.

***Keywords*:** Equivalent distributed stress; Cohesive zone model; Stress intensity factor; Plastic zone size; Crack tip opening displacement

LIST OF SYMBOLS

Acronyms

CFT	Crack Face Traction
CMOD	Crack Mouth Opening Displacement
COD	Crack Opening Displacement
CT	Compact Tension
CTOD	Crack Tip Opening Displacement
CZM	Cohesive Zone Model
DIC	Digital Image Correlation
EDS	Equivalent Distributed Stress
EPFM	Elastic-Plastic Fracture Mechanics
FCP	Fatigue Crack Propagation
FE	Finite Element
FLM	Fictitious crack face Loading Method
LEFM	Linear Elastic Fracture Mechanics
PFM	Phase-Field Model
PICC	Plasticity-Induced Crack Closure
SENB	Single Edge Notch Bend
SIF	Stress Intensity Factor
SYM	Strip Yield Model
XFEM	Extended Finite Element Method

Greek Symbols

ε_{zz}^{p}	Component of plastic strain in the z-direction ahead of the 3D crack tip
λ	Plastic constraint factor
ν	Poisson's ratio
σ^{P}	External stress (MPa)
σ^{R}	Welding-induced residual stress (MPa)
σ^{Y}	Yield stress of material (MPa)

Roman Symbols

a	Fictitious crack length, or half-length of the 2D substitute crack (mm)
a_1	Fictitious crack length in the depth direction of the target 3D surface crack (mm)
a_2	Fictitious crack length in the width direction of the target 3D surface crack (mm)

c	Physical crack length, or half-length of the 2D substitute crack (mm)
c_1	Physical crack length in the depth direction of the target 3D surface crack (mm)
c_2	Physical crack length in the width direction of the target 3D surface crack (mm)
E	Young's modulus (MPa)
f^P	EDS for the CFT induced by σ^P (MPa)
f^R	EDS for the CFT induced by σ^R (MPa)
f^Y	EDS for the CFT induced by $\lambda\sigma^Y$ (MPa)
K	SIF (MPa mm$^{0.5}$)
K^P_{EDS}	Reproduced SIF by the external stress EDS on the 2D substitute crack (MPa mm$^{0.5}$)
K^P_{Ref}	Reference prescribed SIF of the 3D crack induced by external stress (MPa mm$^{0.5}$)
K^R_{EDS}	Reproduced SIF by the residual stress EDS on the 2D substitute crack (MPa mm$^{0.5}$)
K^R_{Ref}	Reference prescribed SIF of the 3D crack induced by residual stress (MPa mm$^{0.5}$)
K^Y_{EDS}	Reproduced SIF by the cohesive stress EDS on the 2D substitute crack (MPa mm$^{0.5}$)
K^Y_{Ref}	Reference prescribed SIF of the 3D crack induced by cohesive stress (MPa mm$^{0.5}$)
N	Number of spline interpolation divisions
N_a	Number of SIF calculation points
r_p	Plastic zone size (mm)
t^P	CFT induced by σ^P (MPa)
t^R	CFT induced by σ^R (MPa)
t^Y	CFT induced by $\lambda\sigma^Y$ (MPa)
V^P	COD induced by f^P (mm)
V^R	COD induced by f^R (mm)
V^Y	COD induced by f^Y (mm)
V_A	Actual COD in the physical crack region obtained from FE analysis (mm)
V_C	Elastic-plastic COD calculated from the EDS-applied center-through crack (mm)
V_E	Elastic-plastic COD calculated from the EDS-applied edge crack (mm)
V_F	Fictitious COD ahead of the physical crack tip obtained from FE analysis (mm)

LIST OF FIGURES

LIST OF TABLES

TABLE OF CONTENTS

CHAPTER 1

INTRODUCTION

1.1 Background

Engineering structures, particularly those used in demanding environments such as shipbuilding and offshore engineering, are routinely exposed to complex loading conditions throughout their service lives. These conditions often involve cyclic and multiaxial stresses arising from external forces such as waves, wind, current, and operational loads. Over time, repeated application of these stresses can lead to localized plastic deformation in structural components, making them vulnerable to fatigue damage. This fatigue process typically initiates from sites of stress concentration, such as welds, notches, and material imperfections, and may ultimately result in the formation and growth of fatigue cracks. If left unchecked, these cracks can compromise the structural integrity of critical components, leading to serious and sometimes catastrophic failures.

Ensuring the structural integrity of ship and offshore structures is of paramount importance, not only to protect human lives but also to avoid severe environmental and economic consequences. Famous historical examples highlight the significance of understanding and managing fatigue behavior in large-scale structures. One notable case is the failure of the Liberty ships during World War II [1]. These cargo vessels, mass-produced to support wartime logistics, experienced unexpected brittle fractures, many of which were initiated from small cracks at welded joints under cyclic loading conditions. Another landmark event is the collapse of the Alexander L. Kielland offshore platform in 1980, which tragically resulted in the loss of 123 lives [2]. Investigations revealed that a fatigue crack, originating from a faulty weld, propagated under cyclic wave loading and ultimately caused the catastrophic failure of one of the platform's legs.

Such incidents highlight the critical role of fracture mechanics and fatigue crack growth analysis in ensuring the safety and reliability of large-scale marine structures. However, accurately predicting fatigue crack growth in ship and offshore structures remains particularly challenging due to the variable amplitude loading experienced in corrosive marine environments. Inaccurate estimation of crack propagation rates can lead to improper maintenance scheduling or unexpected structural failures, both carrying serious consequences.

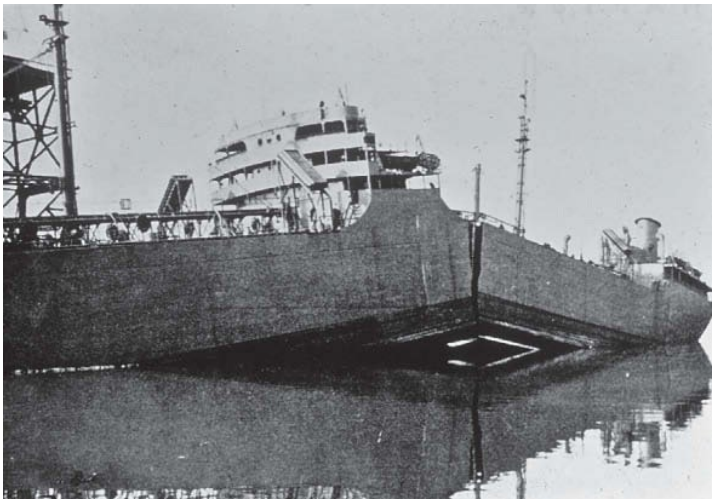

Fig. 1.1 The SS Schenectady, a Liberty ship, fractured due to brittle failure while docked in harbor, 1943 [1]

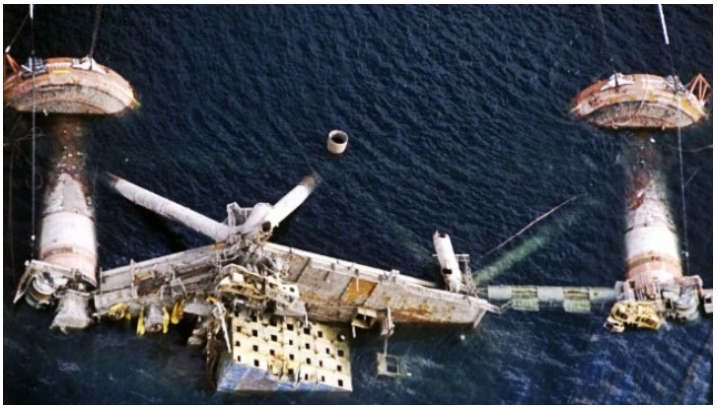

Fig. 1.2 Alexander L. Kielland offshore platform capsize accident, 1980 [2]

Given these evolving challenges, the need for accurate assessment and deeper understanding of fracture mechanics parameters has never been more critical. Reliable evaluation of these parameters is essential for predicting fatigue crack growth and directly supports the development of effective design, inspection, and maintenance strategies. The historical failures of the Liberty ships and the Alexander L. Kielland platform serve as enduring reminders of the catastrophic consequences associated with inadequate fatigue management.

As marine structures continue to grow in complexity and face more aggressive service environments, advancing fracture mechanics methodologies, particularly in the areas of crack growth evaluation, fatigue life prediction, and fracture parameter estimation, remains a vital research priority. These efforts contribute significantly toward ensuring safer, more reliable, and economically viable engineering solutions for the marine industry.

1.2 History and Overview of Fracture Mechanics

Fracture mechanics has evolved as a fundamental discipline for understanding how materials and structures fail under various loading conditions. Originating from early theoretical models in the early 20th century, the field has expanded significantly through successive decades, driven by both scientific advances and the demands of engineering practice. Early contributions provided the foundation for quantifying crack behavior, while post-war research introduced critical modifications that connected theoretical models with real-world observations. Subsequent developments from the 1960s onward have refined the understanding of crack growth, material toughness, and fatigue under increasingly complex loading scenarios. Today, fracture mechanics continues to evolve, incorporating advanced computational methods, new materials, and multidisciplinary approaches. This section provides a historical overview of key developments in fracture mechanics, organized by major periods of research progress.

1.2.1 Early Foundations of Fracture Theory

Initial experimental insights into the fracture behavior of materials can be traced back to Leonardo da Vinci, who, several centuries earlier, observed that the tensile strength of iron wires decreased with increasing wire length [3]. This empirical observation suggested a flaw-controlled mechanism of failure, where larger specimens inherently possessed a higher probability of containing critical flaws. Although da Vinci's findings were qualitative, they hinted at the fundamental role of material imperfections in governing mechanical strength.

A quantitative framework was first established by Inglis in 1913 [4], who performed a stress analysis for an elliptical hole in a plate subjected to tension, demonstrating that sharp flaws create localized stress concentrations significantly greater than the nominal applied stress. Building upon this foundation, Griffith in 1920 [5] proposed the first energy-based fracture theory, developing a fracture criterion based on the first law of thermodynamics. According to Griffith's model, crack propagation becomes unstable when the decrease in elastic strain energy resulting from an incremental crack extension exceeds the surface energy required to create new free surfaces.

Griffith energy balance approach successfully explained the observed inverse relationship between flaw size and tensile strength in brittle materials such as glass.

However, the model inherently assumed that fracture resistance derived exclusively from the material's surface energy, thereby limiting its applicability to ideally brittle solids. Efforts to apply the Griffith theory to ductile materials, such as metals, were unsuccessful due to the absence of plastic deformation mechanisms in the original formulation. Significant theoretical advancements were not introduced until 1948, when modifications to Griffith's framework incorporated plastic energy dissipation, thereby enabling a more accurate description of fracture behavior in metallic systems.

1.2.2 Evolution of Fracture Mechanics after World War II

Following the widespread failures of Liberty ships during World War II, fracture mechanics evolved from a scientific curiosity into an essential engineering discipline. Dr. Irwin, leading the research group at the US Naval Research Laboratory, extended Griffith's 1920 fracture model by incorporating the energy dissipated through local plastic deformation in metals [6], an idea also independently proposed by Orowan [7] and Mott [8] further refined the theoretical framework by addressing rapidly propagating cracks.

In 1956, Irwin [9] introduced the energy release rate, a reformulation of Griffith's theory suited for practical engineering applications. Drawing on Westergaard's 1938 analytical solutions for sharp cracks [10], Irwin established that near-tip stresses and displacements could be characterized by a single parameter, later known as the stress intensity factor, SIF [11]. Williams independently derived similar crack-tip solutions using a different approach [12].

Early successful applications reinforced the value of fracture mechanics. In 1956, Wells [13] employed fracture mechanics to explain the catastrophic fuselage failures of the Comet aircraft, attributing them to fatigue cracks initiated at poorly reinforced, square-cornered windows. In 1957, Winne and Wundt [14] utilized Irwin's energy release rate method to predict and prevent the failure of large steam turbine rotors at General Electric Corporation.

Despite early successes, fracture mechanics initially faced resistance within parts of government and industry. In 1960, Paris and his colleagues [15] proposed a fracture mechanics-based model for fatigue crack growth, challenging the prevailing S–N curve approach and marking a pivotal advancement in fatigue analysis.

1.2.3 Development of Fracture Mechanics: 1960–1980

Following World War II, fracture mechanics evolved rapidly, particularly between 1960 and 1980, when researchers addressed limitations of linear elastic fracture mechanics (LEFM) under significant plastic deformation. Irwin [16], Dugdale [17], and Barenblatt [18] introduced corrections for crack-tip plasticity, while Wells [19] proposed the CTOD as a new fracture parameter for ductile materials.

Rice [20] developed the *J*-integral to characterize nonlinear material behavior, building on Eshelby's earlier conservation integrals [21]. Hutchinson [22], and Rice and Rosengren [23] further related the *J*-integral to crack-tip stress fields, establishing it as both an energy release rate and a nonlinear stress-intensity parameter.

The nuclear power industry's interest in fracture toughness during the 1970s accelerated the adoption of *J*-integral methods. In 1971, Begley and Landes [24] successfully applied the *J*-integral to characterize nuclear pressure vessel steels, which led to the publication of standardized *J*-testing procedures a decade later (ASTM E813, 1981) [25]. Shih and Hutchinson [26] later provided a theoretical framework for fracture design based on the *J*-integral, which was formalized in the Electrical Power Research Institute fracture handbook [27].

In parallel, the UK advanced CTOD methodology for welded structures, driven by North Sea oil developments. Burdekin and Dawes [28] introduced the CTOD design curve, while UK nuclear industries developed fracture assessments based on strip yield models (SYMs). Shih [29] demonstrated the relationship between the *J*-integral and CTOD, leading to a convergence of US and UK approaches. Today, both parameters are widely used to characterize fracture behavior in various materials. Much of the theoretical foundation of dynamic fracture mechanics was laid during this period.

1.2.4 Advancements in Fracture Mechanics: 1980–Present

Since 1980, fracture mechanics has expanded significantly, driven by the demand for safer, more reliable structures across industries such as aerospace, nuclear power, transportation, and offshore engineering. Advances have been made in both theoretical development and practical applications, extending fracture mechanics beyond traditional metals to composites, polymers, and advanced ceramics.

EPFM has been further refined, with widespread adoption of *J*-integral and CTOD approaches for characterizing fracture toughness across a wide range of materials. Testing standards, such as ASTM E1820, were established to formalize procedures for measuring *J*-integral and CTOD, enhancing consistency and reliability in material qualification [30].

Recent research trends include the development of microstructural fracture models and frameworks that relate local fracture processes to global material behavior. Closely related are efforts to characterize and predict the geometry dependence of fracture toughness—an important consideration when conventional, single-parameter fracture mechanics approaches prove insufficient.

The development of computational fracture mechanics, especially FE methods with fracture criteria, enabled detailed simulations of crack initiation and propagation in complex structures [31]. Extended finite element method (XFEM) [32] and phase-field models (PFMs) have been introduced to simulate fracture processes without requiring predefined crack paths [33,34].

With the emergence of advanced materials such as fiber-reinforced composites and nanomaterials, new fracture mechanics concepts have been necessary. Multiscale modeling approaches have been developed to bridge material behavior from the atomic scale to the structural scale [35].

Structural integrity assessments have also evolved, supported by guidelines like the R6 procedure in the UK and the ASME Boiler and Pressure Vessel Code in the US [36]. These frameworks integrate fracture mechanics with probabilistic approaches to account for uncertainties in material properties, loading, and flaw detection.

Today, fracture mechanics continues to play a central role in the design, assessment, and life-extension of critical structures. The integration of machine learning and data-driven approaches with traditional fracture mechanics analysis is an emerging trend, promising further improvements in prediction accuracy and decision-making for structural safety [37,38].

1.3 Development of Fracture Mechanics Frameworks

As fracture mechanics evolved from its early foundations through the post-war period and into modern applications, it became evident that a systematic framework was

necessary to characterize and predict crack initiation and growth across a wide range of materials and loading conditions. Early developments were largely based on linear elastic assumptions, which provided a fundamental understanding of brittle fracture but proved insufficient when addressing the behavior of more ductile materials that exhibit significant plastic deformation at crack tips.

The growing demand for safer and more reliable structures, coupled with the use of increasingly diverse materials, highlighted the limitations of purely linear elastic approaches. Consequently, the discipline expanded to incorporate plasticity effects, leading to the establishment of EPFM alongside traditional LEFM. The primary distinction between these frameworks lies in the development of plastic deformation around the crack tip during the fracture process, as illustrated in **Fig. 1.3**.

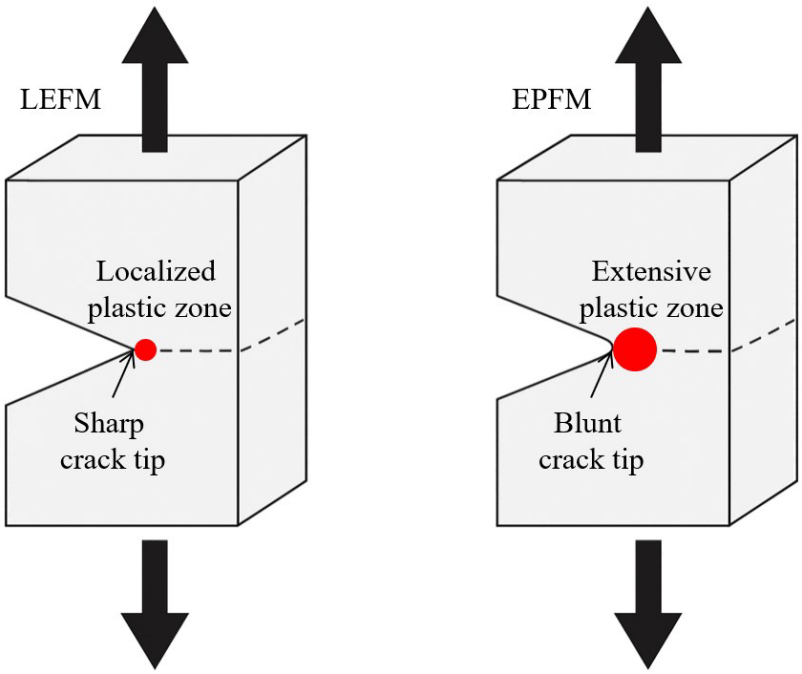

Fig. 1.3 Schematic illustration of crack-tip plastic deformation fields under LEFM and EPFM conditions

These two frameworks now form the foundation of modern fracture mechanics, providing critical tools for evaluating structural integrity under both brittle and ductile fracture conditions.

The following subsections provide a detailed discussion of the principles, assumptions, and parameters associated with LEFM and EPFM.

1.3.1 Linear Elastic Fracture Mechanics

LEFM provides the foundational framework for analyzing crack initiation and propagation under the assumption that the material remains linearly elastic up to fracture. This approach is particularly well-suited for brittle materials or situations where plastic deformation is confined to a very small region near the crack tip and can be neglected in the overall structural response.

The primary parameter governing fracture in LEFM is the SIF, K, which characterizes the intensity of the stress field near the crack tip. When K reaches a critical value, known as the fracture toughness K_{IC}, rapid crack propagation occurs, leading to structural failure. LEFM also assumes that the stress and displacement fields near the crack tip exhibit a singular behavior, following an inverse square root dependence on the distance from the crack tip.

Classical solutions developed within the LEFM framework, such as those by Irwin [9] and Westergaard [10], have provided powerful tools for assessing structural integrity and designing against fracture in various engineering applications. However, as materials with higher ductility and structures subjected to complex loading became more common, the limitations of LEFM became increasingly apparent. In particular, LEFM does not adequately capture the effects of plastic deformation at the crack tip. Moreover, it may not be valid for fatigue crack growth when plasticity-induced crack closure (PICC) significantly affects propagation behavior [39].

As a result, for materials and conditions where plasticity plays a non-negligible role, an extended framework capable of addressing these phenomena was necessary. This need led to the development of EPFM.

1.3.2 Elastic-Plastic Fracture Mechanics

EPFM extends the principles of fracture mechanics into the regime where the assumptions of linear elasticity no longer hold. Unlike LEFM, where the crack tip is modeled as an idealized sharp point with an associated stress singularity, EPFM recognizes that plastic deformation occurs ahead of the crack tip, leading to blunting and redistribution of the stress and strain fields. This plasticity substantially influences crack growth behavior, making linear elastic models insufficient for accurately predicting fracture in ductile materials or under large-scale yielding conditions.

The development of EPFM has been critical for enabling the safe design and evaluation of structures operating under more demanding environments, where higher loads, PICC, complex geometries, and ductile materials are often encountered. By incorporating the effects of plastic deformation, EPFM provides a more comprehensive framework for assessing fracture processes across a wide range of engineering applications.

Within EPFM, several specialized parameters have been formulated to characterize crack initiation and propagation under elastic-plastic conditions. These parameters serve as the foundation for evaluating fracture behavior when plasticity cannot be neglected. The following section introduces and discusses the key parameters utilized in EPFM, which are essential for quantifying the effects of nonlinear material behavior on crack growth.

1.4 Key EPFM Parameters

As discussed in the previous section, EPFM provides the framework necessary to evaluate fracture behavior in materials where significant plastic deformation occurs at the crack tip. Central to EPFM are parameters that quantitatively characterize the crack driving forces and resistance mechanisms under elastic-plastic conditions. Among these, the plastic zone size, the CTOD, and the *J*-integral are of particular importance.

Each parameter captures a different aspect of the complex stress and strain fields near the crack tip. The plastic zone size quantifies the extent of plasticity influencing crack propagation, CTOD provides a physical measure of crack tip deformation, and *J*-integral offers an energy-based perspective. A thorough understanding of these parameters is essential not only for accurate fracture assessments but also for the development of advanced evaluation methods.

1.4.1 Plastic Zone Size

When a crack is present in a ductile material, the region near the crack tip experiences very high stress levels, often exceeding the material's yield strength. As a result, a zone of plastic deformation—referred to as the plastic zone—forms around the crack tip as illustrated in **Fig. 1.4**. The size and shape of this plastic zone play a crucial role in determining the material's fracture behavior, especially under elastic-plastic conditions.

The plastic zone is influenced by several factors, including the applied load, material properties, and the stress state around the crack tip. Under plane stress conditions, which are

typical of thin specimens, the plastic zone tends to be larger and more spread out. In contrast, under plane strain conditions, which dominate in thicker materials, the plastic zone is smaller and more confined. This difference significantly affects the material's apparent toughness and the development of crack tip fields.

Understanding the plastic zone size is important because it reflects how much energy is being absorbed through plastic deformation, and it helps determine the applicability of fracture models. If the plastic zone is small relative to the crack size and specimen dimensions, LEFM may be sufficient. However, when the plastic zone becomes large, EPFM must be employed.

The plastic zone also provides valuable insight into crack tip shielding, crack blunting, and material toughening mechanisms, all of which can contribute to increased fracture resistance. Accurate estimation of the plastic zone size is vital for numerical simulations and for the design of damage-tolerant structures.

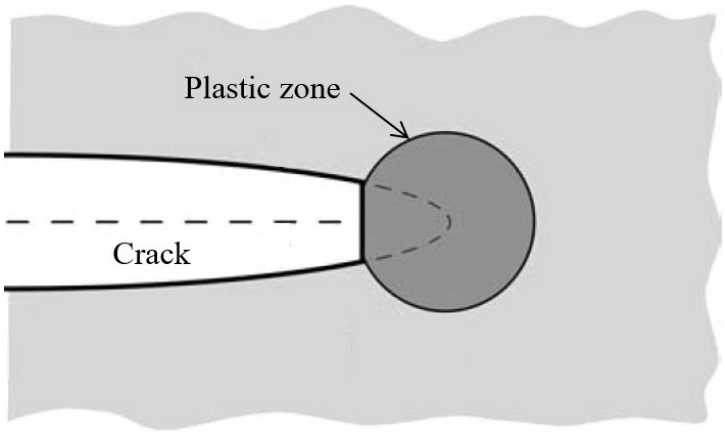

Fig. 1.4 Illustration of plastic zone at the crack tip [3]

1.4.2 Crack Tip Opening Displacement

CTOD plays a pivotal role in characterizing the deformation behavior of ductile materials. It provides a direct and physical measure of the displacement at the crack tip, offering clear insight into the local response of a material as it transitions from stable deformation to fracture.

Historically, the concept of CTOD was introduced in the early 1960s by Wells [19], who observed that ductile materials exhibit a consistent opening displacement at the crack tip just before fracture. His experiments on mild steel demonstrated that even under

significant plastic deformation, the amount of opening at the crack tip remained nearly constant at the onset of crack propagation. This observation laid the groundwork for CTOD as a fracture criterion, particularly effective for materials where plasticity plays a dominant role.

CTOD is defined as the displacement between the upper and lower crack surfaces at a specified point near the crack tip, typically at the original crack tip location and the 90 deg intercept as illustrated in **Fig. 1.5**. It captures the amount of opening induced by applied loads, reflecting the material's resistance to crack growth in the presence of plastic deformation.

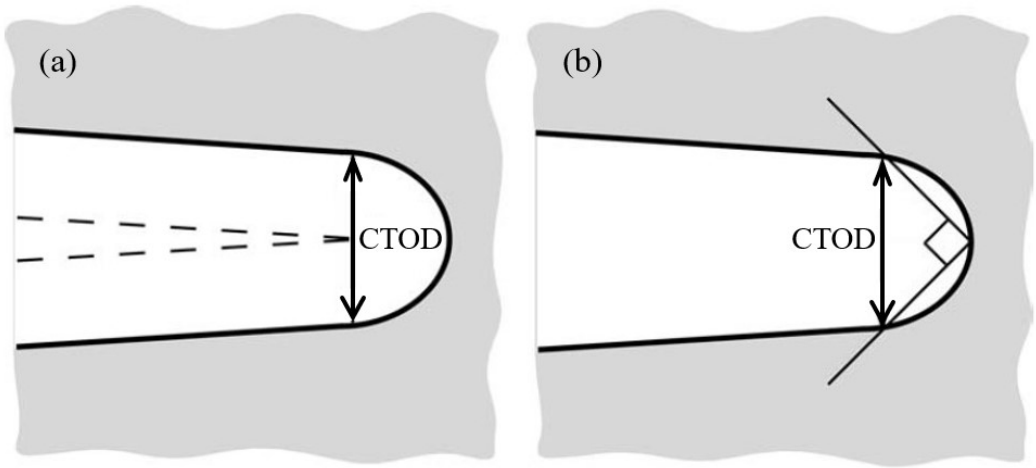

Fig. 1.5 Schematic definitions of CTOD: **(a)** displacement at the original crack tip; **(b)** displacement at the intersection of a 90 deg vertex drawn between the crack flanks [3]

There are several methods to experimentally determine CTOD, depending on the geometry and loading conditions of the specimen:

- **Direct Measurement:** Using high-resolution extensometers or digital image correlation (DIC), the opening displacement at the crack tip can be measured directly during testing. This method is common in standardized fracture toughness tests such as the BS7448 for metallic materials [40].
- **Clip Gauge Method:** In single edge notch bend (SENB) or compact tension (CT) specimens, clip gauges attached at the crack mouth measure the crack mouth opening displacement (CMOD), from which CTOD can be inferred through geometry-based calibration relationships [41].

- **Numerical Estimation:** FE analysis is frequently used to determine CTOD from simulated stress and displacement fields, especially in cases where direct measurement is impractical [42].

A simplified but insightful method to estimate CTOD is through the SYM, originally developed by Dugdale [17] and later extended by others. This model idealizes plastic deformation at the crack tip as a narrow zone of yielded material (the strip) extending ahead of the crack in an otherwise elastic medium. The size of the strip-yield zone, or plastic zone, is defined by the requirement of finite stresses at the crack tip. CTOD can be defined as the opening displacement at the end of the strip-yield zone. Thus, the SYM provides a means to estimate both CTOD and the plastic zone size. A detailed discussion of this model is presented in **Section 2.1.3** of **Chapter 2**.

1.4.3 J-Integral

In 1968, Rice [20] considered the changes in potential energy associated with crack growth in nonlinear elastic materials, recognizing that such behavior could realistically approximate plastic deformation as long as no unloading occurred. Through this work, Rice derived a fracture parameter known as the *J*-integral, a contour integral that can be evaluated along any arbitrary path enclosing the crack tip, as illustrated in **Fig. 1.6** [3]. He demonstrated that the *J*-integral is equivalent to the energy release rate for a crack in nonlinear elastic material.

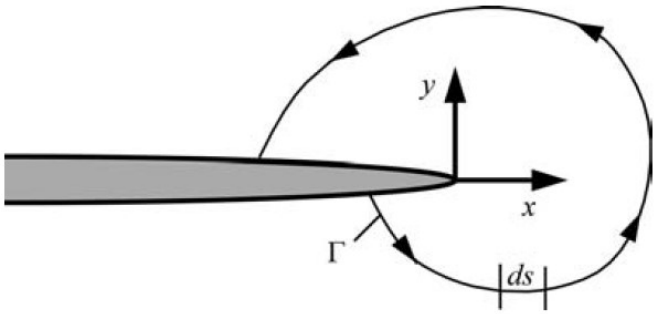

Fig. 1.6 Arbitrary contour path enclosing the crack tip in non-linear elastic material [3]

Building on this foundation, the *J*-integral has become a fundamental parameter in EPFM. It characterizes the intensity of the stress and strain fields near a crack tip under elastic-plastic conditions, extending the concept of crack driving force beyond the limits of linear elasticity. Defined as the energy release rate per unit crack extension, the *J*-integral provides a generalized and powerful measure of the fracture driving force.

Mathematically, the *J*-integral is expressed as:

$$J = \int_{\Gamma} \left(w dy - T_i \frac{\partial u_i}{\partial x} ds \right) \tag{1.1}$$

where Γ is a contour around the crack tip, w is the strain energy density, T_i is the traction vector, u_i is the displacement vector, and s is the arc length along the contour.

One of the major advantages of the *J*-integral is its path-independence under conditions of monotonic loading and absence of crack tip plastic instability, allowing it to be evaluated on contours remote from the crack tip where numerical solutions are more stable. The *J*-integral thus forms the basis for many fracture toughness tests and crack growth criteria in elastic-plastic materials.

However, while the *J*-integral effectively captures the global energy-based characteristics of crack propagation, it does not directly account for the localized deformation and crack opening behavior critical to understanding crack initiation. Therefore, this thesis focuses on physical parameters, particularly plastic zone size and CTOD, which provide more localized insight essential for advancing fracture assessments of complex 3D crack geometries, a task that remains a significant challenge in EPFM.

1.5 Existing Methods and Challenges in Evaluating EPFM Parameters

Plastic zone size and CTOD are widely recognized as key parameters in EPFM, particularly in studies related to PICC and FCP [43–48]. Conventionally, these parameters are evaluated through numerical fracture mechanics analyses, often employing FE methods. While FE analysis provides a straightforward and comprehensive approach, it becomes computationally impractical for FCP problems involving numerous loading cycles, where repeated mesh updates are required. Consequently, despite its accuracy, FE analysis faces significant limitations in practical applications, particularly for evaluating EPFM parameters of 3D crack geometries. This challenge has led to increasing demand for faster and more efficient alternative methods.

In response to such needs, Newman [49,50] developed the fatigue crack growth analysis program FASTRAN, based on the concept of PICC. This program utilizes a 2D analytical SYM, originally derived from the Dugdale model [17] but modified to leave plastically deformed material in the wake of the advancing crack. By superimposing two

elastic problems—one involving a cracked plate under remote uniform stress, and the other involving the same cracked plate subjected to a uniform stress distributed over a segment of the crack surface—the plastic zone size and crack face displacements can be estimated. Newman's SYM has since become one of the most influential analytical frameworks for crack closure and FCP analysis. However, the extension of this model to 3D crack geometries and complex loading conditions remains limited, as it has not been fully validated for such cases. The effectiveness of SYM in accurately addressing complex stress fields and crack propagation behavior of 3D cracks continues to be an open issue, necessitating further research and validation.

In parallel with SYM developments, PFMs have also gained significant attention in fracture mechanics due to their ability to model complex crack propagation without requiring explicit crack tracking [51–53]. PFMs offer significant advantages, such as capturing evolving crack patterns, handling multiple interacting fractures, and providing smooth crack interface representations. However, these models are computationally intensive and typically require fine mesh discretization, which limit their feasibility for large-scale or industrial FCP applications [54,55]. Although recent advancements, such as adaptive mesh refinement techniques and improved energy formulations, have enhanced the computational efficiency of PFMs [56–58], a substantial gap remains between academic research and practical implementation. Notably, no widely available PFM-based FCP analysis code currently exists that could be easily utilized by practicing engineers for fatigue design purposes. Consequently, despite their promise, PFMs have not yet supplanted simpler and more practical methods like SYM in engineering practice, especially where computational simplicity and ease of use are essential.

Efforts have also been made to extend numerical approaches to 3D crack problems. Kelly and Nowell [59] proposed a general method for determining the plastic zone size of cracks in 3D bodies, employing a Dugdale-type penny-shaped crack model. Their approach uses an eigenstrain method, discretizing the elastic and plastic regions into triangular elements to calculate stresses induced by specified crack surface displacements. However, the accuracy of this method heavily depends on the refinement of the mesh, and oscillations may occur in the computed crack opening displacement (COD) profiles, posing challenges for practical applications.

Building further upon SYM concepts, Yamashita and Gotoh [60] investigated PICC, and evaluated elastic-plastic COD profiles of 3D surface cracks by incorporating weight

function methods [61,62] into the SYM framework. Although their method provided improvements in estimating EPFM parameters for 3D cracks, a major challenge remains: the development of SYMs applicable to arbitrary 3D crack shapes requires the derivation and application of corresponding original 3D weight functions, a task that is mathematically complex and practically demanding.

In response to these challenges, the EDS approach was introduced by Toyosada and Niwa [63], based on the Dugdale model and the SYM concept, as a computationally efficient and physically interpretable alternative. The EDS method transforms a complex crack geometry into an equivalent 2D crack by applying a fictitious crack face traction (CFT), thereby preserving the same SIF characteristics. This enables the analysis of EPFM parameters, such as plastic zone size and CTOD, without requiring complex remeshing or full-field stress calculations. Moreover, this method lends itself well to analytical and semi-analytical formulations, which are particularly advantageous when dealing with fatigue analysis involving repetitive crack extension. Unlike FE or PFM approaches that demand extensive numerical effort, EDS can offer rapid estimations of key EPFM parameters with accuracy sufficient for practical design and safety assessments. Furthermore, its theoretical foundation based on fictitious CFT enables straightforward extension to different loading conditions and geometries, provided that the corresponding SIF relationships can be obtained or approximated.

However, existing EDS-based studies have primarily focused on simple 2D geometries [64]. For the EDS concept to be utilized effectively in real-world engineering applications, it must be generalized to accommodate arbitrary 3D crack shapes and validated against reliable reference solutions. This gap presents both a challenge and an opportunity: by extending the EDS methodology to 3D crack configurations, the method could serve as a powerful alternative to traditional fracture mechanics approaches, particularly in contexts where efficiency, interpretability, and adaptability are essential.

Accordingly, this dissertation is driven by the aim of enhancing the applicability of the EDS method to 3D crack geometries and to integrate it into a broader framework for EPFM analysis. The specific objectives and structure of this research are outlined in the following sections.

1.6 Objectives of Research

As discussed in the preceding section, while several methods—ranging from FE analysis to analytical models like SYM and emerging approaches such as PFMs—have contributed to the evaluation of EPFM parameters, significant challenges persist, particularly for practical applications involving 3D crack geometries under elastic-plastic conditions. Existing methods either suffer from prohibitive computational demands, are limited to specific idealized crack shapes, or require complex mathematical formulations that hinder their widespread adoption in engineering practice.

The primary objective of this research is to develop a practical, efficient, and accurate method for evaluating EPFM parameters of 3D cracks by extending the EDS framework. Building on the promising results demonstrated for 2D crack problems, this study seeks to generalize the EDS approach to more complex 3D crack configurations, where conventional methods face substantial limitations.

Specifically, the goals of this research are:

- **To establish a theoretical formulation** for applying the EDS method to 3D cracks, ensuring that essential fracture parameters such as plastic zone size and CTOD can be accurately estimated while maintaining computational efficiency.
- **To develop a practical computational procedure** for determining the EDS distribution for 3D cracks, including the adaptation of iterative schemes for reproducing the crack length–SIF relationships under elastic-plastic conditions.
- **To validate the proposed EDS-based method** by comparing its predictions of key EPFM parameters with high-fidelity FE solutions and available reference data for representative 3D crack configurations.

While the current scope focuses on establishing and validating the EDS approach for the efficient evaluation of EPFM parameters, its extension to FCP problems is identified as a future direction. The outcomes of this research are expected to contribute a new analytical framework to the field of EPFM, bridging the gap between computationally intensive numerical simulations and simplified analytical models, and offering practical value for engineering applications involving complex 3D crack problems.

1.7 Structure and Overview of the Dissertation

This dissertation is organized into six chapters, systematically presenting theoretical development, numerical formulation, and verification of the EDS method for evaluating EPFM parameters in 3D cracked bodies.

- **Chapter 1** introduces the background and motivation of the study, reviews the historical development of fracture mechanics, and outlines the limitations of existing EPFM methods. The research objectives are defined in the context of extending the EDS framework to 3D crack problems.
- **Chapter 2** establishes theoretical groundwork by introducing key principles such as the superposition principle, the weight function method, and the Dugdale CZM. The concept of EDS is formulated in detail, including the explanation of three distinct loading methods within the EDS framework. The advantages and limitations of each method are discussed. Additionally, this chapter introduces weight functions for 2D substitute crack models (center-through and edge cracks), which are fundamental for constructing the EDS representation in 3D analysis.
- **Chapter 3** details the development of the EDS-based analysis method using the fictitious crack face loading method. It outlines the procedures for determining the EDS distribution through spline interpolation and generalized matrix inversion. A CZM formulated within the EDS framework is also introduced, and an integrated EDS-based fracture mechanics analysis system is constructed.
- **Chapter 4** presents the validation of the proposed EDS-based EPFM analysis system for 3D cracks. A 3D penny-shaped crack in an infinite plate under axisymmetric loading is selected as a verification case due to its simple geometry and the availability of an analytical weight function. This chapter demonstrates the EDS analysis procedures in detail and verifies its accuracy in estimating elastic-plastic COD profiles, as well as in comparing key EPFM parameters—plastic zone size and CTOD—with existing analytical solutions.
- **Chapter 5** extends the EDS methodology to semi-elliptical surface cracks, which are commonly encountered in engineering structural components. An idealized plastic zone model is adopted to establish consistent reference crack length–SIF (a–K) relationships for the target 3D cracks. High-precision numerical integration is incorporated into the open-source FE code WARP3D for accurate SIF evaluation.

Based on FE simulations, this chapter determines reference solutions and evaluates EDS distributions and corresponding EPFM parameters at key locations along the crack front—specifically, the deepest and corner points—demonstrating the method's applicability to non-axisymmetric 3D crack geometries.

- **Chapter 6** summarizes the main contributions of the research, confirms the validity and advantages of the proposed method, and discusses directions for future work, including the potential application of the EDS framework to FCP analysis.

Together, these chapters establish a comprehensive framework for analyzing 3D cracks under elastic-plastic conditions using the EDS approach, delivering both theoretical foundations and practical guidance for engineering applications.

CHAPTER 2

THEORETICAL BACKGROUND

2.1 Basic Principles

This chapter presents the theoretical background essential for understanding the framework of the present study. It begins by reviewing fundamental principles employed in the EDS method, including the superposition principle, the weight function approach, and the Dugdale CZM. These concepts provide the foundation for analyzing crack behavior and evaluating SIFs in elastic and elastic-plastic materials. Building upon these basic principles, the concept of EDS is then introduced. The EDS method serves as the core analytical tool in this study, offering a means to represent the crack opening behavior of 3D cracks in a simplified yet effective manner. Through this theoretical foundation, the subsequent chapters will develop and apply the EDS-based methodology to address the objectives of the research.

2.1.1 Superposition Principle

The superposition principle is a fundamental concept in LEFM. It states that the response of a linear elastic system to multiple loads can be obtained by summing the individual responses caused by each load acting separately. This principle greatly facilitates the analysis of SIFs in cracked bodies by allowing complex problems to be decomposed into simpler, more manageable subproblems.

To illustrate the application of the superposition principle in the present study, consider first an isotropic elastic uncracked body subjected to a remote stress distribution $\sigma^P(x)$. When $\sigma^P(x)$ is applied, it induces an internal traction distribution $t^P(x)$ along the plane corresponding to the would-be crack face, indicated by the dotted line in **Fig. 2.1(a)**. Analysis of the stresses along this dotted line reveals that the internal tractions $t^P(x)$ are equal in magnitude to the applied remote stress $\sigma^P(x)$.

In order to create a stress-free condition along the dotted line, opposing stresses of magnitude $\sigma^P(x)$ must be applied along the dotted line, as shown in **Fig. 2.1(b)**. The stresses induced by the remote loading $\sigma^P(x)$ along the dotted line are referred to as the opening stresses $t^P(x)$, while the opposing stresses applied to cancel them out are termed the crack closing stresses, denoted as $-t^P(x)$. It is important to note that the opening stresses $t^P(x)$

generated by the remote loading lead to a crack opening condition and contribute directly to a nonzero SIF.

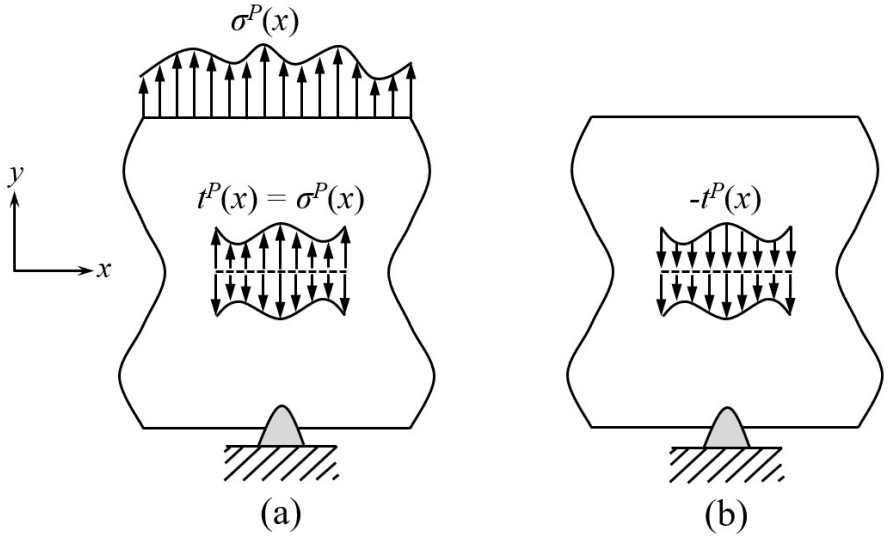

Fig. 2.1 An isotropic elastic uncracked body: **(a)** remote stress $\sigma^P(x)$ inducing internal opening tractions $t^P(x)$; **(b)** closing tractions $-t^P(x)$

Now, consider an isotropic elastic cracked body subjected to a remote stress $\sigma^P(x)$, as shown in **Fig. 2.2(a)**. According to the superposition principle, this configuration can be decomposed into two subproblems, as illustrated in **Fig. 2.2(b)** and **(c)**.

- One configuration consists of the crack subjected solely to the opening tractions $t^P(x)$ (**Fig. 2.2(b)**).
- The other configuration consists of the crack subjected to the remote stress $\sigma^P(x)$ together with the closing tractions $-t^P(x)$ (**Fig. 2.2(c)**).

In the latter case (**Fig. 2.2(c)**), the applied remote stresses and the closing tractions cancel each other out along the crack surfaces, resulting in a clamped crack with no crack opening. Consequently, the SIF for this configuration is zero. Mathematically, this can be expressed as:

$$K_{(a)} = K_{(b)} + K_{(c)} \tag{2.1}$$

which reduces to

$$K_{(a)} = K_{(b)} + 0 \tag{2.2}$$

Therefore, the SIF for the cracked body under the remote stress $\sigma^P(x)$ (**Fig. 2.2(a)**) is equal to that for the crack subjected only to the opening tractions $t^P(x)$ (**Fig. 2.2(b)**). i.e.,

$$K_{(a)} = K_{(b)} \tag{2.3}$$

This decomposition enables a more tractable analysis by isolating the effects of internal tractions and external loads separately. The approach is particularly effective when combined with the weight function method, providing an efficient means for calculating SIFs for arbitrary stress distributions.

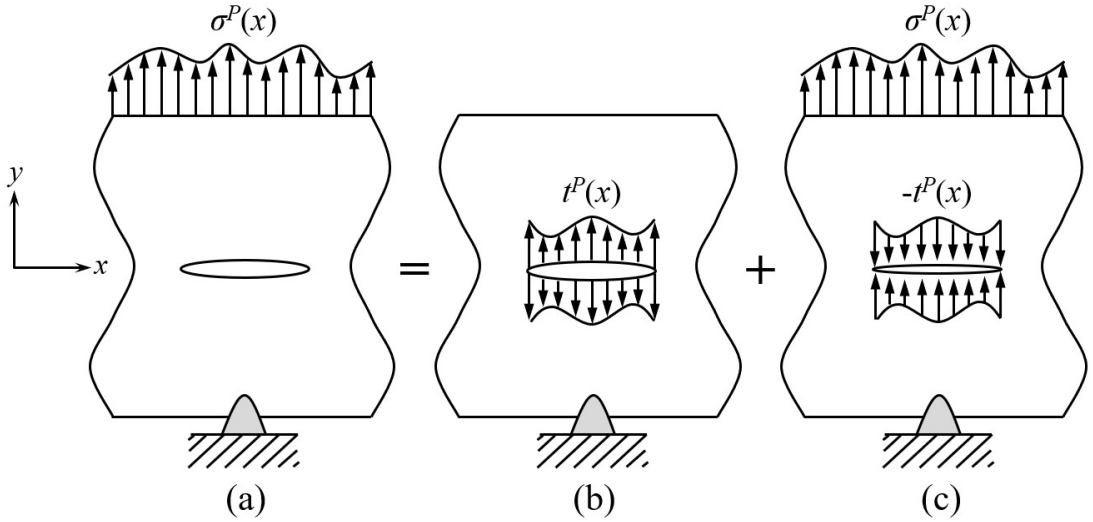

Fig. 2.2 Superposition principle: **(a)** crack under remote stress $\sigma^P(x)$; **(b)** crack under opening tractions $t^P(x)$; **(c)** crack under remote stress $\sigma^P(x)$ and closing tractions $-t^P(x)$

2.1.2 Weight Function Approach

The weight function approach is a widely used method in fracture mechanics for calculating SIFs under arbitrary stress distributions without directly solving complex boundary value problems. A weight function is defined as a fundamental solution that characterizes how a unit load applied along the crack surface contributes to SIF. Once the weight function is known for a given crack geometry and boundary condition, the SIF under any applied stress can be obtained by a simple integration.

For example, consider an edge-cracked elastic body with a crack length a. The SIF resulting from a unit force applied at a point x, as shown in **Fig. 2.3(a)**, can be interpreted as the weight function $g(x,a)$. When a distributed traction stress $t(x)$ is applied along the crack faces, as illustrated in **Fig. 2.3(b)**, the corresponding SIF, K, can be mathematically expressed as:

$$K = \int_{x=0}^{a} t(x)g(x,a)dx \tag{2.4}$$

A graphical representation of the weight function approach is shown in **Fig. 2.3(c)**, where the area under the curve of $t(x)g(x,a)$ corresponds to the resulting SIF, K.

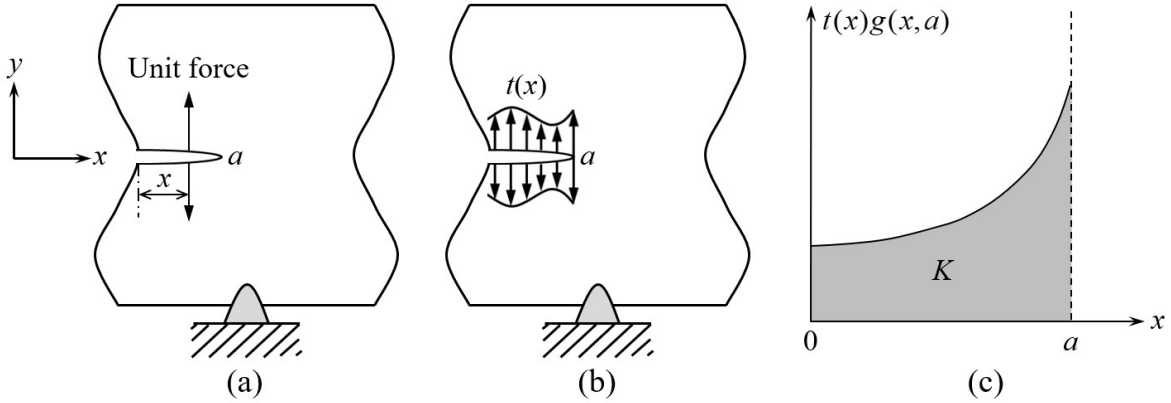

Fig. 2.3 Concept of the weight function approach: **(a)** unit force applied at position x defining the weight function $g(x,a)$; **(b)** distributed traction stress $t(x)$ applied along the crack faces; **(c)** graphical representation of SIF, K as the area under the curve $t(x)g(x,a)$

The weight function depends solely on the geometry of the cracked body and the crack configuration, and is independent of the specific external loading. Thus, once determined, it offers an efficient and flexible means of evaluating SIFs for various loading conditions through straightforward integration. However, as discussed in **Section 1.5**, the evaluation of SIFs in the development of 3D SYMs using their corresponding 3D weight functions remains mathematically complex and practically challenging.

In the present study, the weight function approach is employed to calculate the equivalent SIFs of 3D cracks via 2D substitute crack bodies, forming a foundation for the development of the EDS method.

2.1.3 Dugdale Cohesive Zone Model

The Dugdale CZM, introduced in 1960 [17], is a foundational approach for describing crack tip behavior in ductile materials. It addresses a key limitation of LEFM—the assumption of an infinite stress singularity at the crack tip—by introducing a finite plastic (cohesive) zone where material separation occurs under a constant yield stress.

In this model, the crack does not terminate abruptly. Instead, it is considered to be physically extended by a cohesive zone of finite length, within which plastic deformation resists further crack opening. The material in this zone yields at a constant stress, denoted

by σ^Y, thereby eliminating the stress singularity and providing a more realistic description of ductile fracture.

Consider a centrally cracked, thin, elastic-perfectly plastic sheet subjected to an external tensile stress σ^P, as illustrated in **Fig. 2.4**. The physical crack has a half-length c, and a cohesive zone of length r_p develops, where the material yields under a constant stress σ^Y. For plane strain conditions, the yield stress is multiplied by a plastic constraint factor λ (i.e., $\lambda\sigma^Y$) to account for the effect of thickness constraint. The total length including the physical crack and the plastic zone is defined as the fictitious crack length a.

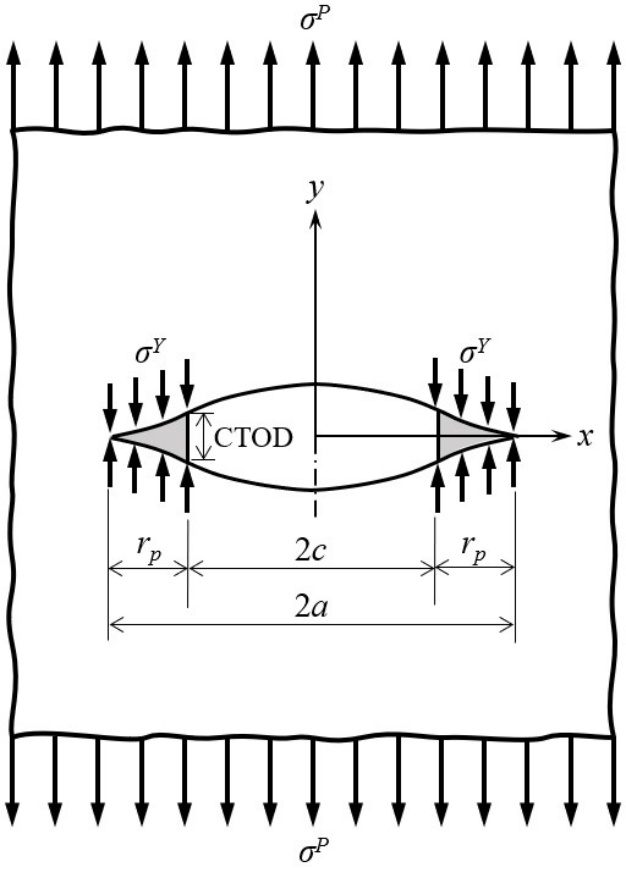

Fig. 2.4 Schematic of the Dugdale CZM for a centrally cracked, thin elastic-perfectly plastic sheet under tensile stress σ^P, with cohesive zones of length r_p exerting closing tractions equal to the material yield stress σ^Y

The Dugdale model is governed by two main conditions:

- Equilibrium: The applied external stress and the cohesive (closing) tractions within the plastic zone must be balanced to ensure force equilibrium.
- CTOD: The opening displacement at the physical crack tip must match the displacement produced by the yielded zone, ensuring continuous deformation.

Under these conditions, the total SIF at the fictitious crack tip is given by the superposition of:

- the SIF, K^P, due to external loading σ^P,
- the SIF, K^Y, due to closing tractions σ^Y within the plastic zone

To prevent stress singularity at the fictitious crack tip, the net SIF must be zero:

$$K^P + K^Y = 0 \tag{2.5}$$

This signifies that the crack is stabilized under the combined influence of external stress and internal cohesive resistance.

The Dugdale model provides a conceptual basis for many modern SYMs, and fracture process zone models used in EPFM . It plays a significant role in understanding and modeling crack tip plasticity and has been widely extended to 3D fracture problems.

In the present study, the Dugdale model offers an essential analogy for understanding the role of distributed internal tractions along the crack faces, particularly when developing simplified 2D substitute models for analyzing 3D elastic-plastic crack problems.

2.2 Equivalent Distributed Stress

This study introduces the concept of EDS for 3D cracks to represent the mechanical effect of complex 3D crack-tip plasticity through a simplified 2D models. The approach builds upon the original EDS theory proposed by Toyosada et al., enabling the evaluation of EPFM parameters in 3D cracked bodies while significantly reducing computational costs.

The EDS concept stems from the physical analogy to the Dugdale CZM, in which internal plastic resistance is modeled as closing tractions distributed along the extended crack faces within the cohesive region. In the present study, EDS is defined as a distributed normal traction acting along the crack surfaces of a 2D substitute body, reproducing the SIFs that would be obtained in the original 3D configuration.

Unlike actual cohesive tractions governed by plastic flow or material separation, the EDS is not a physically measurable quantity, but a mathematically equivalent representation derived from inverse analysis. By calibrating the EDS such that the resulting SIF in the 2D substitute body matches that of the original 3D crack under given loading, the model captures the essential features of crack-tip shielding due to plasticity.

This method leverages the weight function approach described earlier, allowing the EDS to be evaluated from known or estimated SIF values. Once obtained, the EDS serves as a unified internal loading that represents the effect of 3D plastic deformation and facilitates the evaluation of key EPFM parameters, such as plastic zone size and CTOD for 3D cracks.

In the current study, EDS analyses are conducted for 3D penny-shaped and surface cracks with various aspect ratios using two types of 2D substitute cracks: edge crack in a semi-infinite plate and center-through crack in an infinite plate. For the edge crack model, c and a denote the physical and fictitious crack lengths, respectively. In the center-through crack model, they represent the half-lengths of the physical and fictitious cracks. The corresponding model configurations and their weight functions are discussed in detail in **Section 2.3**.

When an external stress σ^P is applied to a 3D cracked body, CFTs t^P and t^Y are induced, representing the effects of σ^P and the cohesive stress σ^Y. Based on the Dugdale concept, the cohesive traction t^Y is assumed to act at a constant value $\lambda\sigma^Y$ over the cohesive region, where λ is the plastic constraint factor, and σ^Y is the yield stress of the material. The SIFs associated with t^P and t^Y, designated K^P and K^Y are used as prescribed input values in the EDS analysis to characterize the crack-opening behavior. These prescribed SIFs can also be obtained analytically or numerically, depending on the geometry of the 3D crack. To reproduce the prescribed SIFs in the 2D substitute model, EDS distributions are applied, denoted by f^P and f^Y corresponding to t^P and t^Y, respectively.

The SIF, denoted as K^P_{EDS}, resulting from the external stress EDS f^P, is determined using the weight function $g^*(x,a)$ corresponding to the 2D substitute crack, as follows:

$$K^P_{EDS} = \int_{x=0}^{a} f^P(x) g^*(x,a) dx \tag{2.6}$$

In the EDS framework, three numerical procedures are available to determine the cohesive stress EDS: yield stress loading method (YLM), whole crack face loading method (WLM), and fictitious crack face loading method (FLM).

The advantages and limitations of each method, along with the one adopted in this study and its rationale, are discussed in the following subsections.

2.2.1 Yield Stress Loading Method

The YLM offers a simplified approach to evaluate the cohesive stress SIF by applying a constant cohesive traction equal to the product of the plastic constraint factor λ and the material yield stress σ^Y, instead of determining the full EDS distribution. By assuming $t^Y = \lambda\sigma^Y$ over the cohesive zone region, this method eliminates the need to iteratively establish the relationship between cohesive stress and fictitious crack length, thereby significantly reducing computational complexity.

In this method, the approximate cohesive stress SIF, denoted as $\widetilde{K}^Y_{EDS}$, is calculated as follows:

$$\widetilde{K}^Y_{EDS} = \int_{x=c}^{a} t^Y(x) g^*(x,a) dx \tag{2.7}$$

However, this simplification comes with limitations. The assumption of a uniform cohesive traction in the 2D substitute model does not accurately reflect the stress redistribution near the crack tip, which may affect the precision of the resulting SIF, particularly for 3D cracks with pronounced plasticity gradients. Therefore, YLM is suitable only for approximate analyses or as an initial estimate in iterative procedures.

2.2.2 Whole Crack Face Loading Method

In WLM, the cohesive stress EDS, f_0^Y, for the case of $c = 0$ is first calculated, and the resulting SIF is then determined using superposition principle by subtracting the SIF generated by f_0^Y acting on the physical crack face ($0 \le x \le c$) from the SIF generated by the same EDS f_0^Y applied over the entire crack face up to the fictitious crack tip ($0 \le x \le a$) as illustrated in **Fig. 2.5**. (Note: For clarity, the closing stress f_0^Y is depicted with an opening direction in the figure.)

Mathematically, the approximate cohesive stress SIF $\widetilde{K}^Y_{EDS}$ can be expressed as:

$$\widetilde{K}^Y_{EDS} = \int_{x=0}^{a} f_0^Y(x) g^*(x,a) dx - \int_{x=0}^{c} f_0^Y(x) g^*(x,a) dx \tag{2.8}$$

This method is straightforward because it involves only the evaluation of SIF due to external stress distribution, and the cohesive stress SIF can be obtained simultaneously using a similar procedure. However, it may introduce numerical inefficiencies due to the subtraction of two large, similar quantities to obtain a relatively small cohesive stress SIF.

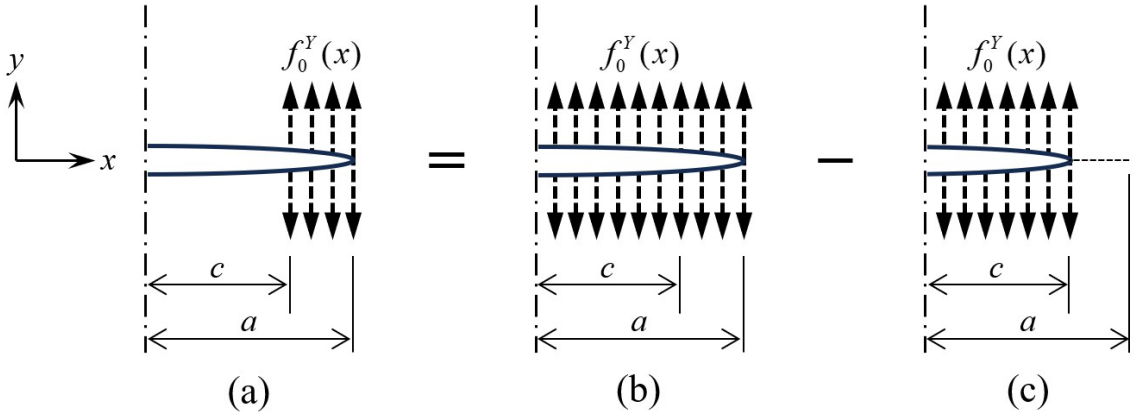

Fig. 2.5 Concept of WLM for calculating the cohesive stress SIF: **(a)** f_0^Y acting on the region ($c \le x \le a$); **(b)** f_0^Y acting on the whole crack face ($0 \le x \le a$); **(c)** f_0^Y acting on the physical crack face ($0 \le x \le c$)

2.2.3 Fictitious Crack Face Loading Method

Previous research by Toyosada et al. [64] demonstrated that EPFM parameters evaluated using YLM tend to overestimate the plastic zone size under high applied stress, while WLM tend to underestimate both the plastic zone size and CTOD under the examined conditions. In contrast, FLM shows good agreement with reference solutions. Based on these findings, FLM is adopted in the present study.

In FLM, the cohesive stress EDS f^Y is applied only over the fictitious crack extension region, i.e., from the physical crack tip to the fictitious crack tip ($c \le x \le a$). This focused application better captures the actual distribution of crack-tip plasticity effects and avoids the oversimplification of uniform loading across the cohesive region.

The cohesive stress SIF K_{EDS}^Y is evaluated as:

$$K_{EDS}^Y = \int_{x=c}^{a} f^Y(x) g^*(x,a) dx \tag{2.9}$$

Unlike YLM and WLM, FLM requires iterative updates of the cohesive stress SIF as the physical crack grows in order to determine the appropriate f^Y that reproduces the prescribed K^Y. While this increases computational effort, it results in more accurate predictions of both the plastic zone size and CTOD, making FLM particularly suitable for the evaluation of 3D cracks under significant plastic deformation.

Fig. 2.6 presents an illustrative example of the FLM-based EDS approach, where a 3D surface crack is used as the target model and a 2D edge crack serves as the substitute

model. The coordinate systems and dimensional definitions for both models are also depicted in the figure. The crack length–SIF relationships at the point of interest, resulting from the traction stresses t^P and t^Y acting on the 3D surface crack, are provided as prescribed input values to reproduce equivalent relationships in the 2D substitute edge crack. These relationships should be extended to a specific coordinate to ensure full coverage of the cohesive region under the intended applied stress conditions.

To match the SIFs of the 3D model, corresponding stress distributions must be applied to the 2D model. These fictitious stresses are referred to as EDSs, denoted f^P and f^Y, corresponding to t^P and t^Y, respectively. These EDSs are constructed using spline partitions, with the spline coefficients determined via generalized matrix inversion techniques. Once the EDSs are obtained, the elastic-plastic CODs and associated EPFM parameters of the target 3D crack can be evaluated by performing numerical integration or by employing analytical closed-form solutions to the 2D substitute crack model. The procedures for deriving EDSs that reproduce the crack length–SIF relationships are detailed in **Chapter 3**.

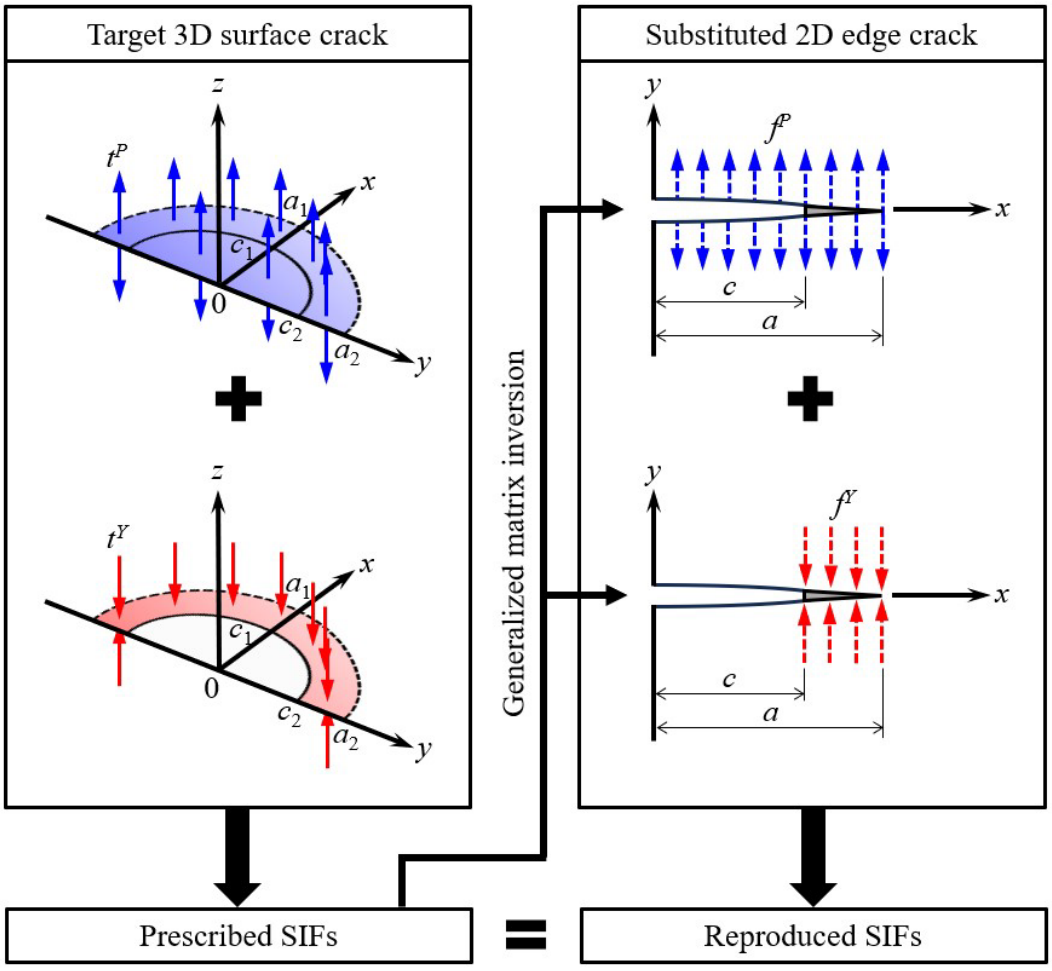

Fig. 2.6 Illustration of the FLM-based EDS concept for a 3D surface crack

2.3 Weight Functions of 2D Substitute Cracks

In the EDS method, the weight function approach is utilized to evaluate SIFs in 2D substitute crack models that replicate the fracture behavior of original 3D cracks. This section introduces the specific weight functions for two representative 2D crack configurations: a center-through crack in an infinite plate and an edge crack in a semi-infinite plate. The elastic-plastic crack opening behavior of 3D cracks is analyzed using these 2D models subjected to EDS distributions. The effectiveness and accuracy of each configuration in representing 3D crack behavior are discussed in the subsequent chapters.

2.3.1 Center-Through Crack in an Infinite Plate

The center-through crack in an infinite plate is a classical 2D configuration commonly used for analytical fracture mechanics studies due to its geometric simplicity and well-established solutions. This model consists of a crack of total length $2a$, symmetrically embedded in an infinite plate. The symmetry and unbounded geometry facilitate accurate evaluation of the SIFs and CODs through the use of its analytical weight function.

Let $g_C(x,a)$ represent the weight function of a center-through crack in an infinite plate, where a pair of unit concentrated forces is applied symmetrically at position $\pm x$ on the crack faces, as illustrated in **Fig. 2.7**. Here, a represents the half-length of the crack.

The analytical closed-form solution for $g_C(x,a)$ is given as follows [65]:

$$g_C(x,a) = \sqrt{\frac{a}{\pi}} \frac{2}{\sqrt{a^2 - x^2}} \tag{2.10}$$

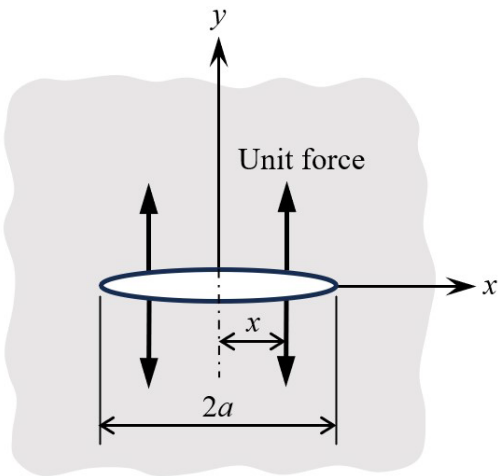

Fig. 2.7 Schematic of a center-through crack in an infinite plate with symmetrically applied unit-concentrated forces at coordinate $\pm x$ on the crack faces

2.3.2 Edge Crack in a Semi-Infinite Plate

An edge crack in a semi-infinite plate is another fundamental 2D configuration frequently used to simulate cracks emanating from a free surface. In this setup, a single crack of length, a, extends from the edge of a semi-infinite body.

Consider $g_E(x,a)$ as the weight function or SIF of an edge crack in a semi-infinite plate when a pair of unit-concentrated forces is applied at point x on the crack length a, as shown in **Fig. 2.8**. This function is given by the following approximation formula, which was derived by Sih [66].

$$g_E(x,a) = \frac{2}{\sqrt{\pi a\left[1-\left(\frac{x}{a}\right)^2\right]}}\left[1.297 - 0.297\left(\frac{x}{a}\right)^{1.25}\right] \tag{2.11}$$

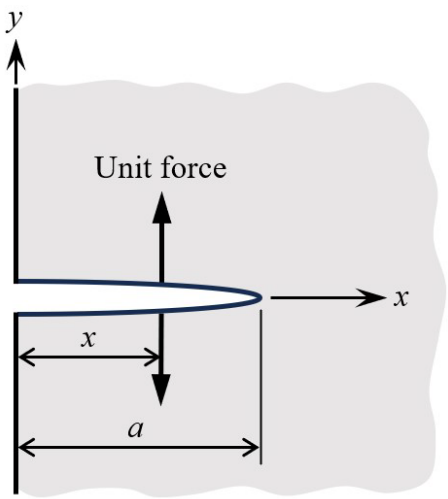

Fig. 2.8 Schematic of an edge crack in a semi-infinite plate with symmetrically applied unit-concentrated forces at coordinate x on the crack faces

CHAPTER 3

FLM-BASED EDS METHODOLOGY

3.1 EDS Determination Procedures

Building on the methodologies and the concept of EDS introduced in **Chapter 2**, this section details the procedures for determining EDS distributions that reproduce the SIFs of 3D cracks using 2D substitute models. The EDS determination process involves establishing the relationship between crack length and SIFs, employing spline interpolation to represent the stress distribution, and formulating a system of equations based on the continuum conditions of the EDS. This system is subsequently solved using generalized matrix inversion to obtain the spline coefficients that define the EDS profile. These procedures constitute the core of the FLM-based EDS fracture analysis system and are essential for accurately evaluating the elastic-plastic crack behavior of 3D geometries. The following subsections describe each step of the procedure in detail.

3.1.1 Spline Interpolation and a–K Relationship Matrix

To accurately reconstruct the SIF distribution of 3D cracks using 2D substitute models, the EDS profiles must be precisely defined. In the EDS approach, spline interpolation is employed to approximate the EDS distributions over a discretized crack face of substitute crack. This subsection describes the partitioning strategy, spline representation, and the formulation of the *a–K* relationship matrix used as a basis for determining the EDS profiles.

Consider N as the number of spline partitions, with partition points located at coordinates $x_0, x_1, \cdots, x_N$. The i-th partition spans the interval $[x_{i-1}, x_i]$, where $i = 1, 2, \cdots, N$. These partition points are arranged so that one of them aligns with the physical crack tip at $x = c$. The partition where the lower boundary of the x-coordinate interval as c is designated as the i_c-th partition.

Let $a_{\max}$ be the maximum length of the fictitious crack. The partitioning is set up to ensure $x_0 = 0$, and $x_N > a_{\max}$. The indices $i_{\min}$ and $i_{\max}$ represent the minimum and maximum partition numbers within the integral region specified by **Eqs. (2.6)** and **(2.9)**. Specifically, when evaluating K_{EDS}^{P}, $i_{\min}$ is assigned the value 1, whereas for K_{EDS}^{Y} calculation, $i_{\min}$ is set equal to i_c.

The EDS in the i-th partition, $f_i(x)$, is approximated using 3rd-order spline interpolation as outlined below.

$$f_i(x) = \alpha_i x^3 + \beta_i x^2 + \gamma_i x + \delta_i \left(x_{i-1} < x \le x_i \right); \;\; i = 1, \cdots, N_{\mathrm{INT}} \tag{3.1}$$

Here, $N_{\mathrm{INT}} = i_{\max} - i_{\min} + 1$, and α_i, β_i, γ_i, δ_i represent the coefficients for spline interpolation. **Fig. 3.1** shows the schematic diagram of EDS expressed by a whole section spline function.

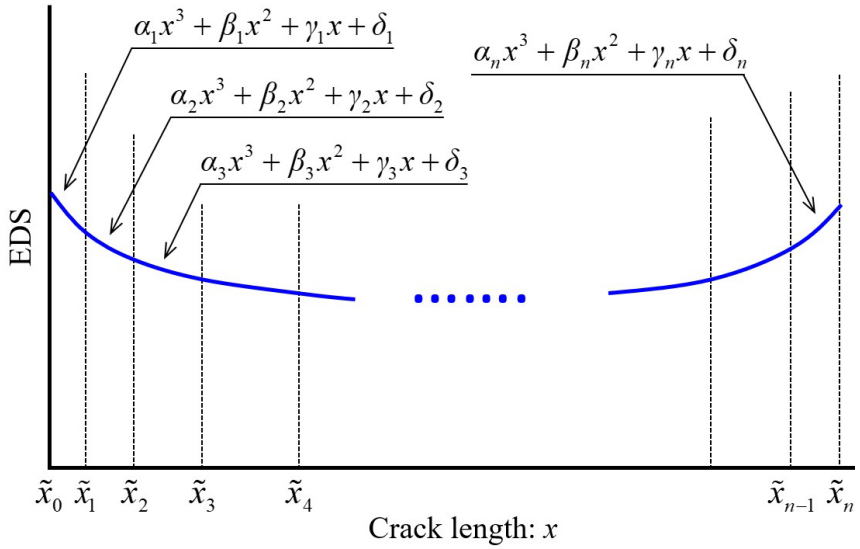

Fig. 3.1 Schematic diagram of the EDS expressed by a whole section spline function

The coefficient vector $\{X\}$ is expressed as:

$$\{X\} = \left\lfloor \alpha_{i_{\min}}, \beta_{i_{\min}}, \gamma_{i_{\min}}, \delta_{i_{\min}}, \cdots, \alpha_{i_{\max}}, \beta_{i_{\max}}, \gamma_{i_{\max}}, \delta_{i_{\max}} \right\rfloor^T \tag{3.2}$$

Consider N_a as the number of SIF calculation points, where the J-th point is represented as a_J ($J = 1, \cdots, N_a$). The value of N_a must be chosen to fulfill the condition $N_a \geq N$. The SIF at $x = a_J$ is denoted as K_J, and it can be evaluated using the following equation.

$$K_J = \sum\nolimits_{i=i_{\min}}^{x_i \le a_J} \left\{ A_{i(J\alpha)} \alpha_i + A_{i(J\beta)} \beta_i + A_{i(J\gamma)} \gamma_i + A_{i(J\delta)} \delta_i \right\}; \; J = 1, \cdots, N_a \tag{3.3}$$

$A_{i(J\alpha)}$, $A_{i(J\beta)}$, $A_{i(J\gamma)}$, and $A_{i(J\delta)}$ in **Eq. (3.3)** are provided as follows:

$$A_{i(J\alpha)} = G_{K,i}^{(3)}(a_J), \; A_{i(J\beta)} = G_{K,i}^{(2)}(a_J), \; A_{i(J\gamma)} = G_{K,i}^{(1)}(a_J), \; A_{i(J\delta)} = G_{K,i}^{(0)}(a_J) \tag{3.4}$$

and $G_{K,i}^{(\ell)}(a); (\ell = 0, 1, 2, 3)$ are computed as:

$$G_{K,i}^{(\ell)}(a) = \int_{\xi = x_{i-1}}^{\min(a, x_i)} \xi^{\ell} g^*(\xi, a) \, d\xi \tag{3.5}$$

Eq. (3.3) can be represented in the following matrix form:

$$\left[A\right]\left\{X\right\}=\left\{B\right\} \tag{3.6}$$

The matrix [A] in **Eq. (3.6)** is termed the *a–K* relationship matrix, and it is presented as follows:

$$\left[A\right]=\begin{bmatrix} A_{i_{\min}(1\alpha)} & A_{i_{\min}(1\beta)} & A_{i_{\min}(1\gamma)} & A_{i_{\min}(1\delta)} & \cdots & A_{i_{\max}(1\delta)} \\ A_{i_{\min}(2\alpha)} & A_{i_{\min}(2\beta)} & A_{i_{\min}(2\gamma)} & A_{i_{\min}(2\delta)} & \cdots & A_{i_{\max}(2\delta)} \\ \vdots & \vdots & \vdots & \vdots & \ddots & \vdots \\ A_{i_{\min}(n\alpha)} & A_{i_{\min}(n\beta)} & A_{i_{\min}(n\gamma)} & A_{i_{\min}(n\delta)} & \cdots & A_{i_{\max}(n\delta)} \end{bmatrix}, \tag{3.7}$$

$$\left\{B\right\}=\left\lfloor K_1,K_2,...,K_n\right\rfloor^T$$

$\{B\}$ is a column vector listing SIFs in the *a–K* relationship. The dimensions of the matrix [A], with respect to its rows (m) and columns (l), are given as:

$$m=N_a,\ l=4N_{\text{INT}}=4\left(i_{\max}-i_{\min}+1\right) \tag{3.8}$$

3.1.2 Continuum Condition of EDS and Elimination of Dependent Variables

The continuum condition of EDS at the node ($i = i_{\min}, \cdots, i_{\max\text{-}1}$), representing the connection point of the adjacent intervals, along with its 0th, 1st, and 2nd order derivatives, can be expressed by the following equations.

$$f_i\left(x_i\right)=f_{i+1}\left(x_i\right),\ f_i'\left(x_i\right)=f_{i+1}'\left(x_i\right),\ f_i''\left(x_i\right)=f_{i+1}''\left(x_i\right) \tag{3.9}$$

From **Eq. (3.9)**, the connection conditions at $x_{i_{\min}}$ are obtained as:

$$\begin{aligned} &\alpha_{i_{\min}}x_{i_{\min}}^3+\beta_{i_{\min}}x_{i_{\min}}^2+\gamma_{i_{\min}}x_{i_{\min}}+\delta_{i_{\min}}-\left(\alpha_{i_{\min}+1}x_{i_{\min}}^3+\beta_{i_{\min}+1}x_{i_{\min}}^2+\gamma_{i_{\min}+1}x_{i_{\min}}+\delta_{i_{\min}+1}\right)=0 \\ &3\alpha_{i_{\min}}x_{i_{\min}}^2+2\beta_{i_{\min}}x_{i_{\min}}+\gamma_{i_{\min}}-\left(3\alpha_{i_{\min}+1}x_{i_{\min}}^2+2\beta_{i_{\min}+1}x_{i_{\min}}+\gamma_{i_{\min}+1}\right)=0 \\ &6\alpha_{i_{\min}}x_{i_{\min}}+\beta_{i_{\min}}-\left(6\alpha_{i_{\min}+1}x_{i_{\min}}+\beta_{i_{\min}+1}\right)=0 \end{aligned} \tag{3.10}$$

Eq. (3.10) is solved for $\alpha_{i_{\min}}$, $\beta_{i_{\min}}$, and $\gamma_{i_{\min}}$ to obtain the following.

$$\begin{Bmatrix}\alpha_{i_{\min}}\\ \beta_{i_{\min}}\\ \gamma_{i_{\min}}\end{Bmatrix}=\left[C_1\right]\begin{Bmatrix}\delta_{i_{\min}}\\ \alpha_{i_{\min}+1}\\ \beta_{i_{\min}+1}\\ \gamma_{i_{\min}+1}\\ \delta_{i_{\min}+1}\end{Bmatrix};\ \left[C_1\right]=\begin{bmatrix} -\dfrac{1}{x_{i_{\min}}^3} & 1 & 0 & 0 & \dfrac{1}{x_{i_{\min}}^3} \\ \dfrac{3}{x_{i_{\min}}^2} & 0 & 1 & 0 & -\dfrac{3}{x_{i_{\min}}^2} \\ -\dfrac{3}{x_{i_{\min}}} & 0 & 0 & 1 & \dfrac{3}{x_{i_{\min}}} \end{bmatrix} \tag{3.11}$$

From **Eqs. (3.2)** and **(3.11)**,

$$\{X\}=\begin{Bmatrix}\alpha_{i_{\min}}\\ \beta_{i_{\min}}\\ \gamma_{i_{\min}}\\ \delta_{i_{\min}}\\ \alpha_{i_{\min}+1}\\ \beta_{i_{\min}+1}\\ \gamma_{i_{\min}+1}\\ \delta_{i_{\min}+1}\\ \vdots\\ \delta_{i_{\max}}\end{Bmatrix}=[T_1]\begin{Bmatrix}\delta_{i_{\min}}\\ \alpha_{i_{\min}+1}\\ \beta_{i_{\min}+1}\\ \gamma_{i_{\min}+1}\\ \delta_{i_{\min}+1}\\ \vdots\\ \delta_{i_{\max}}\end{Bmatrix};\ [T_1]=\begin{bmatrix}[C_1] & [O_{1U}]\\ [I_1]\end{bmatrix} \tag{3.12}$$

$[I_1]$ is an identity matrix of dimensions $\{4N_{\mathrm{INT}}-(4\cdot 1)+1\}\times\{4N_{\mathrm{INT}}-(4\cdot 1)+1\}$, and $[O_{1U}]$ is a zero matrix of size $3\times\{4N_{\mathrm{INT}}-(4\cdot 1)+1-5\}$.

Similar to **Eq. (3.12)**, the following equation is obtained as the connection condition for x_i ($i = i_{\min+1}, \cdots, i_{\max-1}$).

$$\begin{Bmatrix}\alpha_i\\ \beta_i\\ \gamma_i\end{Bmatrix}=[C_i]\begin{Bmatrix}\delta_i\\ \alpha_{i+1}\\ \beta_{i+1}\\ \gamma_{i+1}\\ \delta_{i+1}\end{Bmatrix};\ [C_i]=\begin{bmatrix}-\dfrac{1}{x_i^3} & 1 & 0 & 0 & \dfrac{1}{x_i^3}\\ \dfrac{3}{x_i^2} & 0 & 1 & 0 & -\dfrac{3}{x_i^2}\\ -\dfrac{3}{x_i} & 0 & 0 & 1 & \dfrac{3}{x_i}\end{bmatrix} \tag{3.13}$$

Using **Eq. (3.13)** for $i = i_{\min}+1$,

$$\begin{Bmatrix}\delta_{i_{\min}}\\ \alpha_{i_{\min}+1}\\ \beta_{i_{\min}+1}\\ \gamma_{i_{\min}+1}\\ \delta_{i_{\min}+1}\\ \vdots\\ \delta_{i_{\max}}\end{Bmatrix}=[T_2]\begin{Bmatrix}\delta_{i_{\min}}\\ \delta_{i_{\min}+1}\\ \alpha_{i_{\min}+2}\\ \beta_{i_{\min}+2}\\ \gamma_{i_{\min}+2}\\ \delta_{i_{\min}+2}\\ \vdots\\ \delta_{i_{\max}}\end{Bmatrix};\quad [T_2]=\begin{bmatrix}1 & 0 & 0\\ 0 & [C_2] & [O_2]\\ 0 & [I_{2,L}]\end{bmatrix} \tag{3.14}$$

$[I_{2,L}]$ is an identity matrix of dimensions $\{4N_{\mathrm{INT}} - (4 \cdot 2) + 1\} \times \{4N_{\mathrm{INT}} - (4 \cdot 2) + 1\}$, and $[O_2]$ is a zero matrix of size $3 \times \{4N_{\mathrm{INT}} - (4 \cdot 2) + 1 - 5\}$. $[C_2]$ corresponds to $[C_i]$ in **Eq. (3.13)** when $i = i_{\min+1}$.

Substituting **Eq. (3.14)** into **Eq. (3.12)**,

$$\{X\} = [T_1][T_2]\left\lfloor \delta_{i_{\min}}, \delta_{i_{\min}+1}, \alpha_{i_{\min}+2}, \beta_{i_{\min}+2}, \gamma_{i_{\min}+2}, \delta_{i_{\min}+2}, \cdots, \delta_{i_{\max}} \right\rfloor^T \tag{3.15}$$

Repeating the above procedure for $i = i_{\min+2}, \cdots, i_{\max-1}$ yields the following equation.

$$\{X\} = [\Pi_T]\{X'\};\ [\Pi_T] = [T_1]\cdots\left[T_{N_{\mathrm{INT}}-1}\right] \tag{3.16}$$

$[T_1]_{i\geq 2}$ of **Eq. (3.16)** is given as:

$$[T_i]_{i\geq 2} = \begin{bmatrix} \left[I_{i,U}\right] & 0 & 0 \\ 0 & [C_i] & [O_i] \\ 0 & \left[I_{i,L}\right] & \end{bmatrix} \tag{3.17}$$

$[I_{i,U}]$ is an identity matrix of size $\{i - 1\} \times \{i - 1\}$. $[I_{i,L}]$ is an identity matrix with dimensions of $\{4N_{\mathrm{INT}} - (4i) + 1\} \times \{4N_{\mathrm{INT}} - (4i) + 1\}$, and $[O_i]$ is a zero matrix of size $3 \times \{4N_{\mathrm{INT}} - (4i) + 1 - 5\}$.

$\{X'\}$ in **Eq. (3.16)** is the independent spline coefficient matrix defined by:

$$\{X'\} = \left\lfloor \delta_{i_{\min}}, \delta_{i_{\min}+1}, \cdots \delta_{i_{\max}-1}, \alpha_{i_{\max}}, \beta_{i_{\max}}, \gamma_{i_{\max}}, \delta_{i_{\max}} \right\rfloor^T \tag{3.18}$$

The number of independent coefficients, $\bar{n}$, is calculated by the following equation.

$$\bar{n} = N_{\mathrm{INT}} + 3 = i_{\max} - i_{\min} + 4 \tag{3.19}$$

$[\Pi_T]$ in **Eq. (3.16)** is a transformation matrix that computes all coefficients from the independent coefficients.

Substituting **Eq. (3.16)** into **Eq. (3.6)** yields:

$$[A]\{X\} = [M]\{X'\} = \{B\};\ [M] = [A][\Pi_T] \tag{3.20}$$

The matrix $[M]$ has m rows, as defined in **Eq. (3.8)**, and the number of columns $\bar{n}$ corresponds to the expression in **Eq. (3.19)**. When $N_{\mathrm{INT}} = 1$, $\{X'\} = \{X\}$, and the transformation matrix $[\Pi_T]$ in **Eq. (3.16)** becomes the identity matrix.

3.1.3 Determination of Spline Coefficients by Generalized Matrix Inversion

Spline partition points are placed at intervals coarser than the SIF calculation points, with exclusive consideration given to the case where $m > \bar{n}$. $\{X'\}$ from **Eq. (3.18)** can be obtained by utilizing the least-squares generalized inverse of the matrix $[M]$ [67]. In case the solution shows oscillations due to the instability of the generalized inverse matrix, the rank reduction method using singular value decomposition [68] can be implemented to alleviate such behavior. For the scenario where $m > \bar{n}$, the rank of matrix $[M]$ can be determined using the following equation.

$$R = \text{Rank}\left[M\right] = \min\left(m, \bar{n}\right) = \bar{n} \tag{3.21}$$

Let $\lambda^{(q)}$ and $\{v^{(q)}\}$ (q = 1, ···, Rank $[M]$ = $\bar{n}$) represent the eigenvalues and eigenvectors of $[M]^T[M]$. For q = 1, ···, $\bar{n}$, the vector $\{w^{(q)}\}$ can be defined as follows:

$$\left\{w^{(q)}\right\} = \frac{1}{\kappa^{(q)}}\left[M\right]\left\{v^{(q)}\right\};\ \kappa^{(q)} = \sqrt{\lambda^{(q)}} \tag{3.22}$$

Here, $\kappa^{(q)}$ denotes the singular value of matrix $[M]$. The Moore-Penrose generalized inverse matrix $[M^+]$ which is an $\bar{n} \times m$ matrix, with Rank $[M^+] = \bar{n}$ can be computed using the subsequent equation.

$$\left[M^+\right] = \sum_{q=1}^{\text{Rank}[E]=\bar{n}} \frac{1}{\kappa^{(q)}}\left\{v^{(q)}\right\}\left\lfloor w^{(q)} \right\rfloor \tag{3.23}$$

When $\kappa^{(q)}$ takes on exceptionally small values, the sensitivity of $[M^+]$ to numerical errors increases, leading to an ill-posed inverse problem. To address this issue, a lower threshold for $\kappa^{(q)}$ can be imposed, and singular values below this threshold can be excluded from the summation in **Eq. (3.23)**, consequently reducing the rank of $[M^+]$. In such cases, the generalized inverse matrix can be evaluated using the following equation.

$$\left[M^+\right] = \sum_{q=1}^{\kappa^{(q)} \geq \hat{\kappa},\ q \leq \bar{n}} \frac{1}{\kappa^{(q)}}\left\{v^{(q)}\right\}\left\lfloor w^{(q)} \right\rfloor \tag{3.24}$$

By employing the matrix $[M^+]$ from **Eq. (3.24)**, $\{X'\}$ can be achieved as:

$$\left\{X'\right\} = \left[M^+\right]\left\{B\right\} \tag{3.25}$$

Substituting **Eq. (3.25)** into **Eq. (3.16)**, the spline coefficients for all partitions can be determined as follows:

$$\left\{X\right\} = \left[\Pi_T\right]\left\{X'\right\} = \left[\Pi_T\right]\left[M^+\right]\left\{B\right\} \tag{3.26}$$

3.2 EDS-Based Cohesive Zone Model

Following the establishment of EDS distributions through spline-based interpolation and generalized matrix inversion in **Section 3.1**, this section introduces the application of these distributions to 2D substitute models within a CZM framework. The EDS-based CZM enables the evaluation of fracture behavior by explicitly incorporating both externally applied and cohesive stresses into the SIF calculation and crack opening analysis.

The EDS due to external loading, denoted as $f^P(x)$, is represented using a piecewise cubic spline function over $i_{\max}$ segments, with nodal coordinates $x_0 = 0, \cdots, x_{i_{\max}}$. In the FLM approach, the EDS due to cohesive stress, $f^Y(x)$, is similarly approximated using a spline defined over $i_{\max}$-i_c+1 segments, spanning from $x_{i_c} = c$ to $x_{i_{\max}}$. Each spline segment of $f_i^P(x)$ and $f_i^Y(x)$ is characterized by four spline coefficients: $\{\alpha_i^P, \beta_i^P, \gamma_i^P, \delta_i^P\}$ and $\{\alpha_i^Y, \beta_i^Y, \gamma_i^Y, \delta_i^Y\}$, respectively.

3.2.1 Calculation of SIF and Plastic Zone Size

When $f_i^P(x)$ acts over the region ($0 \le x \le a$) of the substituted 2D crack, the SIF at the fictitious crack tip, K_{EDS}^P, can be determined using the following equation.

$$\begin{aligned} K_{EDS}^P &= \sum_{i=1}^{0\le x_i\le a} \int_{\xi=x_{i-1}}^{\min(a,x_i)} f_i^P(\xi) g^*(\xi, a)\, d\xi \\ &= \sum_{i=1}^{x_i\le a} \left\{ G_{K,i}^{(3)}(a)\alpha_i^P + G_{K,i}^{(2)}(a)\beta_i^P + G_{K,i}^{(1)}(a)\gamma_i^P + G_{K,i}^{(0)}(a)\delta_i^P \right\} \end{aligned} \tag{3.27}$$

Likewise, the SIF at the fictitious crack tip for cohesive stress EDS, denoted as K_{EDS}^Y, is obtained when $f_i^Y(x)$ acts over the region ($c \le x \le a$) of the substitute body, as follows.

$$\begin{aligned} K_{EDS}^Y &= \sum_{i=i_c}^{x_i\le a} \int_{\xi=\max(c,x_{i-1})}^{\min(a,x_i)} f_i^Y(\xi) g^*(\xi, a)\, d\xi \\ &= \sum_{i=i_c}^{x_i\le a} \left\{ G_{K,i}^{(3)}(a)\alpha_i^Y + G_{K,i}^{(2)}(a)\beta_i^Y + G_{K,i}^{(1)}(a)\gamma_i^Y + G_{K,i}^{(0)}(a)\delta_i^Y \right\} \end{aligned} \tag{3.28}$$

Here ξ is the coordinate of the crack length a in the x-direction.

Since the stress singularity disappears at the fictitious crack tip, the following equation can be derived.

$$K_{EDS}^P - K_{EDS}^Y = 0 \tag{3.29}$$

The length of the fictitious crack, a, is determined through iterative calculations satisfying **Eq. (3.29)**. The plastic zone size r_p can be computed as:

$$r_p = a - c \tag{3.30}$$

3.2.2 Calculation of Crack Opening Displacement

The calculation of CODs for the target 3D crack is carried out using the EDS applied to the 2D substitute crack models. COD at the coordinate x, resulting from a pair of unit-concentrated EDS applied to the coordinate ξ of the crack length a, can be determined using Paris's reciprocal theorem, as presented below [69].

$$V_0(x;\xi,a) = \frac{2}{E'}\int_{\bar{a}=\max(\xi,x)}^{a} g^*(\xi,\bar{a})\, g^*(x,\bar{a})\, d\bar{a} \tag{3.31}$$

E' is defined in terms of Young's modulus E, and Poisson's ratio ν, considering either the plane stress or plane strain condition.

$$E' = \begin{cases} E & (\text{plane stress}) \\ \dfrac{E}{1-\nu^2} & (\text{plane strain}) \end{cases} \tag{3.32}$$

According to **Eq. (3.31)**, CODs induced by $f_i^P(x)$ and $f_i^Y(x)$, referred to as $V^P(x)$ and $V^Y(x)$ respectively, can be calculated using the following equations.

$$\begin{aligned} V^P(x) &= \frac{2}{E'}\sum_{i=1}^{i_{\max}}\int_{\xi=x_{i-1}}^{\min(a,x_i)} f_i^P(\xi)\, V_0(x;\xi,a)\, d\xi \\ &= \frac{2}{E'}\sum_{i=1}^{i_{\max}}\left[\alpha_i^P G_{V,i}^{(3)}(x,a) + \beta_i^P G_{V,i}^{(2)}(x,a) + \gamma_i^P G_{V,i}^{(1)}(x,a) + \delta_i^P G_{V,i}^{(0)}(x,a)\right] \end{aligned} \tag{3.33}$$

$$\begin{aligned} V^Y(x) &= \frac{2}{E'}\sum_{i=i_c}^{i_{\max}}\int_{\xi=x_{i-1}}^{\min(a,x_i)} f_i^Y(\xi)\, V_0(x;\xi,a)\, d\xi \\ &= \frac{2}{E'}\sum_{i=i_c}^{i_{\max}}\left[\alpha_i^Y G_{V,i}^{(3)}(x,a) + \beta_i^Y G_{V,i}^{(2)}(x,a) + \gamma_i^Y G_{V,i}^{(1)}(x,a) + \delta_i^Y G_{V,i}^{(0)}(x,a)\right] \end{aligned} \tag{3.34}$$

$G_{V,i}^{(p)}(x,a)$; (p = 3, 2, 1, 0) is expressed as:

$$G_{V,i}^{(p)}(x,a) = \int_{\xi=x_{i-1}}^{\min(a,x_i)} \xi^p V_0(x;\xi,a)\, d\xi \tag{3.35}$$

The elastic-plastic COD of the target 3D crack, calculated from the EDS-applied 2D substitute crack is obtained as follows:

$$V(x) = V^P(x) - V^Y(x) \tag{3.36}$$

When using the center-through crack as the substitute model, the integrals in **Eqs. (3.5)**, **(3.31)**, and **(3.35)** can be evaluated analytically, reducing computation time in FCP analysis over many loading cycles. For the edge crack model, these integrals are computed numerically using the 10–21 point Gauss-Kronrod adaptive quadrature [70] from QUADPACK [71].

The characteristics of the COD curves resulting from the EDS-applied center-through and edge cracks are illustrated in **Figs. 3.2** and **3.3**, respectively. Here, the subscripts C and E represent the center-through and edge crack models. The slope of the COD curve resulting from the center-through crack is zero at $x = 0$ due to the symmetric boundary conditions. In contrast, the COD curve resulting from the edge crack exhibits a non-zero slope at $x = 0$, reflecting the absence of constraint at the crack mouth.

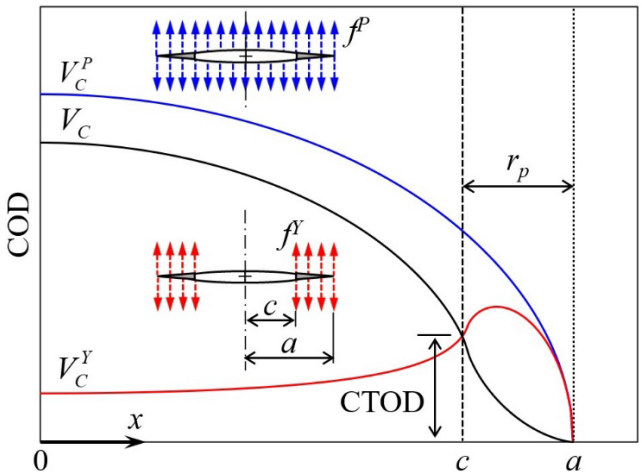

Fig. 3.2 Characteristic of the COD curves resulting from the EDS-applied 2D substitute center-through crack in an infinite plate

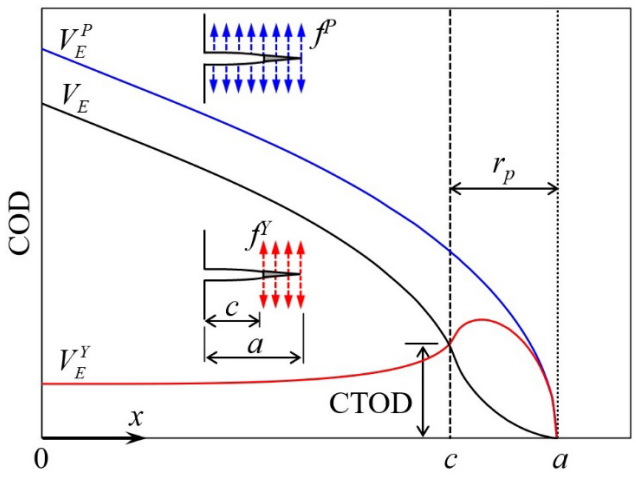

Fig. 3.3 Characteristic of the COD curves resulting from the EDS-applied 2D substitute edge crack in a semi-infinite plate

Using this EDS-based CZM framework, it is also possible to account for the effects of residual stress on crack tip opening behavior, discussed in **Appendix A**, by employing the same procedures as those used for external stress.

3.3 EDS Fracture Mechanics Analysis System

Based on the formulations described in the previous sections, the EDS-based fracture mechanics analysis of 3D cracks proceeds through the following steps:

a) Define the physical crack length c for the 3D target crack. The a–K relationships due to external and cohesive stresses are obtained using analytical or numerical methods appropriate for the crack geometry.

b) Set the number of spline intervals N and the nodal coordinates x_i such that the lower bound of the i_c-th interval coincides with c. Specify a lower threshold $\hat{\kappa}$ for singular values to be used in computing the generalized inverse matrix $[M^+]$.

c) Store the a–K relationships for external stress in column vector $\{B\}$ of **Eq. (3.6)**. Using the weight function g^* of the substitute crack, calculate the a–K relationship matrix $[A]$ and transformation matrix $[\Pi_T]$ from **Eqs. (3.6)** and **(3.16)**, respectively, with $i_{\min} = 1$. Then compute generalized inverse matrix $[M^+]$ using **Eq. (3.24)** and determine the spline coefficient matrix $\{X\}^{(P)}$ via **Eq. (3.26)**.

d) Similarly, store the cohesive stress a–K relationships in $\{B\}$ and evaluate $[A]$ and $[\Pi_T]$ with $i_{\min} = c$. Use **Eq. (3.24)** to compute $[M^+]$ and obtain $\{X\}^{(Y)}$ from **Eq. (3.26)**.

e) Set the initial fictitious crack length a_0 and the upper limit a_{UP} for the iterative search.

f) Assume $a = a_0$ and approximate the EDSs for external and cohesive stresses, $f_i^P(x)$ and $f_i^Y(x)$, using $\{X\}^{(P)}$ and $\{X\}^{(Y)}$, respectively. Calculate the corresponding SIFs, K_{EDS}^P and K_{EDS}^Y using **Eqs. (3.27)** and **(3.28)**, and check whether **Eq. (3.29)** is satisfied.

g) If **Eq. (3.29)** is not satisfied, apply the bisection method with c and a_{UP} as lower and upper bounds, respectively, to find the value of a that satisfies **Eq. (3.29)**. The plastic zone size r_p is then determined as $a - c$.

h) Using $\{X\}^{(P)}$, $\{X\}^{(Y)}$, and the fictitious crack length a, compute CODs $V^P(x)$ and $V^Y(x)$ induced by $f_i^P(x)$ and $f_i^Y(x)$, respectively via **Eqs. (3.33)** and **(3.34)**, employing the weight function g^* of the substitute crack. Finally, obtain the elastic-plastic COD $V(x)$ using **Eq. (3.36)**.

A comprehensive flowchart summarizing this FLM-based EDS analysis for evaluating EPFM parameters of the 3D cracked body is shown in **Fig. 3.4**.

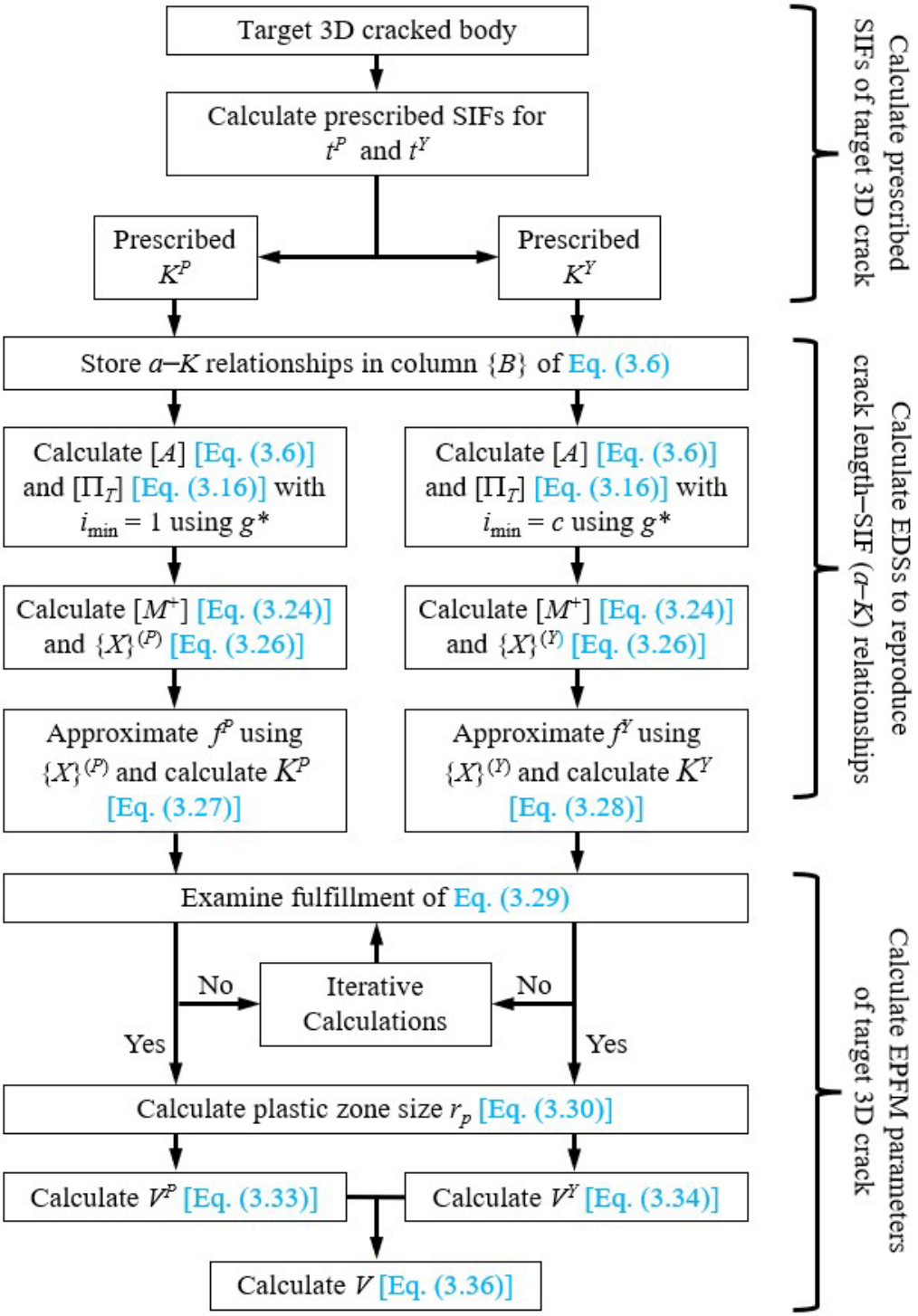

Fig. 3.4 Flowchart of FLM-based EDS fracture mechanics analysis system for 3D cracks

CHAPTER 4

VERIFICATION OF EDS ANALYSIS SYSTEM FOR 3D CRACKS

4.1 Framework for Validation

To verify the accuracy and applicability of the developed EDS analysis system for general 3D cracks, a benchmark problem with established reference solutions is required. For this purpose, a 3D penny-shaped crack embedded in an infinite plate under axisymmetric loading is adopted as the verification case [72,73]. This configuration is particularly well-suited for validation, as it possesses a straightforward analytical weight function that enables the precise generation of reference SIF data. Additionally, reference COD profiles can be obtained directly from existing analytical solutions. The axisymmetric geometry further ensures that the details of the EDS procedures can be presented clearly, free from the complexities introduced by asymmetric boundary conditions.

This chapter begins by determining the plastic constraint factor specific to the reference penny-shaped crack to enable accurate elastic-plastic fracture simulation under plane strain conditions. The prescribed a–K relationships for both external and cohesive stresses are then derived using the analytical weight function. Next, EDS distributions derived using the FLM-based formulation are then used to reproduce a–K relationships, which are then compared with the prescribed values. Finally, elastic-plastic COD profiles obtained from the EDS-based CZM framework are compared with those from analytical solutions, thereby demonstrating the physical fidelity of the proposed method. The EDS system was originally developed using a 2D center-through crack model due to its straightforward and computationally efficient weight function, and this model is employed as the primary substitute for the EPFM analysis of the 3D penny-shaped crack.

4.2 3D Penny-Shaped Crack under Axisymmetric Loading

A Dugdale-type 3D penny-shaped crack in an infinite plate subjected to axisymmetric loading is illustrated in **Fig. 4.1**. The crack, with radius c, lies in the x-y plane and is centered at the origin O. The loading is applied in the z-direction, normal to the crack surface, and is distributed in a radially symmetric manner, reducing the problem to a one-dimensional formulation in the radial coordinate x. Geometry assumes an infinite plate to eliminate boundary effects, ensuring the generality of the results.

In this model, the external loading is represented by a uniform tensile stress σ^P applied remotely. As stress increases, a Dugdale-type plastic zone r_p develops around the crack front, extending radially from $x = c$ to a fictitious crack tip at $x = a$. Within this plastic zone, a constant cohesive stress $\lambda\sigma^Y$, is assumed to oppose crack opening. This cohesive stress is introduced in the same spirit as in Dugdale CZM to capture elastic-plastic behavior.

The material is modeled as elastic–perfectly plastic, with no strain hardening. The mechanical properties are assigned as follows:

- Physical crack radius: c = 1.0 mm
- Young's Modulus: E = 206,000 MPa
- Yield stress: σ^Y = 392 MPa
- Poisson's ratio: v = 0.3

The axisymmetry of the problem permits straightforward derivation of the SIFs for both external and cohesive loading through the use of an analytical weight function, which plays a central role in both the reference solution and EDS formulation.

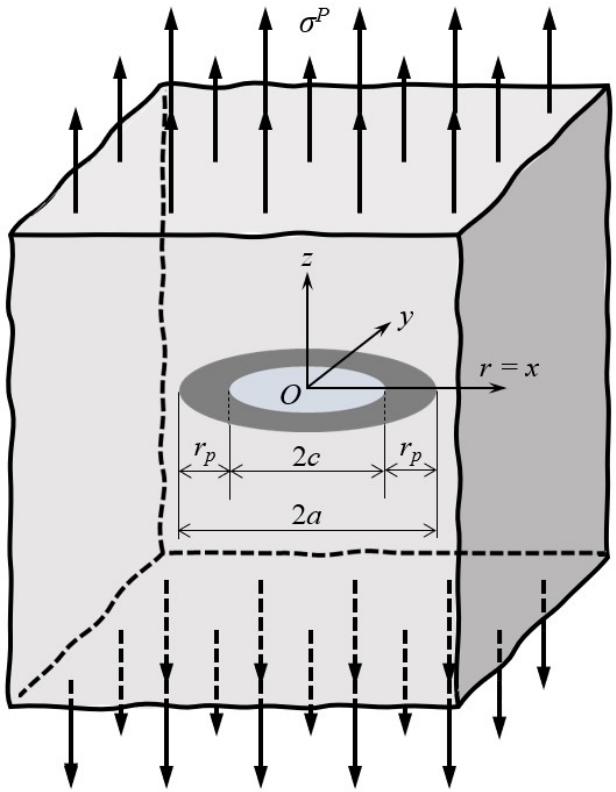

Fig. 4.1 Schematic of a 3D Dugdale-type penny-shaped crack of radius c embedded in an infinite solid, subjected to axisymmetric remote tensile loading σ^P, with a surrounding plastic zone extending to radius a

4.2.1 Determination of Plastic Constraint Factor

To accurately simulate elastic-plastic crack behavior using the EDS analysis system, it is essential to determine the plastic constraint factor λ for the target crack configuration. This factor accounts for the constraint effect near the crack tip and scales the yield stress σ^Y to reflect the level of triaxiality in the plastic zone. In general, λ ranges from 1.0 to 3.0, where $\lambda = 1.0$ corresponds to a fully plane stress condition, and $\lambda = 3.0$ represents an ideal plane strain condition [49]. However, in practical 3D configurations, even under conditions approximating plane strain, the actual constraint effect is often lower than the idealized value of 3 because the stress state is not as severe as it would be in a fully 3D deformation [74].

For the case of a 3D penny-shaped crack embedded in an infinite, isotropic, and homogeneous solid, λ can be estimated analytically. When the axial stress σ_z in the cohesive region corresponds to $\lambda\sigma^Y$, the plastic zone size r_p can be computed from the following equation derived for axisymmetric loading conditions [75].

$$r_p = c\left[\left\{1-\left(\frac{\sigma^P}{\lambda\sigma^Y}\right)^2\right\}^{-\frac{1}{2}}-1\right] \tag{4.1}$$

An alternative estimation of λ is provided by Keer's analysis, which is based on the maximum shear stress criterion. According to Keer's model, it is necessary to satisfy the following equation in the plastic region [76].

$$\sigma_z - \sigma_\theta = \sigma^Y \tag{4.2}$$

In this expression, σ_θ is the circumferential stress acting ahead of the crack front in the radial direction. Under this formulation, the plastic zone size $r_p = a - c$ can be explicitly expressed as:

$$\frac{(1-2\nu)\left(\frac{\sigma^P}{\sigma^Y}\right)}{2-(1+2\nu)\left(\frac{\sigma^P}{\sigma^Y}\right)} = \sqrt{1-\left(\frac{c}{a}\right)^2}-\frac{c}{2a}\cos^{-1}\frac{c}{a} \tag{4.3}$$

From **Eqs. (4.1)** and **(4.3)**, λ can be determined for various values of the normalized external load σ^P/σ^Y [77]. **Fig. 4.2** illustrates the relationship between λ and σ^P/σ^Y, as obtained

from the maximum shear stress model. The curve indicates that λ decreases with increasing applied stress, suggesting a gradual loss of constraint. This behavior highlights the transitional nature of constraint in 3D geometries, where the stress state evolves continuously.

The obtained λ values for the reference penny-shaped crack are subsequently used to calibrate the EDS-based CZM, ensuring that the simulated crack-tip fields faithfully represent elastic-plastic fracture under given conditions.

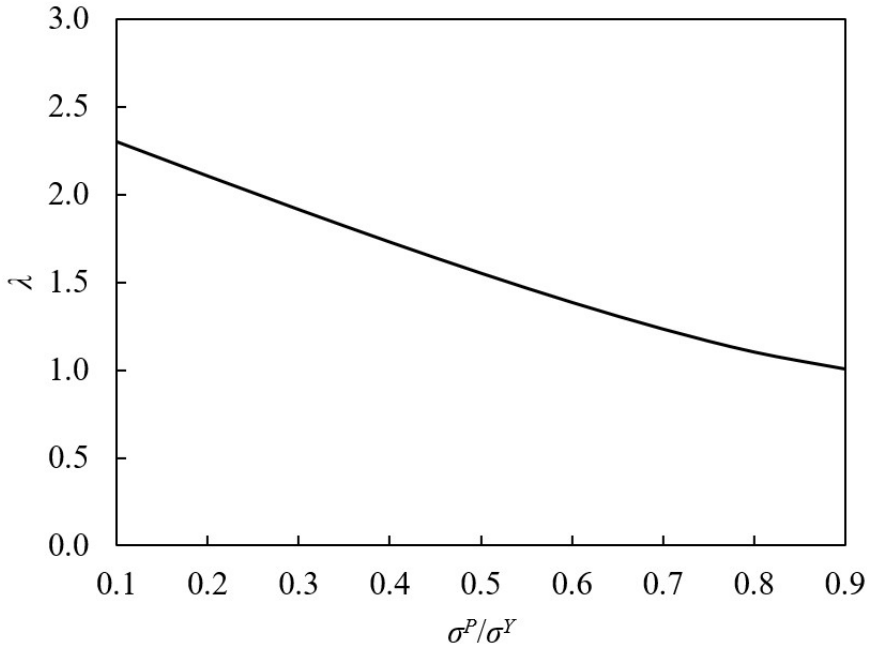

Fig. 4.2 Relationship between λ and σ^P/σ^Y for a 3D penny-shaped crack

4.2.2 Calculation of Prescribed a–K Relationships by Weight Function Method

The prescribed *a–K* relationships for both external and cohesive stresses are computed using the analytical weight function for a penny-shaped crack embedded in an infinite elastic medium.

The weight function, denoted as $g_P(x,a)$, represents the SIF response to a unit concentrated ring load applied at a radial position $r = x$ on the crack face of radius a, as illustrated in **Fig. 4.3**.

$$g_P(x,a) = \frac{2}{\sqrt{\pi a}} \frac{x}{\sqrt{a^2 - x^2}} \tag{4.4}$$

For external loading, normal stress is assumed to be a uniform traction t^P acting over the crack face. The corresponding reference SIF, denoted K^P_{Ref}, is derived by integrating the weight function with respect to the applied stress profile over the fictitious crack length a. The value of a is systematically varied beyond the physical crack radius c to simulate the extension of the plastic zone.

For the cohesive stress case, a constant traction $\lambda\sigma^Y$ is assumed to act uniformly over the plastic zone $c \le x \le a$, representing the Dugdale-type cohesive zone. The resulting reference SIF, K^Y_{Ref}, is calculated using the same weight function, but with the integration domain limited to the plastic zone from c to a. Both sets of prescribed a–K relationships serve as reference data for determining the EDSs to be applied on the 2D substitute center-through crack, such that the resulting SIF values match those of the original problem.

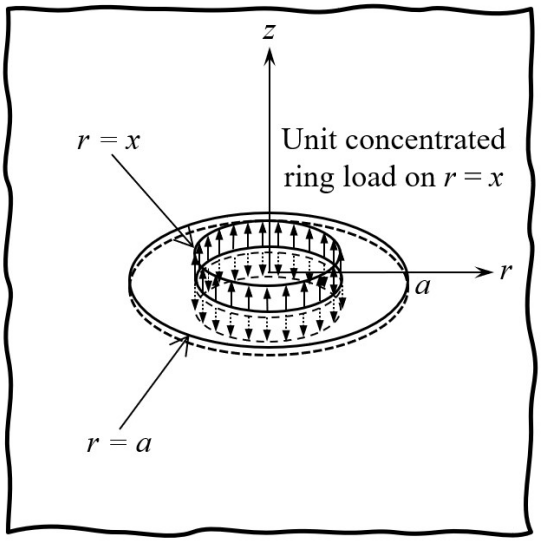

Fig. 4.3 Schematic of a penny-shaped crack embedded in an infinite plate, with unit concentrated ring load applied at a radial position $r = x$ on the crack face of radius a

As an illustrative example, consider a case in which a remote tensile stress of σ^P = 200 MPa is applied to a 3D penny-shaped crack with a physical radius of c = 1.0 mm. According to **Eqs. (4.1)** and **(4.3)**, this loading results in a plastic zone that extends radially to a fictitious crack size of a = 1.06 mm.

Fig. 4.4 presents a comparison between the weight functions g_C and g_P. Both functions increase monotonically with x, diverging to infinity as $x \to a$. The ratio g_C/g_P is plotted in **Fig. 4.5**, where it is evident that $g_C > g_P$ over the interval $0 \le x \le a$. This ratio diverges as $x \to 0$, decreases monotonically with increasing x, and approaches unity as $x \to a$.

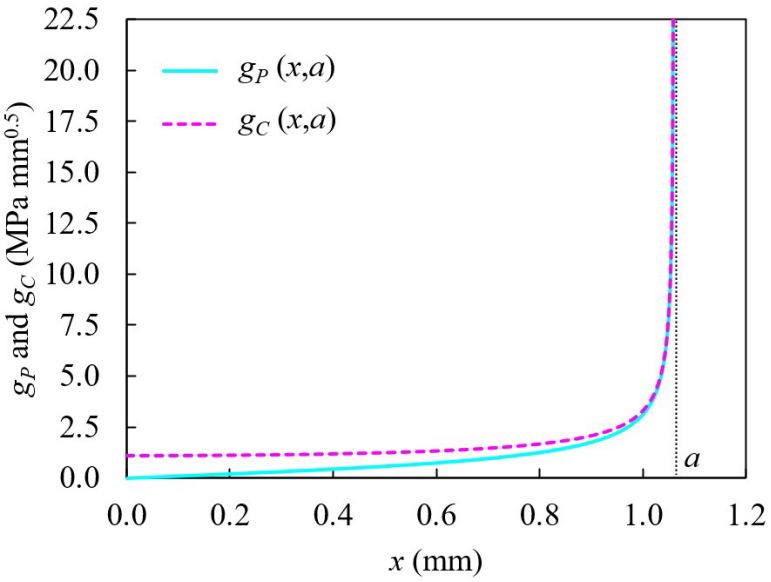

Fig. 4.4 Comparison of weight functions g_C and g_P as a function of x

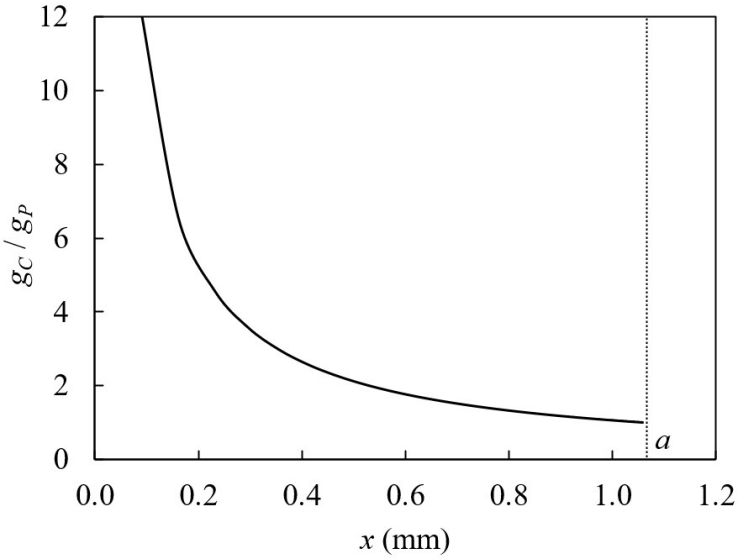

Fig. 4.5 Relationship between the ratio g_C/g_P and x

4.3 EDSs and Reproduced *a*–*K* Relationships

In this section, EDSs are computed to reproduce the prescribed *a*–*K* relationships established for the 3D penny-shaped crack. The objective is to assess how accurately the EDS-based formulation, originally developed using a 2D substitute model, can capture the elastic-plastic fracture behavior of the target 3D geometry. By applying the EDS analysis framework, the reconstructed SIFs are directly compared to the reference values derived analytically in **Section 4.2.2**. The consistency between these two sets of results provides a measure of the applicability and fidelity of the proposed method.

In the EDS analysis, the domain ranging from $x = 0$ to 1.2 mm is discretized into spline partitions with a uniform interval of 0.2 mm. Consequently, the interval index i_c corresponding to the location of the physical crack tip (i.e., $c = 1.0$ mm) is identified as 5.

Fig. 4.6 shows the comparison between the CFTs, t^P and t^Y, and the corresponding EDSs, f^P and f^Y, computed by the EDS-based analysis under a remote tensile stress of $\sigma^P = 200$ MPa. Since the analysis is performed on a 3D penny-shaped crack, while the EDS procedure employs the 2D center-through crack weight function g_C, a geometric mismatch arises. As a result, the EDSs cannot coincide with the CFTs due to the non-conformity of the applied weight function.

As discussed in **Section 4.2.2**, the 2D center-through crack weight function g_C is consistently larger than the 3D penny-shaped crack weight function g_P across the interval $0 \leq x \leq a$. Therefore, in order to ensure that the SIFs calculated from EDSs match the prescribed a–K relationships of the 3D model, the EDS magnitudes must be proportionally lower than the corresponding CFT, resulting in $f^P(x) < t^P(x)$.

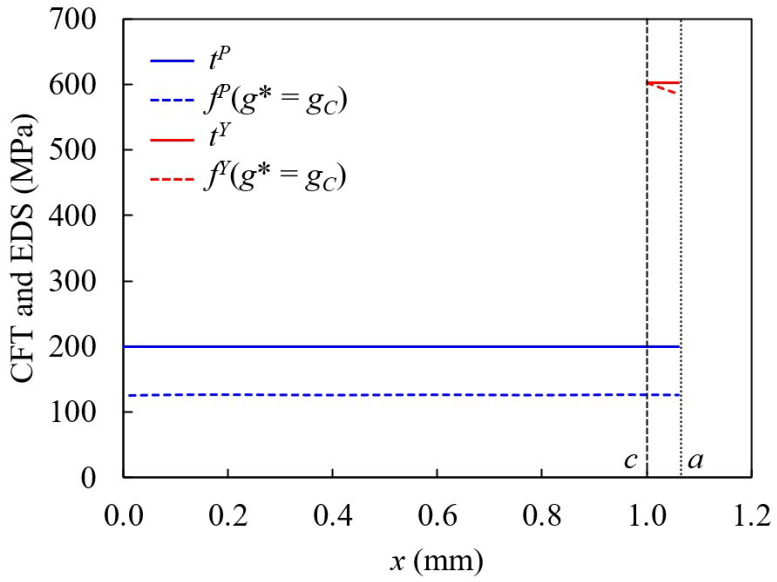

Fig. 4.6 Comparison of applied CFTs and calculated EDSs for a 3D penny-shaped crack in an infinite plate under uniform tensile loading ($c = 1.0$ mm, $\sigma^P = 200$ MPa)

Fig. 4.7 compares the products CFTs × g_P and EDSs × g_C. As outlined in **Section 2.1.2**, the area under each curve represents the corresponding SIF value. This comparison highlights how appropriately scaled EDSs can compensate for the use of a non-fitting weight function.

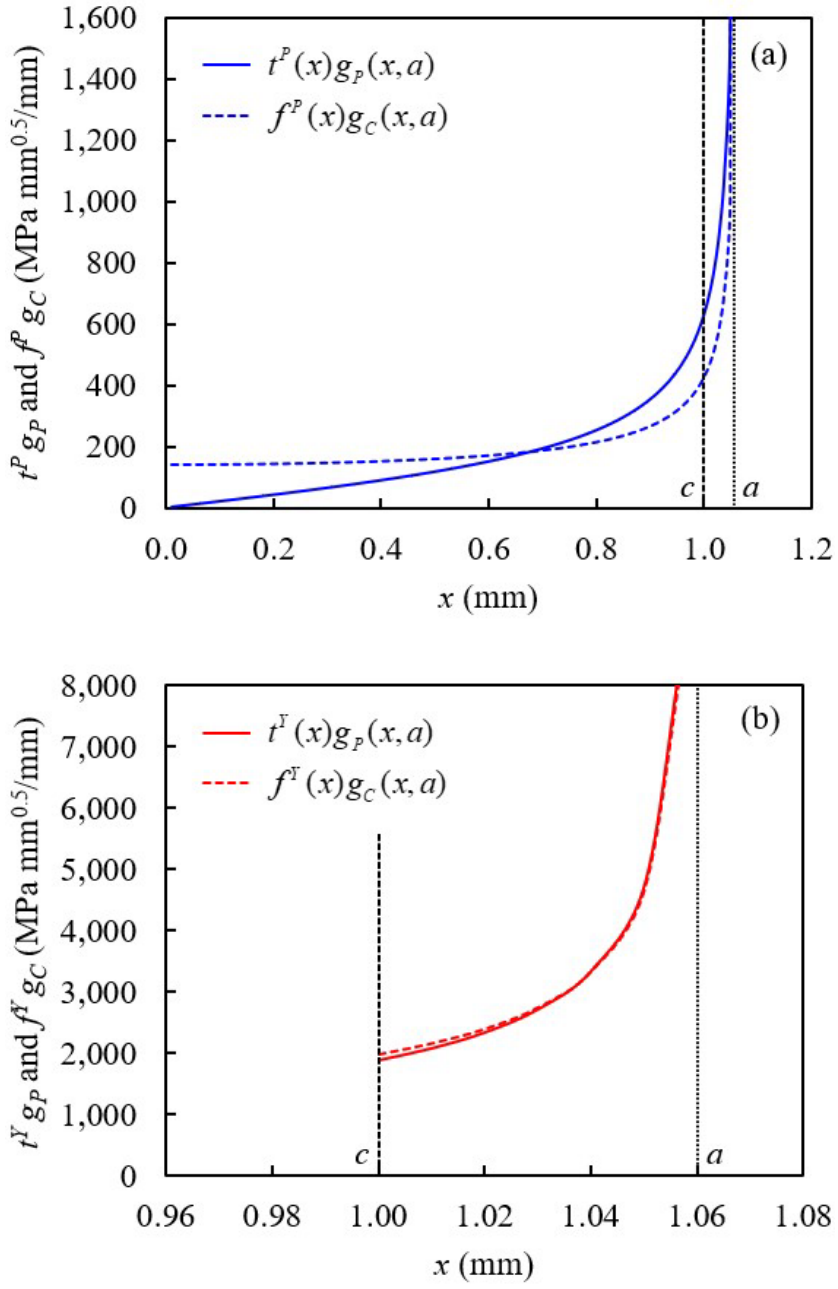

Fig. 4.7 Comparison of integrands used in the calculation of SIFs for a penny-shaped crack with c = 1.0 mm under σ^P = 200 MPa: **(a)** external stress case showing $t^P(x)g_P(x,a)$ and $f^P(x)g_C(x,a)$; **(b)** cohesive stress case showing $t^Y(x)g_P(x,a)$ and $f^Y(x)g_C(x,a)$

Fig. 4.8 presents a comparison between the reference a–K relationships and those reconstructed using EDSs with the 2D center-through crack weight function. The reproduced SIFs show excellent agreement with the analytical reference values, thereby confirming the validity and robustness of the proposed EDS determination method for practical use in 3D crack problems.

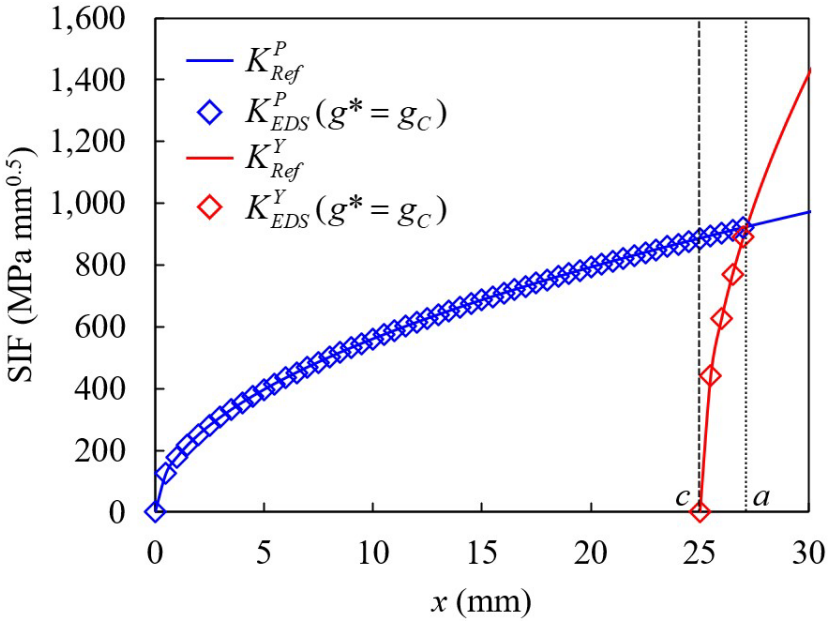

Fig. 4.8 Comparison of reference a–K relationships of the target 3D penny-shaped crack with reproduced a–K relationships obtained using EDSs applied to the substituted 2D center-through crack model (c = 1.0 mm, σ^P = 200 MPa)

4.4 Comparison of Elastic-Plastic COD Profiles

To evaluate the effectiveness of the proposed EDS-based fracture analysis system, this section compares elastic-plastic COD profiles obtained using the EDS method with analytical reference solutions. In the EDS analysis, CODs are computed using **Eqs. (3.31) – (3.36)**, incorporating the weight function of the 2D center-through crack model. The simulations are conducted under remote tensile stresses of σ^P = 160, 200, and 240 MPa.

The resulting elastic-plastic COD profiles and corresponding EPFM parameters are compared against analytical solutions derived by Sneddon [78], which are presented in **Appendix B**. The results of this comparison are presented in **Fig. 4.9** and **Table 4.1**. As shown, the COD profiles and EPFM parameters predicted by the EDS method exhibit excellent agreement with the reference solutions for the 3D penny-shaped crack.

These findings validate the accuracy and reliability of the developed EDS-based framework. The close match between the EDS results and analytical benchmarks confirms that the proposed method offers a robust and computationally efficient alternative for EPFM analysis of 3D cracks.

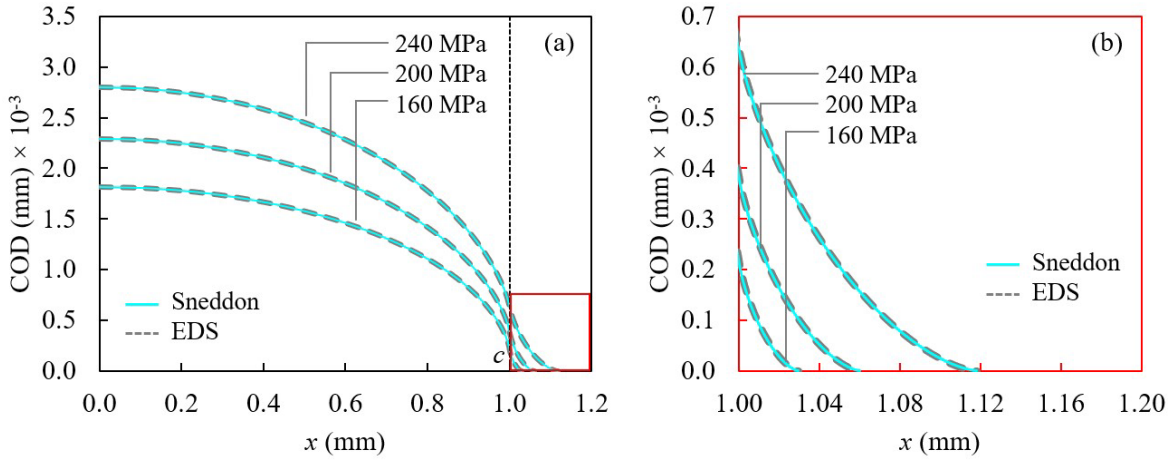

Fig. 4.9 Comparison of CODs of the 3D penny-shaped crack obtained from the EDS method and Sneddon's solution: **(a)** full profile; **(b)** magnified view ahead of the crack tip

Table 4.1 Comparison of r_p and CTOD of the 3D penny-shaped crack obtained using the EDS method and Sneddon's solution

σ^P (MPa)	λ	r_p (mm) × 10^{-3}		CTOD (mm) × 10^{-3}	
		EDS	Sneddon	EDS	Sneddon
160	1.716	29.540	29.540	0.217	0.217
200	1.537	60.154	60.154	0.384	0.384
240	1.368	118.243	118.243	0.638	0.638

4.5 Summary

This chapter presented the validation of the developed EDS-based EPFM analysis framework for 3D cracks. A 3D penny-shaped crack in an infinite plate under axisymmetric loading was adopted as the verification case owing to its simple geometry and the availability of an analytical weight function, which enabled a detailed and systematic demonstration of the EDS analysis procedures.

To enhance computational efficiency, a 2D center-through crack in an infinite plate—featuring a well-established and computationally efficient weight function—was employed as a substitute model for the 3D penny-shaped crack. Prescribed a–K relationships for both external and cohesive stresses were analytically derived using the original weight function of the penny-shaped crack and were successfully reproduced on the 2D model using the FLM-based EDS formulation.

The elastic-plastic COD profiles obtained through the EDS-based CZM framework were subsequently compared with the analytical solutions by Sneddon. Across a range of applied remote stress levels, the EDS-derived CODs and associated EPFM parameters showed excellent agreement with the analytical results.

These results confirm the reliability, physical fidelity, and computational efficiency of the proposed EDS-based fracture analysis framework. This chapter demonstrates that the developed method offers a robust and practical alternative for the EPFM analysis of 3D cracks, laying a solid foundation for extending its application to a wider range of crack configurations commonly encountered in engineering structures.

CHAPTER 5

EDS ANALYSIS OF 3D SURFACE CRACKS

5.1 Extension of the EDS Method to 3D Surface Cracks

In the previous chapter, the effectiveness of the EDS method for analyzing axisymmetric 3D crack, specifically penny-shaped crack, was successfully demonstrated. This validation established a foundational framework for applying the EDS concept to EPFM problems involving 3D geometries. However, extending the FLM-based EDS methodology to crack configurations more commonly encountered in engineering applications remains a significant challenge.

Among these, surface cracks are particularly prevalent in steel structural components, often initiating as shallow flaws with low aspect ratios and evolving over time [79–81]. Numerous experiments and numerical investigations have shown that crack growth predominantly occurs in the depth direction under tension loading, as the SIF is higher at the deepest point for most aspect ratios until they approach an aspect ratio of 1.0 [82–85].

This chapter investigates the applicability of the EDS method to such practical surface crack scenarios. The analysis focuses on both the deepest and corner points of semi-elliptical surface cracks, enabling a detailed assessment of key EPFM parameters including plastic zone size and CTOD. The reference a–K relationships for external and cohesive stresses are analyzed using WARP3D [86], within the framework of the FLM approach.

In the EDS analysis, a 2D edge crack in a semi-infinite plate and a center-through crack in an infinite plate are considered as substitute crack models to thoroughly examine the elastic-plastic crack opening behavior and assess their computational efficiency for analyzing 3D surface cracks. Due to similar boundary conditions and geometry, the 2D edge crack is employed as a substitute model for 3D surface cracks, with the expectation of achieving a comparable COD profile along the crack face [87,88].

However, in the context of FCP, the accurate prediction of EPFM parameters—particularly the plastic zone size and CTOD—is essential, as these parameters strongly influence the SIF and the crack opening behavior. The accuracy of the COD at the crack mouth, while useful for visualization, is less critical since it does not reflect the localized mechanical fields near the crack front. Therefore, EDS analysis is also conducted using the

2D center-through crack model. If both substitute models yield consistent predictions for the essential EPFM parameters, the center-through model offers a more straightforward and computationally efficient alternative by eliminating the need for numerical integration through the use of closed-form solution.

By applying and refining the EDS methodology to non-axisymmetric 3D surface crack problems, this chapter addresses a notable gap in the literature and extends the practical capabilities of the EDS framework. These developments not only enhance the original SYM-based approach but also provide a robust basis for integration into fatigue life prediction tools for complex structural systems.

5.2 Configuration of Target Surface Cracks

To investigate the applicability of the EDS method to 3D surface cracks, a semi-elliptical surface crack embedded in a semi-infinite plate is considered, as illustrated in **Fig. 5.1**. The geometry is carefully selected to ensure that the stress distribution around the crack remains unaffected by the finite boundaries of the plate, thereby approximating a semi-infinite body condition suitable for EDS analysis.

The coordinate system is defined such that the origin, O, lies at the midpoint of the surface crack along the y-axis. c_1 and c_2 represent the physical crack lengths in the positive x-direction (depth) and y-direction (width), respectively. Five surface crack models are prepared with initial aspect ratios (c_1/c_2) of 0.2, 0.4, 0.6, 0.8 and 1.0 to represent a range of practical crack shapes from shallow to semi-circular. For consistency, the crack width c_2 is fixed at 1.0 mm in all models, while the crack depth c_1 varies from 0.2 mm to 1.0 mm in increments of 0.2 mm.

In this study, the EDS analysis is performed at two critical locations along the crack front: the deepest point (on the x-axis) and the corner point (intersection with the free surface), capturing the variation in local constraint and crack-tip plasticity across the crack front. This dual-point analysis enables a more comprehensive understanding of the EPFM parameters, particularly the plastic zone size and CTOD, under the influence of 3D surface crack geometry. For simplicity and consistency with the Dugdale CZM, the material is assumed to behave as an elastic-perfectly plastic body without strain hardening. The material properties used in the EDS calculations are as follows: E = 206,000 MPa, σ^Y = 392 MPa, and ν = 0.3.

This idealized material model allows clear interpretation of plastic zone development and cohesive stress distribution, providing a robust basis for comparison with the EDS-derived results.

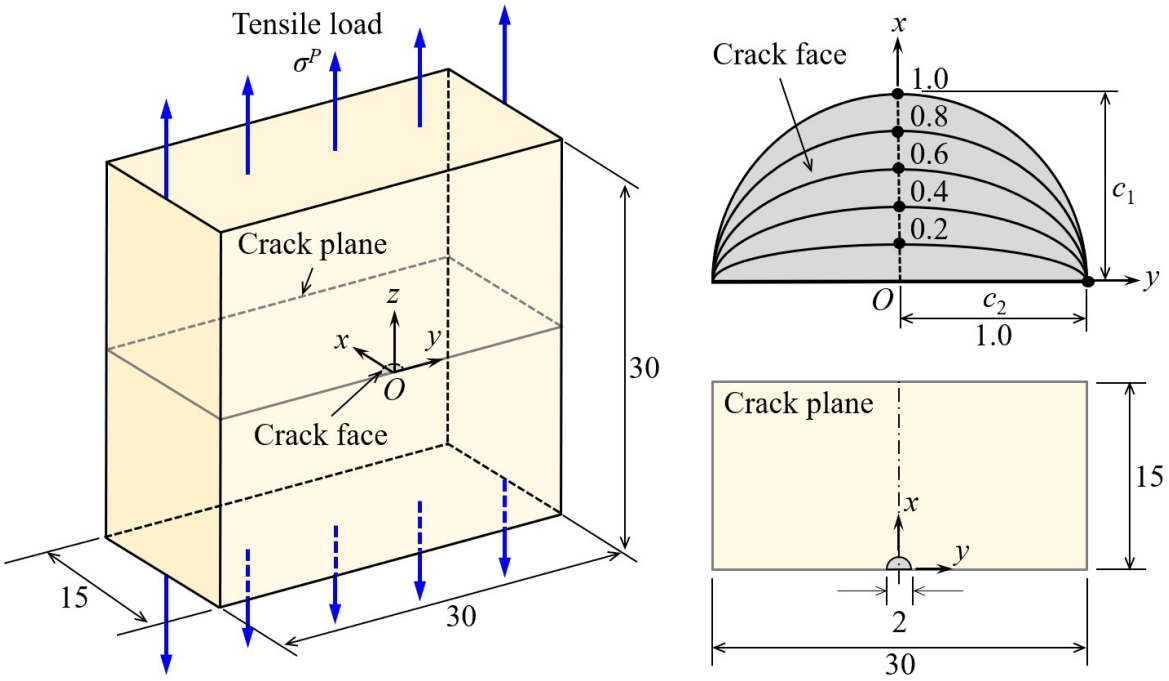

Fig. 5.1 Configuration of a 3D surface crack in a semi-infinite plate under uniform tensile loading σ^P (dimensions in mm)

5.3 Elastic-Plastic FE Analysis for Reference Solutions

To obtain the reference CODs and corresponding EPFM parameters for comparison with the EDS results, elastic-plastic FE analysis is conducted using MSC Marc [89]. The FE mesh is generated using TSV-Crack [90], and 10-node tetrahedral (TET10) element type is employed. As shown in **Fig. 5.2**, an extra fine mesh is constructed in the vicinity of the physical crack front to capture the localized stress-strain behavior accurately. The minimum element size near the crack front is set to 0.005 mm to ensure high fidelity in the computed reference data.

The reliability of the developed mesh is also validated by comparing the SIFs calculated using the virtual crack closure-integral method for quadratic tetrahedral elements [91,92] with the well-known Newman-Raju solutions [93]. The comparison indicates a negligible discrepancies of approximately 1.0% or less at both the deepest and corner points of the crack front across all aspect ratio models.

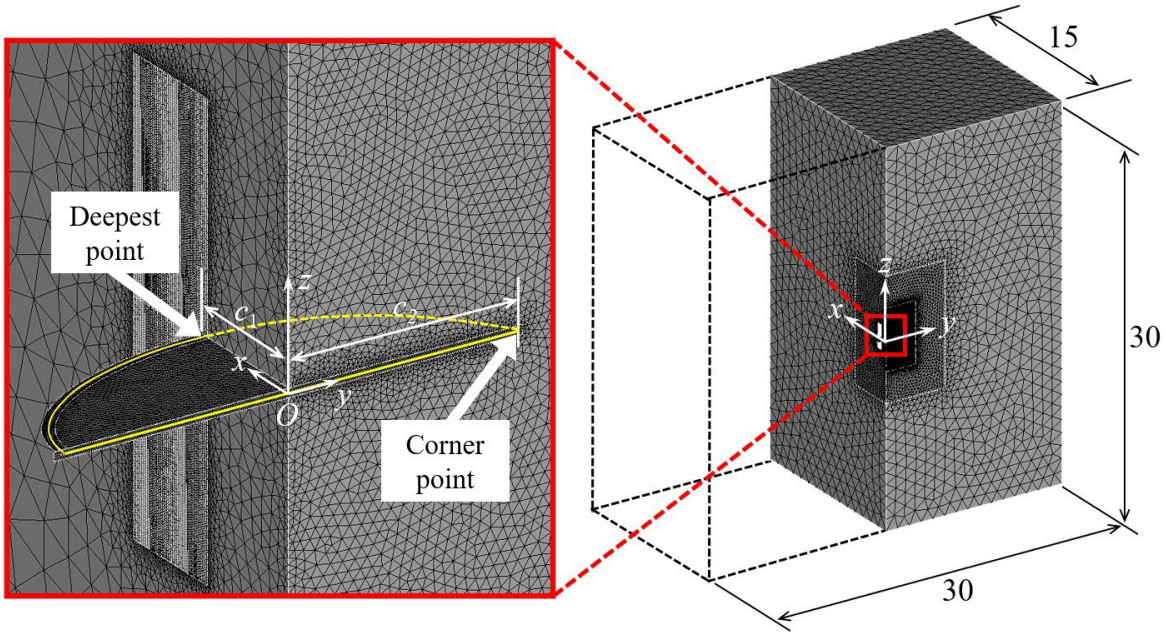

Fig. 5.2 FE mesh of a 3D surface crack model with an aspect ratio c_1/c_2, showing the global mesh distribution and local refinement near the crack front (dimensions in mm)

5.3.1 Determination of Elastic-Plastic COD Profile in FE Analysis

To characterize the COD in a cracked structure under elastic-plastic conditions, the displacement field along the crack faces must be carefully extracted from the FE analysis results. The actual COD in the physical crack region, denoted as V_A, is obtained by extracting the relative displacement of nodes located on the opposing crack faces along the x- and y-directions.

Beyond the physical crack tip, the COD is no longer directly measurable and must be estimated through a fictitious extension of the crack. In this region, the fictitious COD, referred to as V_F, is evaluated based on the accumulated plastic strain in the ligament ahead of the crack tip, using the following expression [94].

$$V_F = 2\left\{\int_0^{\infty} \varepsilon_{zz}^{p} dz\right\}\left(1+\frac{\sigma^{Y}}{E'}\right) \tag{5.1}$$

where ε_{zz}^{p} denotes the component of plastic strain in the z-direction beyond the physical crack tip. The parameter E' is the effective modulus under plane strain conditions, as previously defined in **Eq. (3.32)**. This formulation allows the representation of the crack opening in the plastic zone beyond the actual crack front.

At the junction between the physical and fictitious crack regions lies the physical crack tip, where the COD is referred to as the CTOD. Since the mesh node corresponding to the physical crack tip typically exhibits zero displacement in FE analysis, the CTOD is computed by linearly interpolating the displacements of adjacent nodes near the crack tip. This approach provides a continuous and smooth COD profile, seamlessly connecting the physical crack region to the plastic zone ahead of the crack tip. A comprehensive depiction of the definitions V_A, V_F, and CTOD in the FE analysis is provided in **Fig. 5.3**.

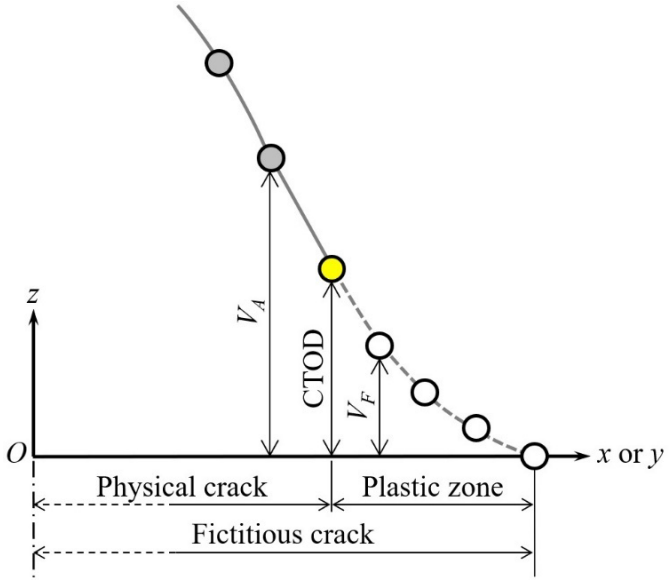

Fig. 5.3 Schematic illustration of the definitions of V_A, V_F, and CTOD in FE analysis

5.3.2 Investigation of Actual Plastic Zone Shape

In the FLM-based EDS analysis framework, an accurate understanding of the plastic (or cohesive) zone characteristics is crucial for establishing cohesive stress *a*–*K* relationships. To address this, the actual shapes of plastic zones for target surface cracks under specific loading conditions are examined through detailed elastic-plastic FE analysis.

Fig. 5.4 illustrates the plastic zone shapes as viewed from the *xy*-plane for σ^P values of 100, 200, and 300 MPa. These visualizations reveal how the size and geometry of the plastic zones evolve with increasing applied load. The variation in plastic zone morphology is strongly influenced by the crack aspect ratio and the corresponding distribution of SIFs along the crack front. In general, under tensile loading, cracks with lower aspect ratios exhibit a tendency for the plastic zone to extend more prominently in the depth direction. In contrast, when the aspect ratio approaches unity (a nearly circular crack front), the plastic zone expansion becomes more pronounced along the width direction.

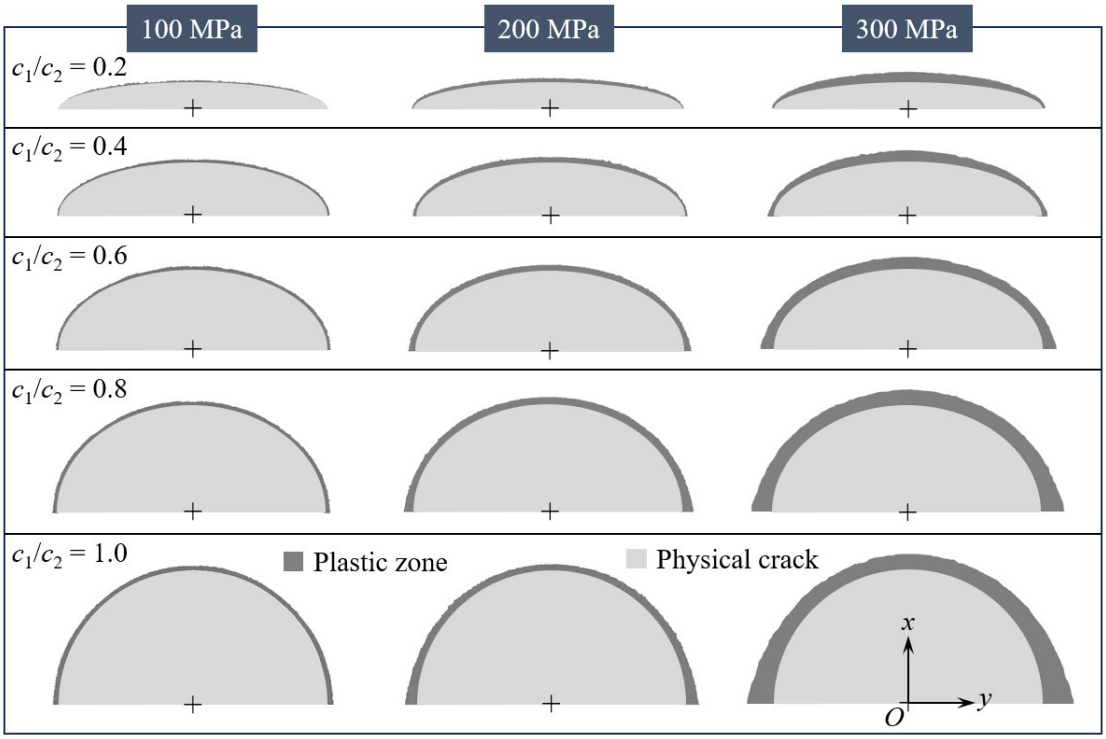

Fig. 5.4 Plastic zone shapes (*xy*-view) of surface cracks obtained from FE analysis

Fig. 5.5 examples a comprehensive view of the 3D plastic zone shape along the crack front for a surface crack with a c_1/c_2 ratio of 0.6 under a tensile load of σ^P = 200 MPa. Here, a_1 and a_2 represent the fictitious crack lengths in the positive *x*- and *y*-directions, respectively. The minimum element size close to the physical crack front is 0.005 mm, and the average size is 0.01 mm.

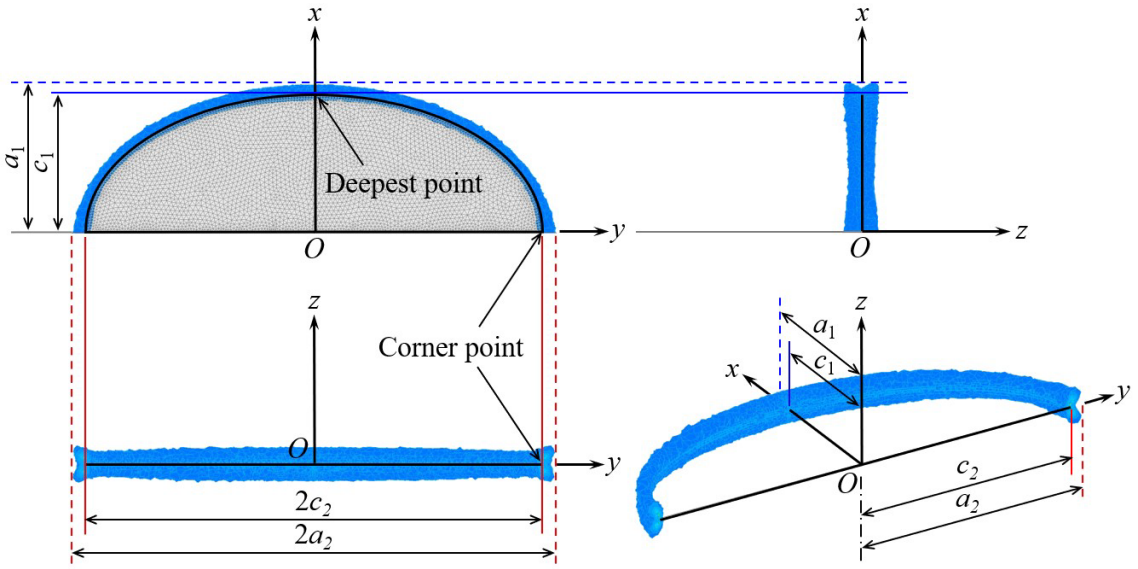

Fig. 5.5 Configuration of the 3D plastic zone shape along the crack front of a surface crack obtained from FE analysis (c_1/c_2 = 0.6, σ^P = 200 MPa)

To facilitate a clearer comparison, the plastic zone shapes at both the deepest point and the corner of the crack front are projected onto a single reference plane, as illustrated in **Fig. 5.6**. r_{px} and r_{py} refers to the plastic zone size in the x- and y-directions, respectively. Due to variations in SIFs along the crack front, which depend on the aspect ratio, it can be observed that the plastic zone extends further in the depth direction (x-direction) up to a c_1/c_2 ratio of 0.6 but begins to extend more in the width direction (y-direction) as the c_1/c_2 ratio reaches 0.8.

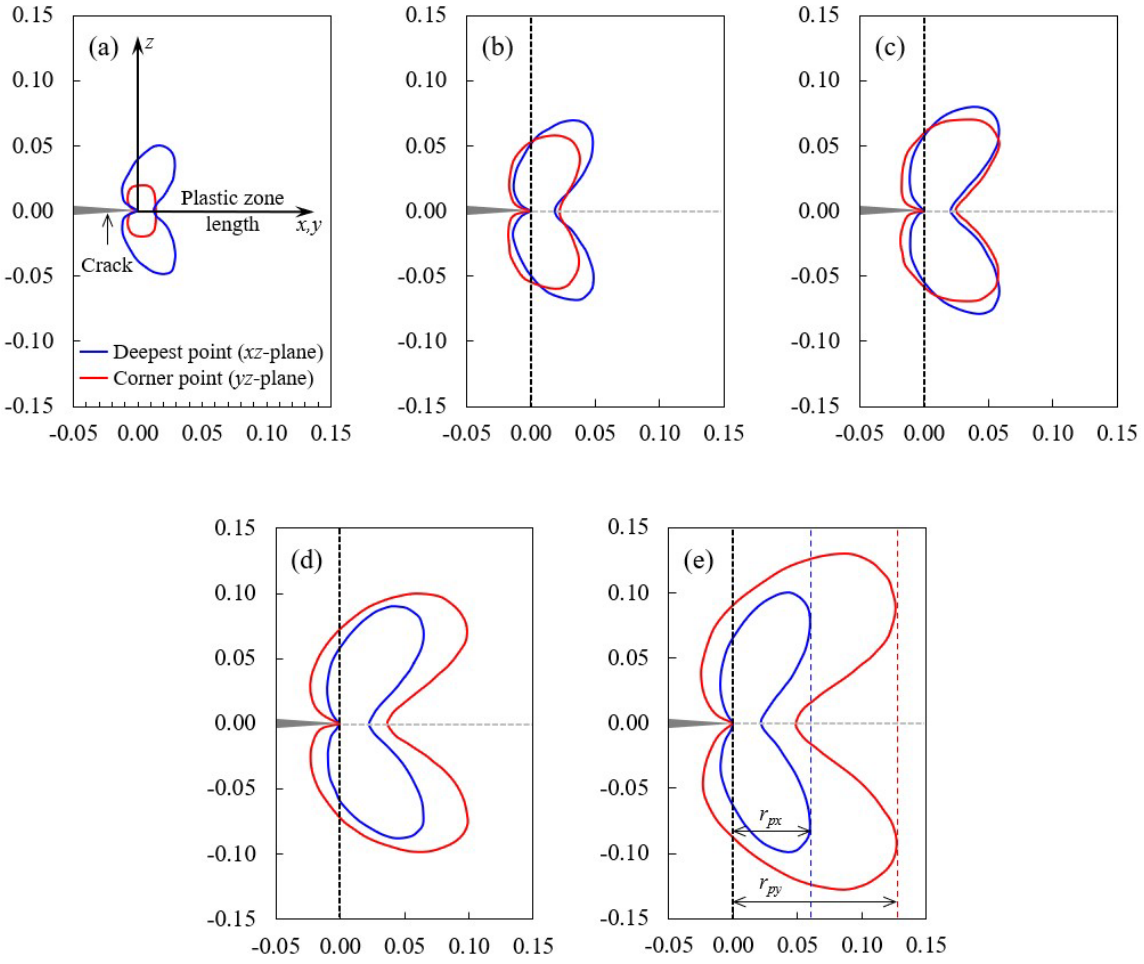

Fig. 5.6 Plastic zone shapes at the deepest and corner points of surface cracks from FE analysis: **(a)** $c_1/c_2 = 0.2$; **(b)** $c_1/c_2 = 0.4$; **(c)** $c_1/c_2 = 0.6$; **(d)** $c_1/c_2 = 0.8$; **(e)** $c_1/c_2 = 1.0$

5.3.3 Determination of Plastic Constraint Factor

In the evaluation of elastic-plastic crack behavior, the plastic constraint factor λ plays a critical role in characterizing the stress triaxiality at various points along the crack front. At the corner point of a surface crack, the stress state is assumed to be close to plane stress; therefore, λ is taken as 1.0.

In contrast, at the deepest point of the physical crack—where the stress state tends toward plane strain—the constraint is more severe and must be evaluated quantitatively. In this study, λ at the deepest point is determined by matching the results of FE analysis with the analytical formulation shown below [75].

$$\lambda = \frac{\sigma^P}{\sigma^Y \sqrt{1-\left(\frac{c}{a}\right)^2}} \tag{5.2}$$

Fig. 5.7 presents the calculated values of λ obtained from **Eq. (5.2)** for different normalized applied stress levels, specifically for σ^P/σ^Y ratios ranging from 0.2 to 0.8. The results reveal a nearly linear decrease in λ with increasing applied stress, indicating a progressive relaxation of constraint as plasticity becomes more dominant.

For practical implementation within the EDS framework, the variation of λ with applied stress is approximated using a linear regression fit. The resulting values are subsequently incorporated into the EDS analysis for the crack deepest point to ensure accurate representation of the constraint effect near the crack front.

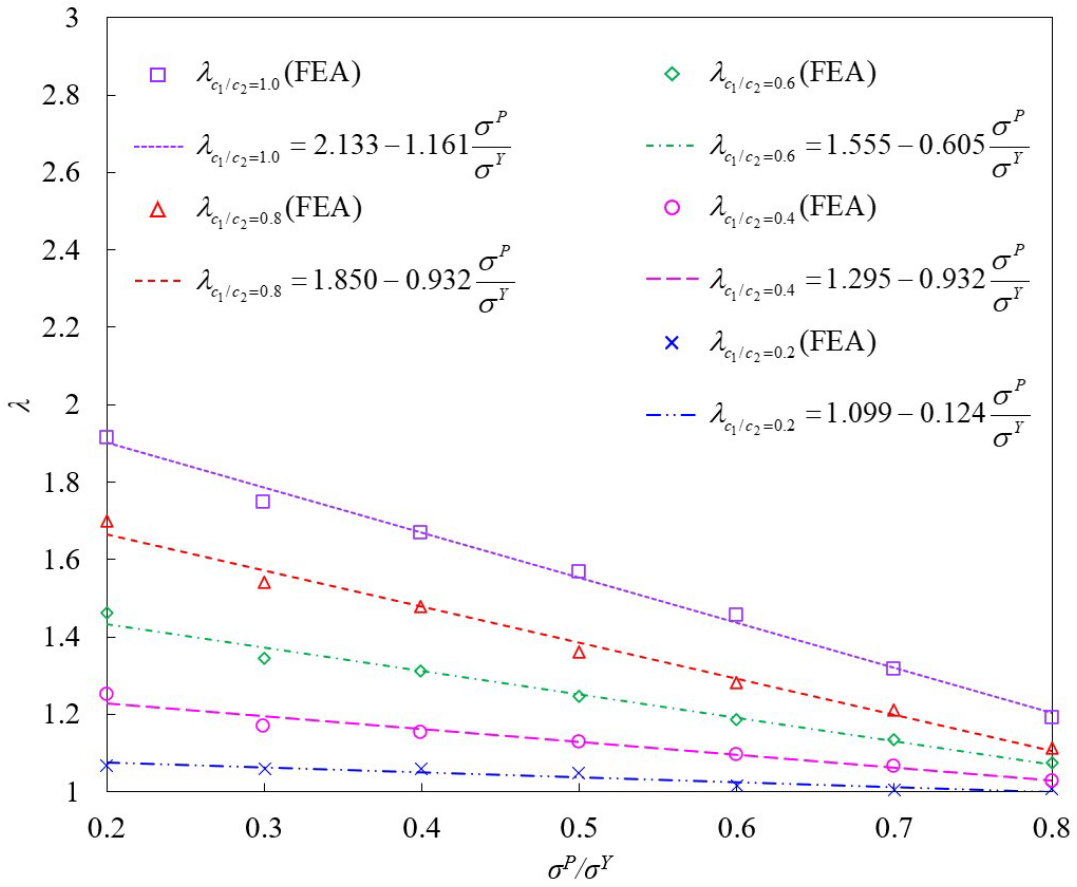

Fig. 5.7 Solutions of plastic constraint factors for the deepest point of target surface cracks

5.4 Calculation of Prescribed *a–K* Relationships

To enable accurate application of the EDS method in surface crack analysis, it is essential to establish the prescribed *a–K* relationships for both external and cohesive stresses. These relationships are developed using LEFM analysis, employing the interaction integral method [95] together with the CFT-integral formulation [96,97], implemented in the public-domain FE code WARP3D.

Fig. 5.8 illustrates an example of the specific locations along both the crack depth and width directions where the *a–K* relationships are computed, in the case of a surface crack with an aspect ratio of $c_1/c_2 = 0.8$. As noted in the preceding sections, the actual cohesive (plastic) zone shape evolves non-uniformly along the crack front, depending on the aspect ratio and loading conditions. This variation renders it impractical to predetermine the plastic zone shape a priori. To address this, a simplified and idealized model of the plastic zone is adopted to facilitate consistent development of the prescribed *a–K* relationships required in the EDS analysis.

Specifically, a Dugdale-type cohesive zone is assumed to extend an equal distance ahead of the physical crack front along the entire crack front, as depicted in **Fig. 5.8**. This assumption implies that the distance between the physical and fictitious crack fronts remains constant for each increment along crack front, regardless of the parametric angle ϕ. Based on this simplified geometry, the *a–K* relationships are computed by applying the following loading conditions:

$$\begin{aligned} &t^P = \sigma^P, \text{ in the region } (x,y): \frac{x^2}{a_1^{\,2}} + \frac{y^2}{a_2^{\,2}} \le 1,\ x \ge 0 \\ &t^Y = \lambda\sigma^Y, \text{ in the region } (x,y): \frac{x^2}{c_1^{\,2}} + \frac{y^2}{c_2^{\,2}} \ge 1, \text{ and } \frac{x^2}{a_1^{\,2}} + \frac{y^2}{a_2^{\,2}} \le 1,\ x \ge 0 \end{aligned} \tag{5.3}$$

Within the physical crack region, the *a–K* relationships for external stresses are determined by incrementally extending the crack front in accordance with the actual aspect ratio c_1/c_2. Beyond the physical crack front, where the cohesive zone is defined, the *a–K* relationships for both external and cohesive stresses are developed by uniformly extending the crack front. This approach ensures that the cohesive zone representation in the EDS analysis accurately captures SIFs at the fictitious crack tip. To this end, the fictitious crack front is extended in very small increments over a predefined distance, providing sufficient

resolution to characterize the cohesive region across the range of applied stress levels considered.

To realize this, WARP3D has been enhanced to compute the equivalent nodal forces resulting from partially applied CFT stresses on an element face using numerical surface integration with ultra-high order Gauss-Legendre quadrature (up to 64 points) [88]. Consistent with the Dugdale assumption, cohesive stress is applied as $\lambda\sigma^Y$ in the loading direction, and the *a–K* relationships for cohesive stresses are computed using a 0.01 mm increment of the fictitious crack front.

For completeness and clarity, the resulting SIFs along the crack front for both external and cohesive stresses are provided in **Appendix C**. These results are tabulated at 0.05 mm increments of the fictitious crack front, offering a detailed characterization of the SIF distribution along the crack front and serving as a structured foundation for subsequent evaluation in the EDS analysis.

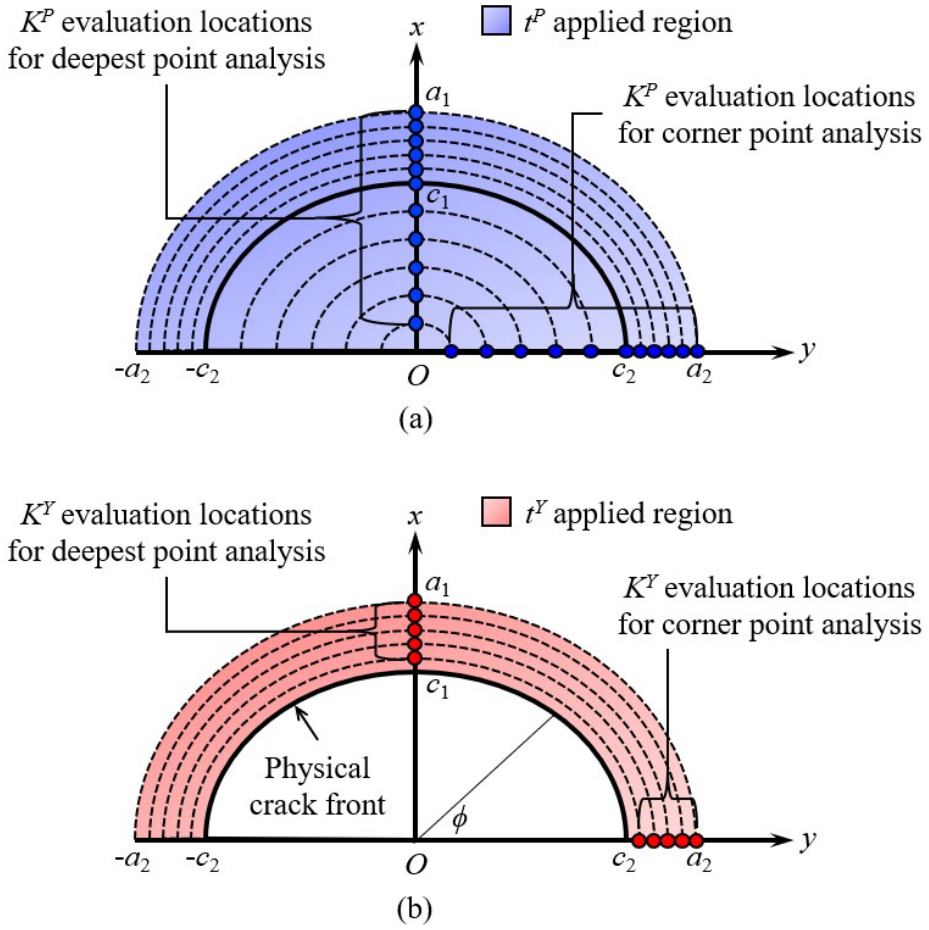

Fig. 5.8 Arrangement of evaluation locations for prescribed *a–K* relationships in the depth and width directions of a surface crack: **(a)** for K^P; **(b)** for K^Y ($c_1/c_2 = 0.8$)

5.5 EDS Analysis of Surface Cracks at the Deepest Point

This section presents the application of the EDS method to surface cracks, with a focus on the deepest point along the crack front. As one of the most critical locations for evaluating fracture behavior, the deepest point typically experiences higher constraint and stress intensity, making it essential for accurate prediction of EPFM parameters. Building upon the prescribed *a*–*K* relationships developed in the preceding sections, the EDS analysis is carried out using the weight functions of two substitute crack models, g_C and g_E. The performance and accuracy of each model in representing the 3D crack opening behavior at the deepest point are also discussed.

5.5.1 EDS and Reproduced a–K Relationships for the Deepest Point

In the EDS analysis, spline partition points are set at coarser intervals than the SIF calculation points. For cracks with c_1/c_2 ratios of 0.2 and 0.4, the points are placed at 0.1 mm intervals, whereas for cracks with c_1/c_2 ratios of 0.6, 0.8, and 1.0, they are placed at 0.2 mm intervals, ensuring appropriate spacing based on the crack size.

Figs. 5.9 – 5.13 show the applied CFTs (t^P and t^Y) and EDSs (f^P and f^Y) for $\sigma^P = 200$ MPa, with c_1/c_2 ratios ranging from 0.2 to 1.0. The results demonstrate that smooth and continuous EDS distributions are calculated for both external and cohesive stresses.

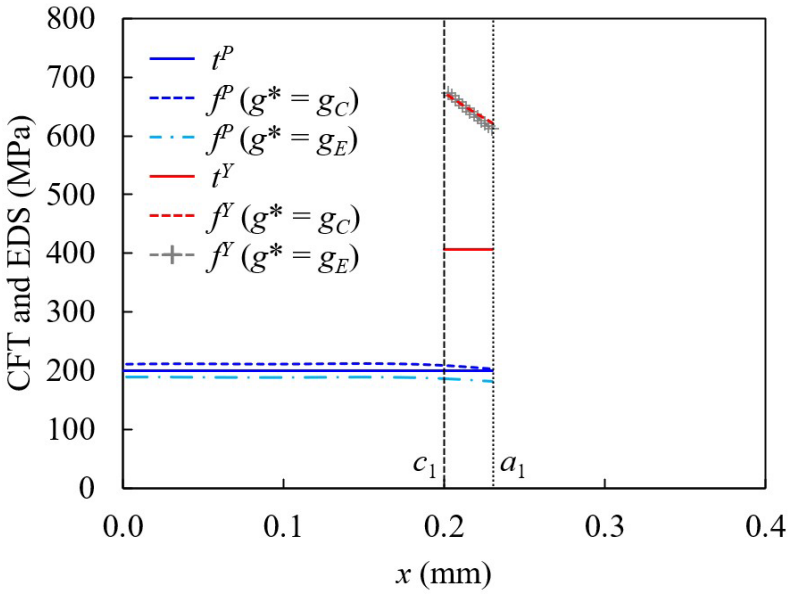

Fig. 5.9 Comparison of applied CFTs and calculated EDSs along the depth direction of a 3D surface crack in a semi-infinite plate under uniform tensile loading ($c_1/c_2 = 0.2$, $\sigma^P = 200$ MPa)

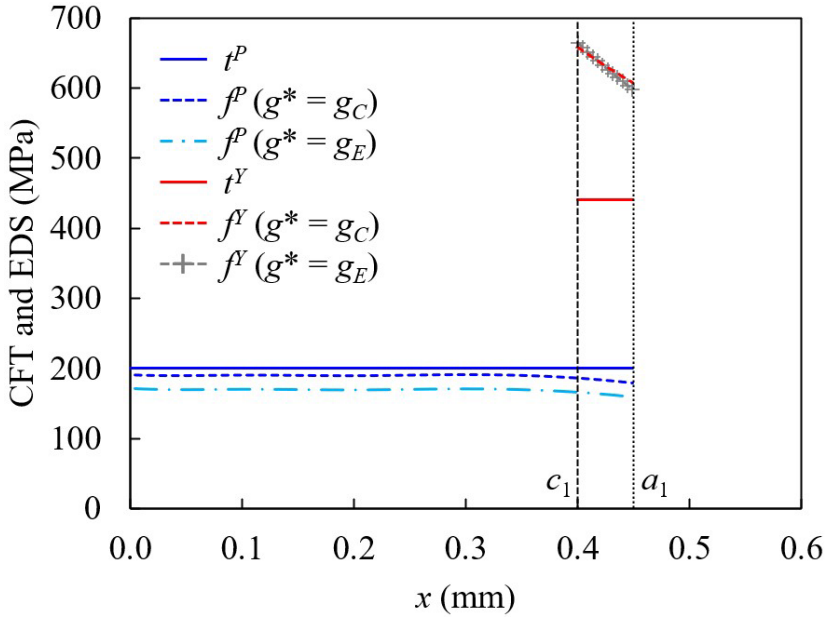

Fig. 5.10 Comparison of applied CFTs and calculated EDSs along the depth direction of a 3D surface crack in a semi-infinite plate under uniform tensile loading ($c_1/c_2 = 0.4$, $\sigma^P = 200$ MPa)

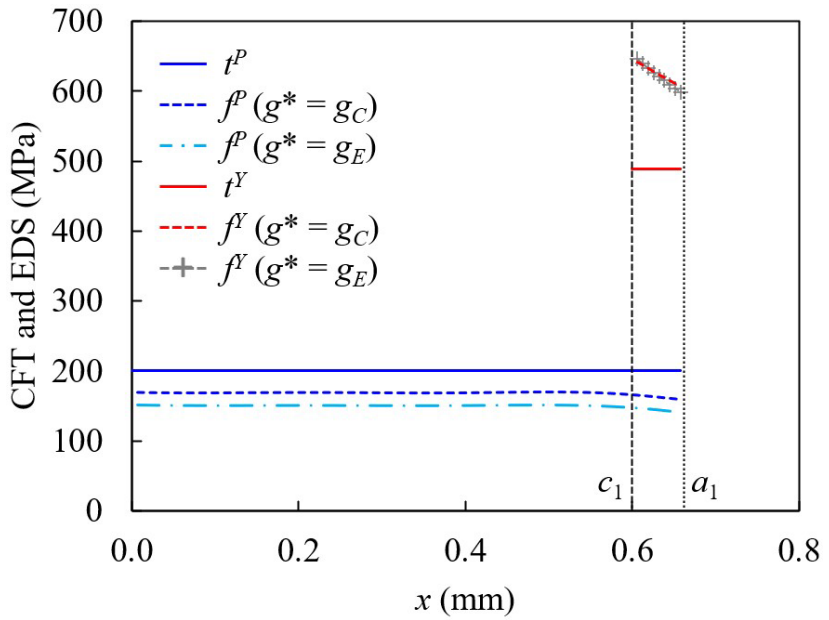

Fig. 5.11 Comparison of applied CFTs and calculated EDSs along the depth direction of a 3D surface crack in a semi-infinite plate under uniform tensile loading ($c_1/c_2 = 0.6$, $\sigma^P = 200$ MPa)

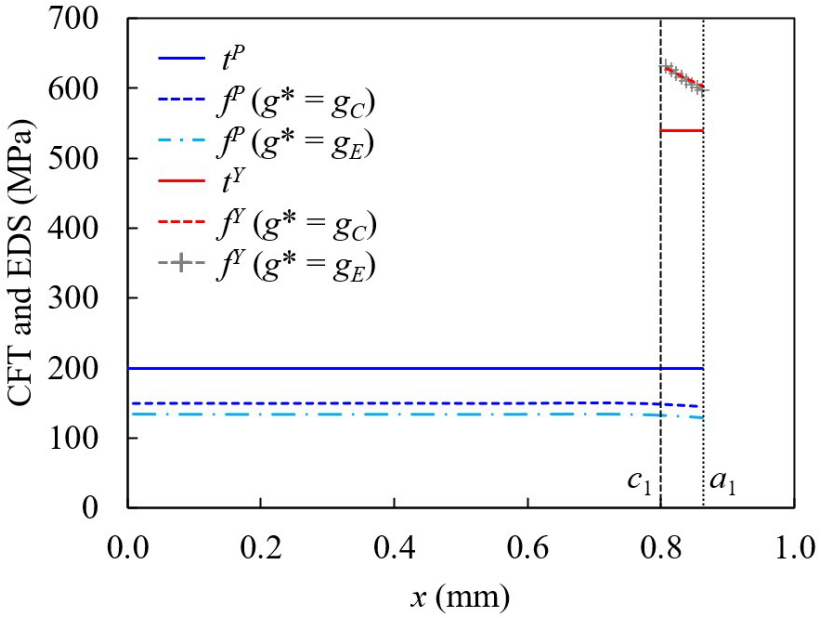

Fig. 5.12 Comparison of applied CFTs and calculated EDSs along the depth direction of a 3D surface crack in a semi-infinite plate under uniform tensile loading ($c_1/c_2 = 0.8$, $\sigma^P = 200$ MPa)

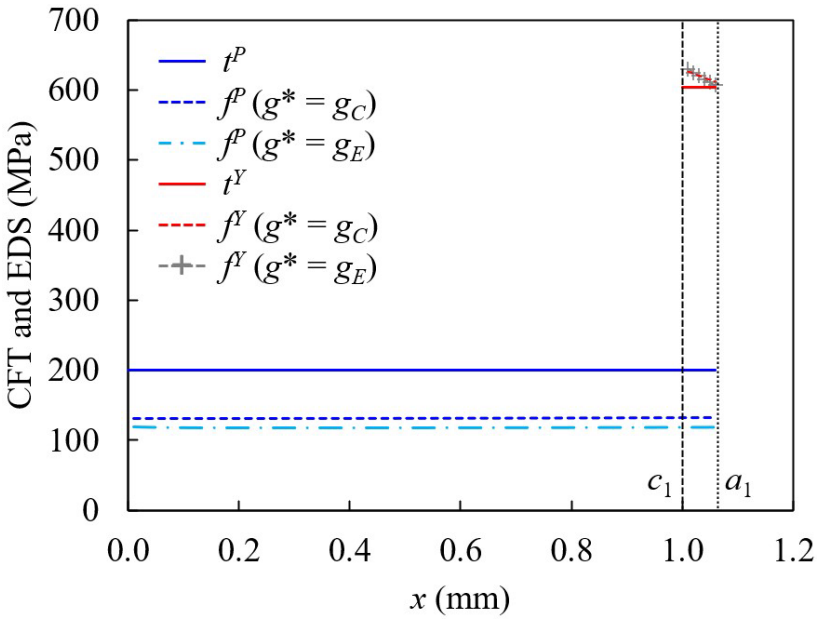

Fig. 5.13 Comparison of applied CFTs and calculated EDSs along the depth direction of a 3D surface crack in a semi-infinite plate under uniform tensile loading ($c_1/c_2 = 1.0$, $\sigma^P = 200$ MPa)

Figs. 5.14 – 5.18 present the comparison between the prescribed a–K relationships and those reproduced by the EDS method using the weight functions of the 2D edge crack (g_E) and center-through crack (g_C). As described in the previous sections, the prescribed a–

K relationship inputs are defined up to a certain distance beyond the physical crack tip. The a–K relationships reproduced by the EDS method terminate at the end of the cohesive zone, where the stress singularity disappears under the given stress level. The calculated SIFs demonstrate a strong correlation with the prescribed inputs, validating the effectiveness and reliability of the developed EDS determination system.

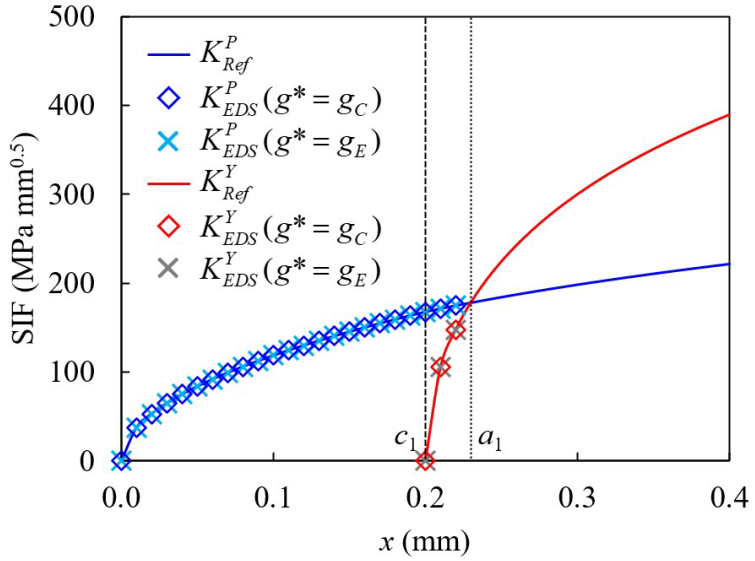

Fig. 5.14 Comparison of reference a–K relationships along the depth direction of a 3D surface crack with reproduced a–K relationships obtained using EDSs applied to substituted 2D center-through and edge crack models (c_1/c_2 = 0.2, σ^P = 200 MPa)

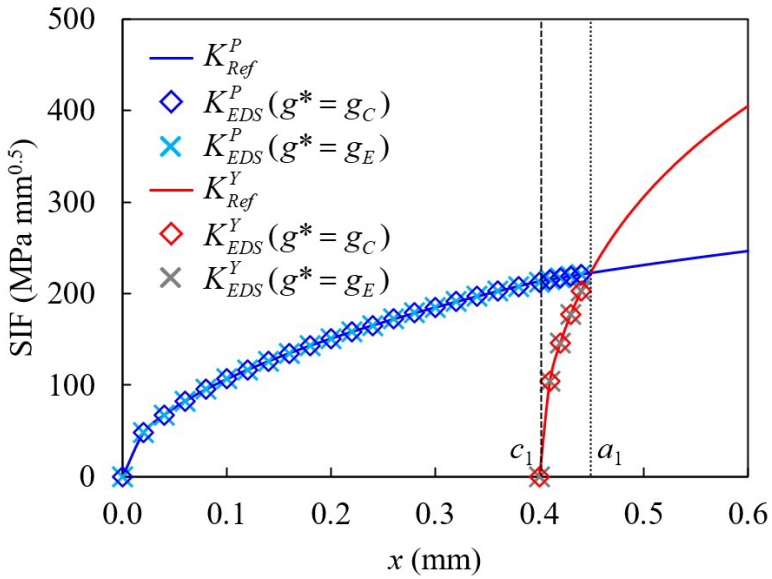

Fig. 5.15 Comparison of reference a–K relationships along the depth direction of a 3D surface crack with reproduced a–K relationships obtained using EDSs applied to substituted 2D center-through and edge crack models (c_1/c_2 = 0.4, σ^P = 200 MPa)

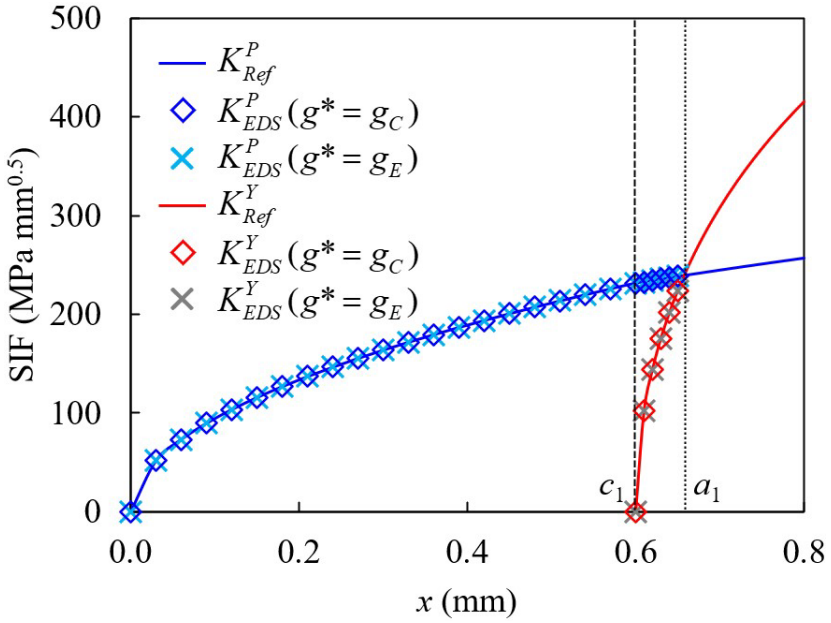

Fig. 5.16 Comparison of reference *a*–*K* relationships along the depth direction of a 3D surface crack with reproduced *a*–*K* relationships obtained using EDSs applied to substituted 2D center-through and edge crack models ($c_1/c_2 = 0.6$, $\sigma^P = 200$ MPa)

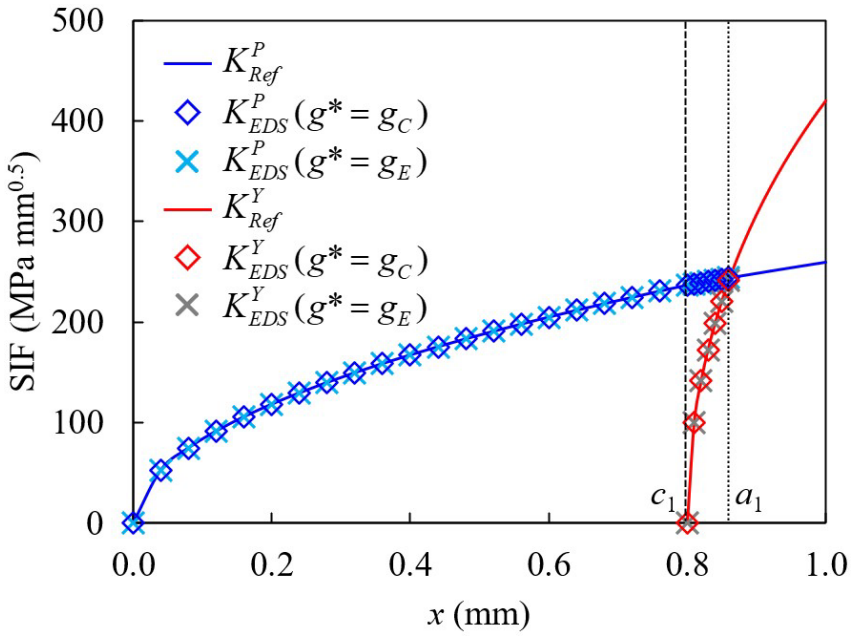

Fig. 5.17 Comparison of reference *a*–*K* relationships along the depth direction of a 3D surface crack with reproduced *a*–*K* relationships obtained using EDSs applied to substituted 2D center-through and edge crack models ($c_1/c_2 = 0.8$, $\sigma^P = 200$ MPa)

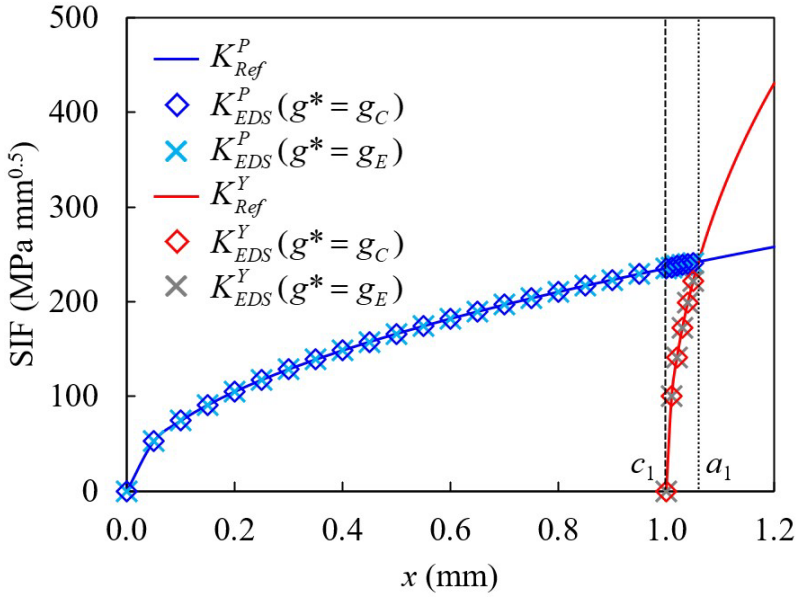

Fig. 5.18 Comparison of reference *a*–*K* relationships along the depth direction of a 3D surface crack with reproduced *a*–*K* relationships obtained using EDSs applied to substituted 2D center-through and edge crack models (c_1/c_2 = 1.0, σ^P = 200 MPa)

5.5.2 Comparison of EPFM Parameters for the Deepest Point

In the EDS analysis, elastic-plastic CODs induced by EDSs are calculated through **Eqs. (3.31) – (3.36)** from **Chapter 3**, based on the weight functions of 2D center-through and edge cracks. Surface cracks with c_1/c_2 ratios of 0.2, 0.4, 0.6, 0.8, and 1.0 are analyzed under three loading conditions (σ^P = 160, 200, and 240 MPa). The results are then compared with the reference FE analysis solutions along the depth direction.

Figs. 5.19 – 5.23 show comparisons between the elastic-plastic CODs calculated using the EDS method and the reference FE solutions. The COD profiles along the crack face, obtained via the edge crack weight function, closely match the FE results and exhibit better agreement than those derived from the center-through crack. However, it is evident that the key EPFM parameters (r_p and CTOD) can be accurately determined regardless of whether an edge crack or a center-through crack is used as the substitute crack. The values obtained are nearly identical ahead of the physical crack tip, with a percentage difference of approximately 0.01% across all cases.

Therefore, employing a center-through crack as the substitute body in the EDS analysis is advantageous as it leverages closed-form solutions to simplify calculations while maintaining the necessary accuracy for r_p and CTOD. This also provides significant advantages for future implementation in FCP analysis involving multiple loading cycles.

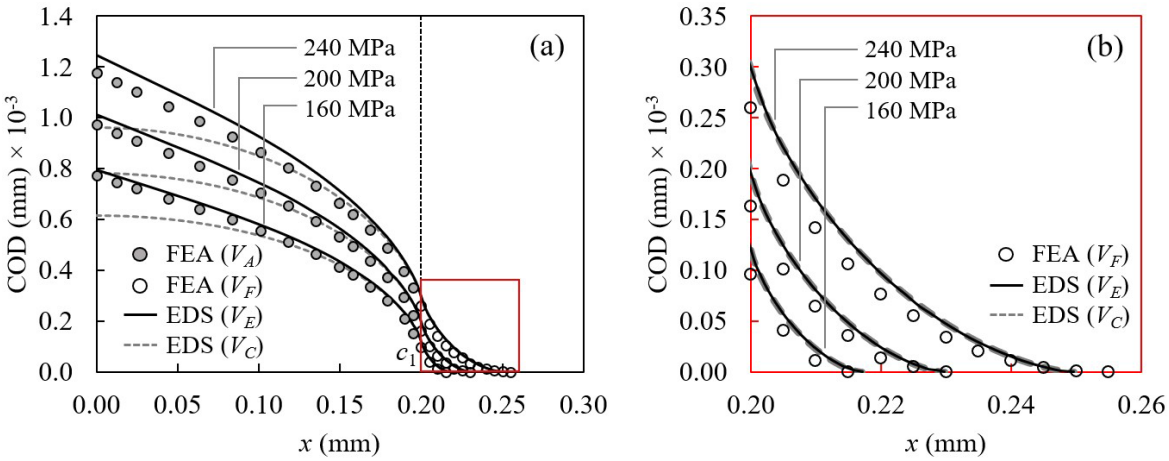

Fig. 5.19 Comparison of CODs along the depth direction obtained from the EDS method and FE analysis: **(a)** full profile; **(b)** magnified view ahead of the crack tip ($c_1/c_2 = 0.2$)

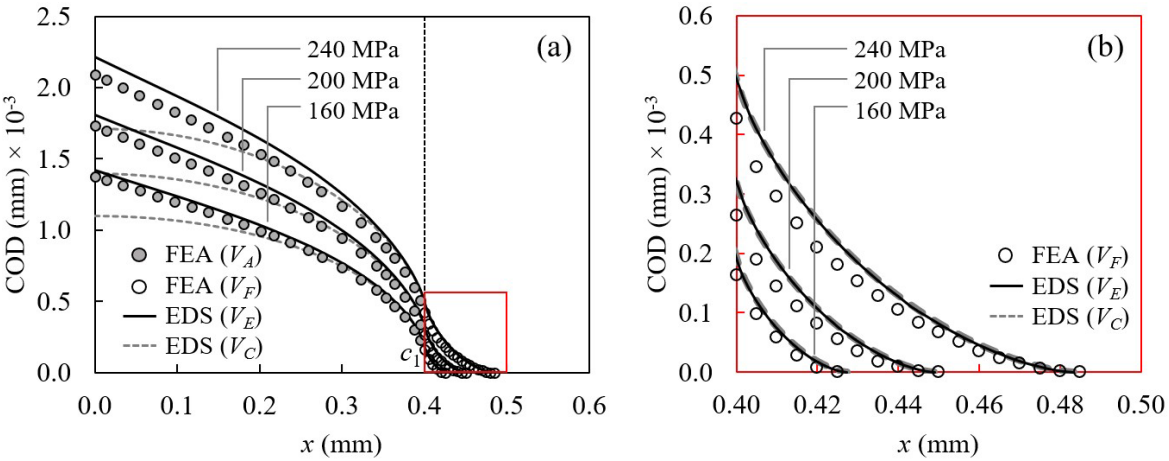

Fig. 5.20 Comparison of CODs along the depth direction obtained from the EDS method and FE analysis: **(a)** full profile; **(b)** magnified view ahead of the crack tip ($c_1/c_2 = 0.4$)

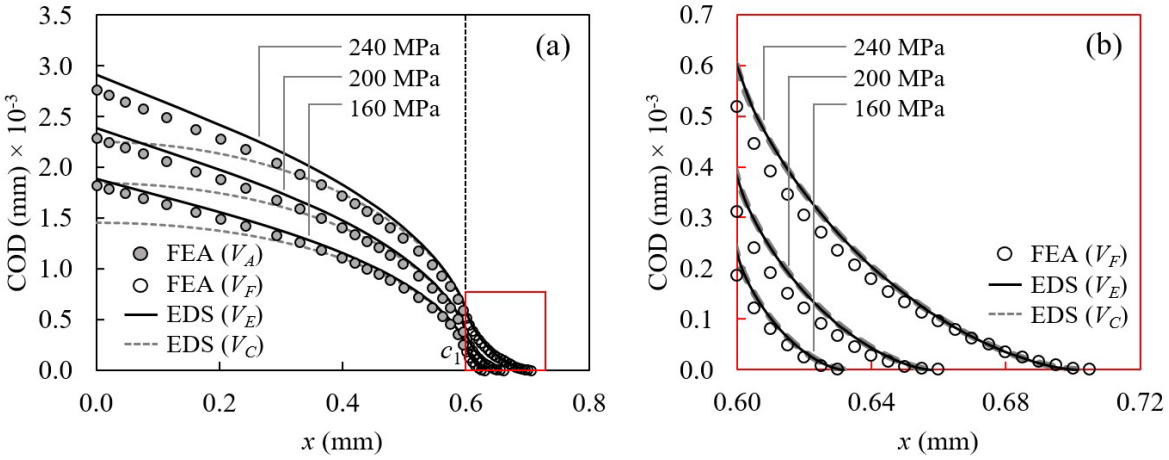

Fig. 5.21 Comparison of CODs along the depth direction obtained from the EDS method and FE analysis: **(a)** full profile; **(b)** magnified view ahead of the crack tip ($c_1/c_2 = 0.6$)

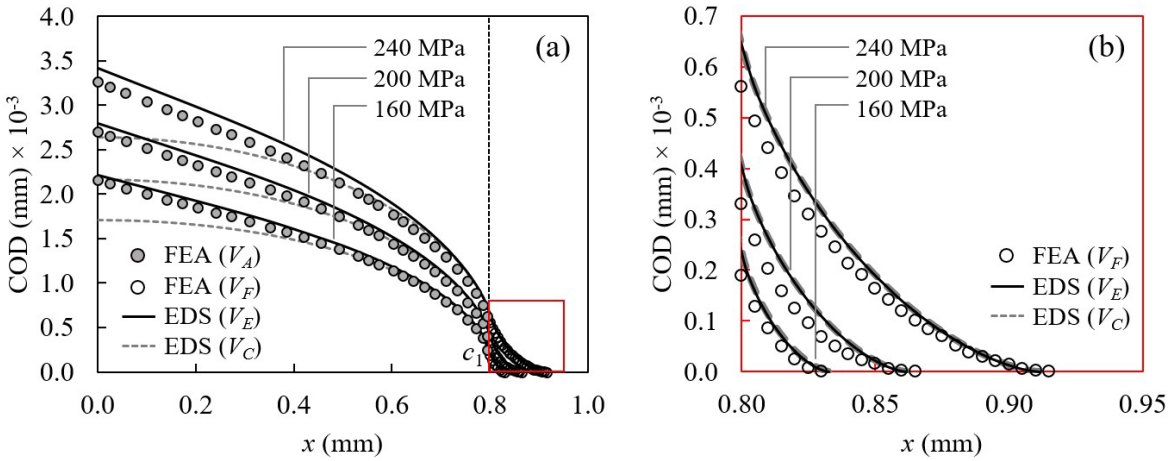

Fig. 5.22 Comparison of CODs along the depth direction obtained from the EDS method and FE analysis: **(a)** full profile; **(b)** magnified view ahead of the crack tip ($c_1/c_2 = 0.8$)

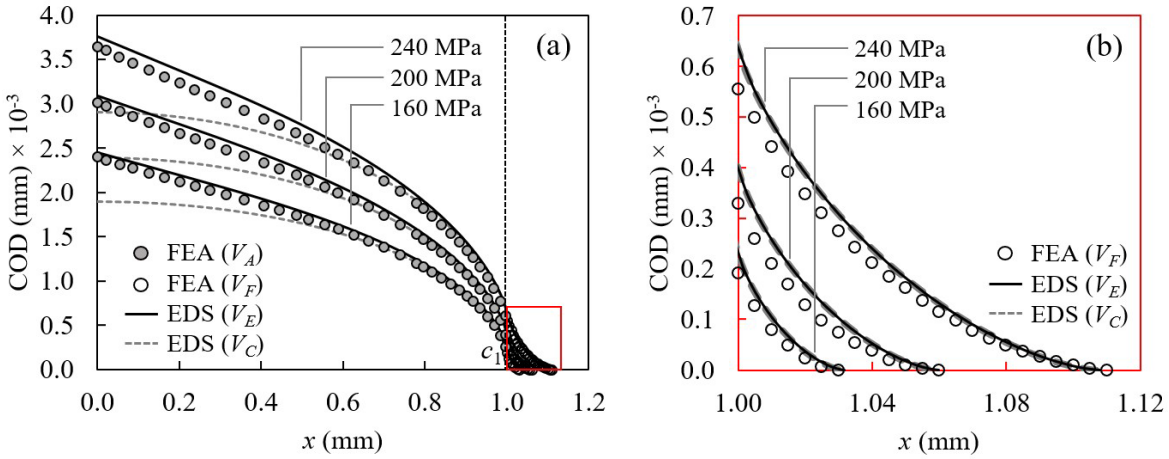

Fig. 5.23 Comparison of CODs along the depth direction obtained from the EDS method and FE analysis: **(a)** full profile; **(b)** magnified view ahead of the crack tip ($c_1/c_2 = 1.0$)

Table 5.1 presents the comparison between the key EPFM parameters (r_p and CTOD) at the deepest point, obtained using the EDS method with the center-through crack weight function and those derived from detailed FE analysis. The results show excellent agreement across all crack geometries and loading conditions, with differences consistently within an acceptable engineering tolerance. This level of accuracy demonstrates the robustness of the EDS method for evaluating critical fracture parameters at the deepest point of 3D surface cracks, even when using simplified 2D substitute crack models.

Moreover, the effectiveness of the current EDS framework underscores the validity of the cohesive zone assumptions and the prescribed *a*–*K* relationships developed in **Section 5.4**. These relationships provide a direct and consistent link between the applied loading and the resulting crack front conditions, which is essential for accurate near-tip fracture

characterization. The demonstrated capability of the EDS method to capture essential EPFM parameters with reduced computational effort suggests strong potential for its integration into practical engineering workflows. In particular, the use of a center-through crack allows for analytical simplification through closed-form solutions, making the approach especially suitable for FCP analysis under repeated cycles.

Table 5.1 Comparison of r_p and CTOD at the deepest point of target 3D surface cracks obtained from the EDS method and FE analysis

c_1/c_2	σ^P (MPa)	λ	r_p (mm) × 10^{-3}		CTOD (mm) × 10^{-3}	
			EDS	FEA	EDS	FEA
0.2	160	1.043	17.146	15.0	0.121	0.095
	200	1.036	29.785	30.0	0.197	0.163
	240	1.030	49.574	55.0	0.299	0.259
0.4	160	1.142	27.353	25.0	0.194	0.163
	200	1.125	48.957	50.0	0.321	0.264
	240	1.108	83.374	85.0	0.495	0.427
0.6	160	1.277	31.535	30.0	0.227	0.186
	200	1.246	57.814	60.0	0.381	0.312
	240	1.215	100.902	105.0	0.597	0.518
0.8	160	1.422	32.734	30.0	0.237	0.190
	200	1.375	61.621	65.0	0.404	0.330
	240	1.327	111.260	115.0	0.645	0.560
1.0	160	1.586	31.661	30.0	0.233	0.191
	200	1.526	59.775	60.0	0.398	0.329
	240	1.466	107.906	110.0	0.637	0.555

5.6 EDS Analysis of Surface Cracks at the Corner Points

While the previous section demonstrated the effectiveness of the EDS method at the deepest point of surface cracks, additional challenges arise at the corner point, where the crack front intersects the free surface. Unlike the deepest point, the corner point is typically characterized by a highly complex stress state, which complicates the accurate determination of SIF and other EPFM parameters. The geometry of the crack front at this

location, combined with the rapid transition from the interior of the material to the surface, results in a stress distribution that is difficult to model and compute reliably. Additionally, the interaction between the crack tip and the free surface can introduce localized effects, further complicating the analysis.

To address these complexities, the EDS method is extended to the corner point using the same cohesive zone assumptions and the prescribed *a–K* relationships developed in earlier sections. To ensure computational efficiency while maintaining sufficient accuracy in the evaluation of key EPFM parameters, the center-through crack is employed as the substitute model. This choice allows for the use of closed-form weight functions, simplifying the analysis of elastic-plastic crack opening behavior at this location [98].

The analysis in this section focuses on crack configurations with aspect ratios approaching 1.0, where crack growth is often more likely to initiate from the corner points. Specifically, surface cracks with c_1/c_2 = 0.6, 0.8, and 1.0 are examined using the EDS method. Since the corner point lies on the free surface and is predominantly subjected to a plane stress condition, λ is assumed to be 1.0 through the analysis.

5.6.1 EDS and Reproduced a–K Relationships for the Corner Points

As in the analysis at the deepest point, spline partition points for the corner point evaluation are set at wider intervals than the calculation points used for SIF determination. Specifically, the partition points are spaced at intervals of 0.2 mm. Given that c_2 = 1.0 mm for the analyzed cracks, this results in an interval number of 5 at c_2.

Figs. 5.24 – **5.26** show comparisons of CFTs (t^P and t^Y), and EDSs (f^P and f^Y), along the width direction of surface cracks with aspect ratios c_1/c_2 = 0.6, 0.8, and 1.0, under σ^P = 200 MPa. It is observed that both f^P and f^Y exhibit smooth and continuous behaviors when the aspect ratio is 1.0. However, for lower aspect ratios of 0.6 and 0.8, only f^P maintains a reasonable and physically consistent trend, while f^Y deviates significantly from t^Y.

This discrepancy arises from the nature of the local crack tip conditions at the corner point. In particular, it reflects the shift in the SIF-dominant region and the intrinsic characteristics of the cohesive stress *a–K* relationships. As discussed in the **Appendix C**, cohesive stress SIF at the corner point does not differ significantly from that generated by external stress when the crack has a low aspect ratio. Consequently, the cohesive response derived from yield-based loading does not develop in the same manner as it does at the

deepest point, resulting in a less accurate reproduction of f^Y at the corner. In contrast, f^P, obtained from traction applied over the entire crack face, remains more representative because it captures the broader stress distribution acting along the crack front.

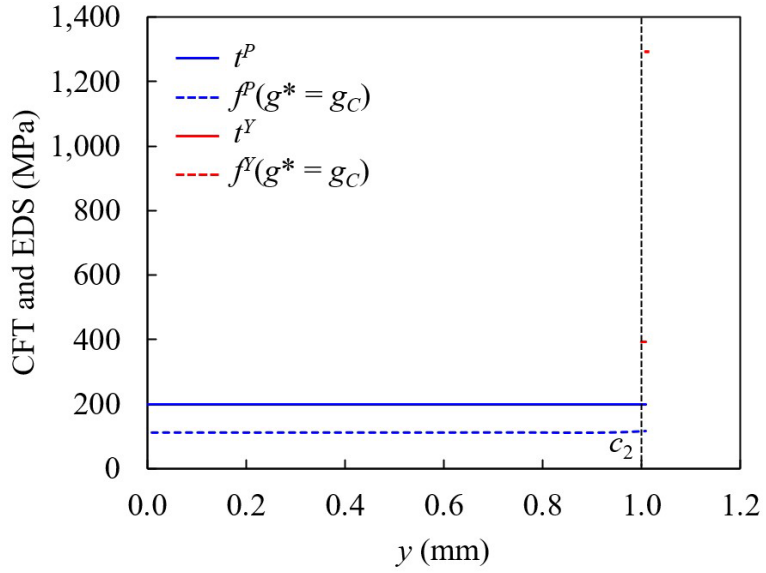

Fig. 5.24 Comparison of applied CFTs and calculated EDSs along the width direction of a 3D surface crack in a semi-infinite plate under uniform tensile loading ($c_1/c_2 = 0.6$, $\sigma^P = 200$ MPa)

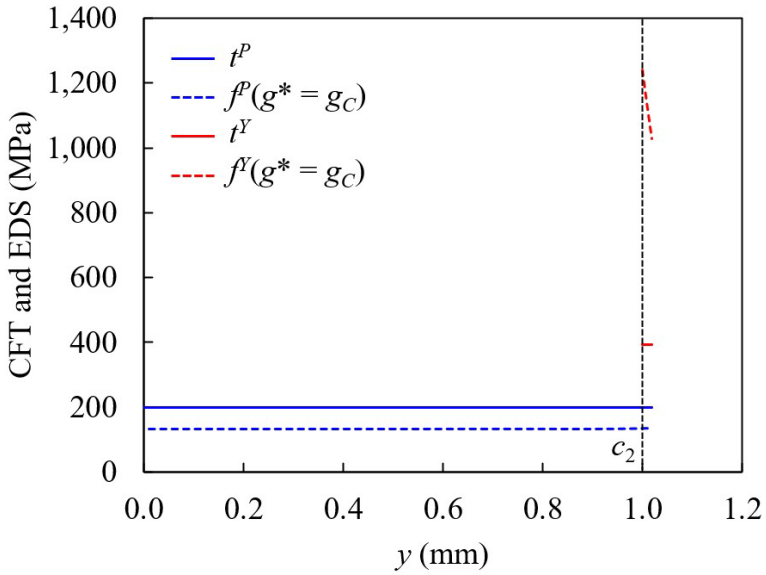

Fig. 5.25 Comparison of applied CFTs and calculated EDSs along the width direction of a 3D surface crack in a semi-infinite plate under uniform tensile loading ($c_1/c_2 = 0.8$, $\sigma^P = 200$ MPa)

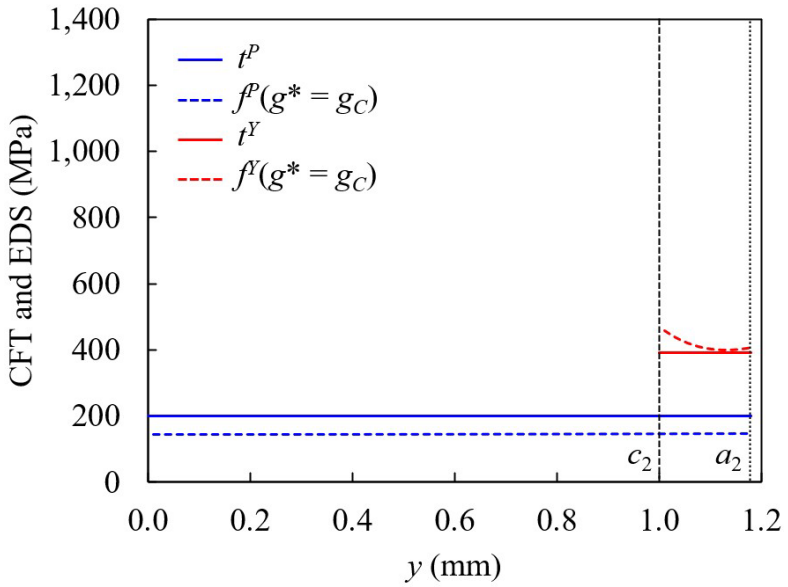

Fig. 5.26 Comparison of applied CFTs and calculated EDSs along the width direction of a 3D surface crack in a semi-infinite plate under uniform tensile loading ($c_1/c_2 = 1.0$, $\sigma^P = 200$ MPa)

Figs. 5.27 – 5.29 illustrate the prescribed *a*–*K* relationships of the analysis crack models at the corner point, alongside those reproduced from the EDSs using the weight function of the center-through crack (g_C). Consistent with the trends observed in the EDS results, the reproduced *a*–*K* relationships show good agreement with the prescribed values only for the crack with an aspect ratio $c_1/c_2 = 1.0$. In this case, the SIFs for both external and cohesive stresses are accurately captured across the entire range of crack extension.

However, for lower aspect ratios ($c_1/c_2 = 0.6$ and 0.8), although the external stress SIFs remain in good agreement with the prescribed *a*–*K* curves, the cohesive stress SIFs exhibit noticeable deviations. This discrepancy reinforces the earlier observation that cohesive zone behavior is strongly influenced by local fracture mechanics conditions at the corner point. Specifically, when the corner is not the SIF-dominant region, the applied cohesive stresses fail to develop the same crack-driving effect due to the reduced constraint and altered stress state near the free surface. As a result, the cohesive SIF response becomes less representative, leading to discrepancies in the reproduced.

It is important to emphasize that this deviation is not due to limitations of the substitute model or the chosen weight function, but rather to the physical nature of crack tip interactions in low-constraint regions.

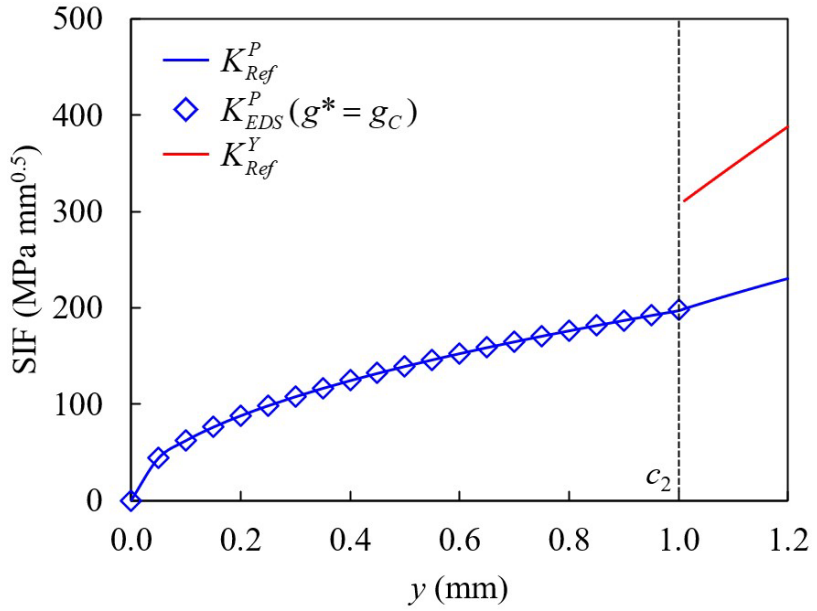

Fig. 5.27 Comparison of reference *a*–*K* relationships along the width direction of a 3D surface crack with reproduced *a*–*K* relationships obtained using EDSs applied to the substituted 2D center-through crack model (c_1/c_2 = 0.6, σ^P = 200 MPa)

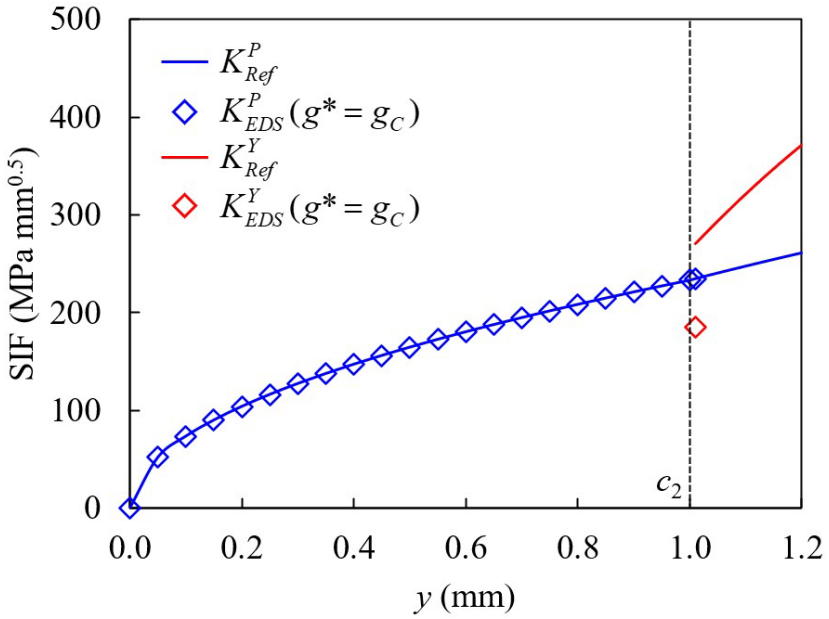

Fig. 5.28 Comparison of reference *a*–*K* relationships along the width direction of a 3D surface crack with reproduced *a*–*K* relationships obtained using EDSs applied to the substituted 2D center-through crack model (c_1/c_2 = 0.8, σ^P = 200 MPa)

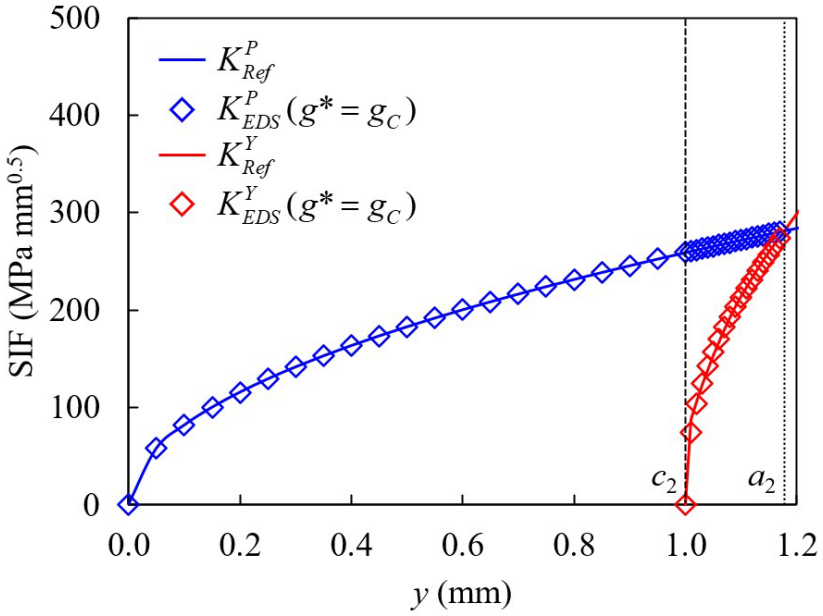

Fig. 5.29 Comparison of reference a–K relationships along the width direction of a 3D surface crack with reproduced a–K relationships obtained using EDSs applied to the substituted 2D center-through crack model (c_1/c_2 = 1.0, σ^P = 200 MPa)

5.6.2 Comparison of EPFM Parameters for the Corner Points

EDS analysis of surface cracks with c_1/c_2 ratios of 0.6, 0.8, and 1.0 are performed under three loading conditions (σ^P = 160, 200, and 240 MPa), consistent with the cases examined for the deepest point. The results were then compared with reference FE solutions along the width direction to evaluate the performance of the EDS method at the corner points.

Figs. 5.30 – **5.32** present a comparison between the elastic-plastic CODs obtained using the EDS method against those derived from FE analyses. For each loading case, results for all three aspect ratios are shown together to facilitate a comprehensive comparison.

The results indicate that for c_1/c_2 ratios of 0.6 and 0.8, the COD profiles computed using the EDS method agree well with the FE results in the region $0 \le y < c_2$, i.e., within the physically meaningful crack length. However, beyond the physical crack tip, significant discrepancies appear, particularly in the computed plastic zone size r_p and CTOD. These discrepancies are primarily attributed to the limitations of the EDS method in accurately reproducing the SIF, K^Y, associated with yield-based cohesive loading at the corner point, as discussed in the preceding sections.

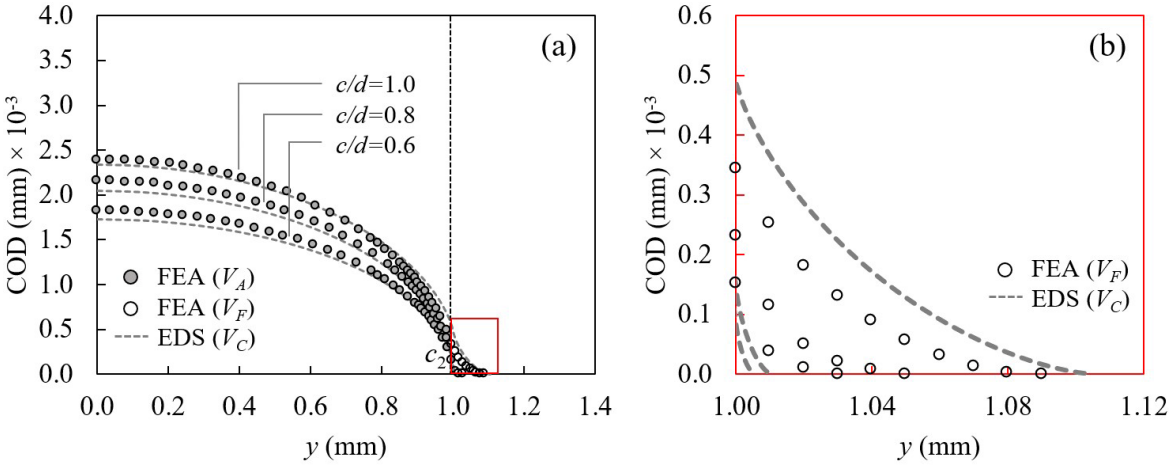

Fig. 5.30 Comparison of CODs along the width direction obtained from the EDS method and FE analysis: **(a)** full profile; **(b)** magnified view ahead of the crack tip (σ^P=160 MPa)

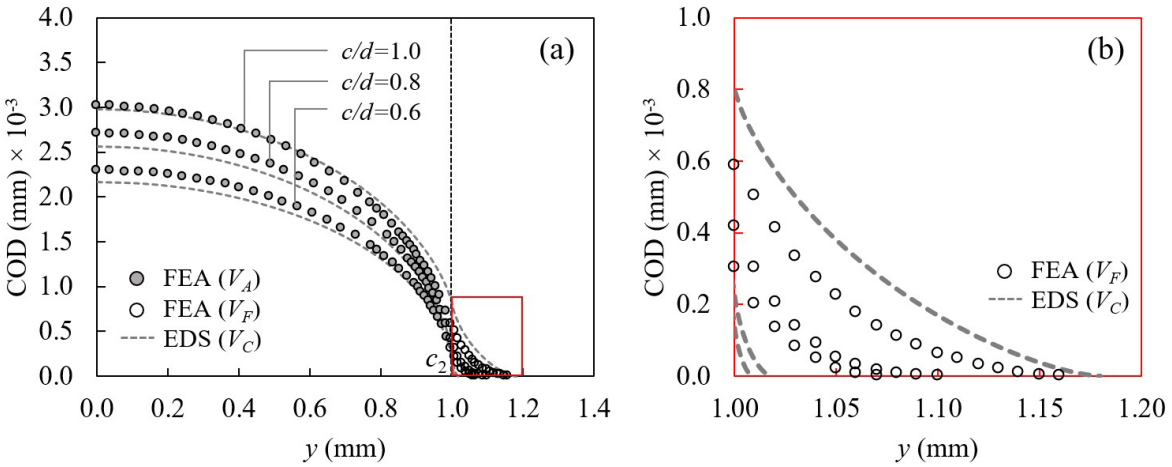

Fig. 5.31 Comparison of CODs along the width direction obtained from the EDS method and FE analysis: **(a)** full profile; **(b)** magnified view ahead of the crack tip (σ^P=200 MPa)

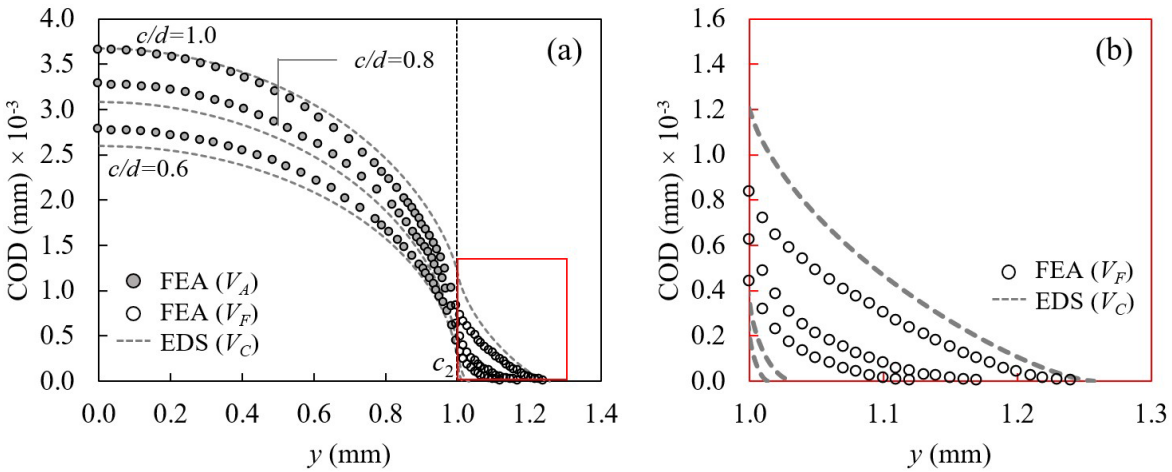

Fig. 5.32 Comparison of CODs along the width direction obtained from the EDS method and FE analysis: **(a)** full profile; **(b)** magnified view ahead of the crack tip (σ^P=240 MPa)

In contrast, for the $c_1/c_2 = 1.0$, where the corner point is the dominant location in terms of SIF, the EDS method successfully reproduces both K^P and K^Y. As a result, the computed COD profiles, as well as the corresponding r_p and CTOD, show favorable agreement with the FE results across all loading levels. A summary of r_p and CTOD values at the corner point, obtained using the EDS method with the center-through crack weight function and those derived from detailed FE analyses is provided in **Table 5.2**.

Table 5.2 Comparison of r_p and CTOD at the corner point of target 3D surface cracks obtained from the EDS method and FE analysis

c_1/c_2	σ^P (MPa)	r_p (mm) × 10^{-3}		CTOD (mm) × 10^{-3}	
		EDS	FEA	EDS	FEA
0.6	160	5.594	30.0	0.105	0.152
	200	8.812	70.0	0.157	0.303
	240	13.689	120.0	0.204	0.437
0.8	160	10.350	50.0	0.142	0.232
	200	18.090	100.0	0.227	0.418
	240	31.880	170.0	0.340	0.618
1.0	160	105.070	90.0	0.487	0.344
	200	179.830	160.0	0.798	0.588
	240	257.067	240.0	1.193	0.832

These findings underscore the importance of geometric and boundary conditions in cohesive stress-based evaluations using the EDS method. Since the EDS method is formulated to reproduce the SIF of a 3D crack using a 2D crack, its accuracy is sensitive to the local dominance of crack-driving forces. When the corner point is not the SIF-dominant location—as in the cases with $c_1/c_2 = 0.6$ and 0.8—the method becomes less reliable, despite the FE results in **Section 5.3** indicating a slightly longer plastic zone at the corner for $c_1/c_2 = 0.8$, possibly due to mesh-related effects.

Understanding this behavior is essential for applying the EDS method to realistic surface cracks, where local conditions may vary significantly along the crack front.

5.7 Summary

This chapter presented an extension of the EDS method to the analysis of non-axisymmetric 3D surface cracks. The investigation focused on evaluating the applicability and limitations of the EDS approach in predicting key EPFM parameters (r_p and CTOD) at two characteristic locations along the crack front: the deepest point and the corner point. To achieve this, surface cracks with varying aspect ratios were analyzed under specific loading conditions, using substituted 2D center-through and edge crack models.

Following the configuration of the target crack geometries, detailed elastic-plastic FE analyses were performed to generate reference solutions. These analyses provided COD profiles, plastic zone morphologies, and plastic constraint factors necessary for verifying the EDS method and the simplified cohesive zone assumptions.

Prescribed *a–K* relationships for external and cohesive stress are developed using LEFM analysis, combining the interaction integral method with the CFT-integral formulation. These were implemented in the public-domain FE code WARP3D. Due to the non-uniformity of the plastic zone along the crack front, simplified, idealized model of the plastic zone was adopted to enable consistent construction of the prescribed *a–K* relationships needed for the EDS analysis. To facilitate accurate evaluation of SIFs for cohesive stress, WARP3D was enhanced to compute equivalent nodal forces arising from partially applied traction stresses via high-precision numerical surface integration using ultra-high-order Gauss–Legendre quadrature.

For the deepest point, the EDS method successfully reproduced the SIFs for both the externally applied and cohesive stresses (K^P and K^Y), demonstrating favorable agreement with the FE solutions across all aspect ratios. The resulting r_p and CTOD closely matched the reference data, confirming the robustness of the method in this region. Furthermore, it was shown that both center-through and edge crack can serve effectively as substitute models in the EDS analysis. Notably, using a center-through crack is advantageous due to the availability of closed-form solutions, which simplify calculations while maintaining sufficient accuracy in predicting r_p and CTOD.

In contrast, the application of the EDS method to the corner point revealed a strong sensitivity to the local geometric and constraint conditions. For $c_1/c_2 = 1.0$, where the corner point is a SIF–dominant location, the EDS method accurately reproduced K^P and K^Y,

resulting in good agreement with the FE-derived EPFM parameters. However, for lower aspect ratios (c_1/c_2 = 0.6 and 0.8), the corner point exhibited reduced SIF dominance. In these cases, the EDS method showed limitations in replicating cohesive stress behavior, leading to deviations in the calculated r_p and CTOD values—particularly beyond the physical crack front. These discrepancies are attributed to the method's inherent reliance on SIF reproduction, which becomes less reliable in low-constraint, geometry-sensitive regions.

The findings in this chapter highlight the importance of considering local crack-front characteristics when applying the EDS method to surface cracks. While the method provides a practical and analytically tractable tool for evaluating elastic-plastic behavior, its applicability is contingent on the crack-driving force being sufficiently dominated by the SIF. This insight is critical for extending the EDS method to realistic engineering applications involving complex crack geometries and constraint conditions.

CHAPTER 6

CONCLUSION

This dissertation has presented a comprehensive framework for EPFM analysis of 3D cracks, grounded in EDS method. Motivated by the need for computationally efficient and physically interpretable approaches, the proposed method offers a practical tool for evaluating fracture parameters in support of SYM-based FCP analysis programs.

The EDS-based fracture mechanics analysis system was constructed on the foundation of the original EDS theory, adopting the FLM approach to ensure high accuracy and reliability. Two 2D substitute crack models—a center-through crack in an infinite plate and an edge crack in a semi-infinite plate—were introduced to represent the crack tip opening behavior of 3D cracks. By matching the crack length–SIF (a–K) relationships between the original 3D crack and the substitute models through generalized matrix inversion, the system enabled direct evaluation of elastic-plastic CODs and associated EPFM parameters using the simplified solutions of the substitute cracks.

The accuracy of the proposed framework was first validated using a 3D penny-shaped crack in an infinite plate subjected to axisymmetric loading. This geometry, which offers an analytical weight function, allowed for rigorous verification. Using a 2D center-through crack as the substitute model, the prescribed a–K relationships were accurately reproduced through the FLM-based EDS approach. The resulting elastic-plastic COD profiles showed excellent agreement with analytical solutions derived from Sneddon's closed-form expressions, demonstrating both the reliability and computational efficiency of the proposed framework.

To demonstrate broader applicability, the system was extended to non-axisymmetric 3D surface cracks, which are more commonly encountered in engineering structures. The method was applied to a range of surface cracks with varying aspect ratios and loadings, with particular attention given to two key EPFM parameters: the plastic zone size, r_p, and CTOD. FE analyses provided detailed reference data, including COD profiles and plastic zone morphologies, enabling validation of the EDS-based results at both the deepest and corner points along the crack front. To address the complex distribution of plastic zones, idealized plastic zone model was adopted to construct consistent a–K relationships, and

high-precision numerical integration was incorporated into the FE code WARP3D for an accurate evaluation of prescribed SIFs.

At the deepest point along the crack front, the EDS method demonstrated strong performance by accurately reproducing both externally applied and cohesive stress SIF (K^P and K^Y) across all aspect ratios. The resulting values of r_p and CTOD closely matched the FE reference data, validating the robustness of the approach in this region. Both substitute crack models proved effective, with the center-through crack model offering the added advantage of closed-form solutions that simplify calculation without compromising accuracy.

In contrast, the application of the EDS method to the corner point revealed greater sensitivity to local geometric and constraint conditions. For cracks where the corner region remained dominated by SIF, the EDS method maintained good accuracy in reproducing K^P and K^Y and predicting r_p and CTOD. However, for lower aspect ratios, where the corner point experienced reduced SIF dominance, the method showed limitations in capturing the cohesive stress behavior. This resulted in noticeable discrepancies beyond the physical crack front, especially in the values of r_p and CTOD. These deviations are attributed to the method's reliance on reproducing the SIF of a 3D crack using a 2D substitute crack, which becomes less reliable under low-constraint and geometry-sensitive conditions.

Overall, this study demonstrates that the EDS-based framework provides a practical and analytically tractable approach for evaluating elastic-plastic fracture behavior of 3D cracks, particularly effective at crack propagation initiation points where the SIF is dominant. The method offers a significant reduction in computational cost while maintaining accuracy in predicting key EPFM parameters.

As a future direction, the integration of the developed EDS-based system into FCP analysis programs is anticipated. Such integration will significantly enhance the efficiency and applicability of fatigue crack growth predictions in large-scale structural components with complex geometries, contributing to safer and more reliable engineering designs.

APPENDICES

A. EDS-Based CZM Considering Residual Stress

In fracture mechanics analysis, accounting for residual stress is essential to ensure safe and reliable structural design, particularly in welded components where tensile residual stress can significantly influence crack behavior. This appendix outlines the procedure for incorporating residual stress into the EDS-based CZM.

Let t^R denote the CFT representing the effects of welding-induced residual stress σ^R in the 3D cracked body. The reference SIF, K^R_{Ref}, induced by t^R can be determined by efficient and reliable numerical tools such as FRANC3D [99].

Let $f^R(x)$ represent the residual stress EDS applied to the substituted 2D models. Like the external stress EDS $f^P(x)$, this distribution is expressed using a cubic spline function over $i_{\max}$ segments, with nodal coordinates $x_0 = 0, \cdots, x_{i_{\max}}$. Each segment $f_i^R(x)$ is defined by spline coefficients $\{\alpha_i^R, \beta_i^R, \gamma_i^R, \delta_i^R\}$. When $f_i^R(x)$ is applied over the region ($0 \le x \le a$) of the substituted 2D crack, the SIF at the fictitious crack tip, K^R_{EDS}, is given by:

$$\begin{aligned} K^R_{EDS} &= \sum_{i=1}^{0\le x_i\le a} \int_{\xi=x_{i-1}}^{\min(a,x_i)} f_i^R(\xi) g^*(\xi,a)\, d\xi \\ &= \sum_{i=1}^{x_i\le a} \left\{ G^{(3)}_{K,i}(a)\alpha_i^R + G^{(2)}_{K,i}(a)\beta_i^R + G^{(1)}_{K,i}(a)\gamma_i^R + G^{(0)}_{K,i}(a)\delta_i^R \right\} \end{aligned} \tag{A.1}$$

At the fictitious crack tip, where the stress singularity vanishes, the combined SIFs induced by f^P and f^R must cancel out that induced by cohesive stress EDS f^Y, leading to:

$$K^P_{EDS} + K^R_{EDS} - K^Y_{EDS} = 0 \tag{A.2}$$

The fictitious crack length a is determined iteratively to satisfy **Eq. (A.2)**.

CODs induced by $f_i^R(x)$, denoted as $V^R(x)$, can be calculated using:

$$\begin{aligned} V^R(x) &= \frac{2}{E'} \sum_{i=1}^{i_{\max}} \int_{\xi=x_{i-1}}^{\min(a,x_i)} f_i^R(\xi)\, V_0(x;\xi,a)\, d\xi \\ &= \frac{2}{E'} \sum_{i=1}^{i_{\max}} \left[\alpha_i^R G^{(3)}_{V,i}(x,a) + \beta_i^R G^{(2)}_{V,i}(x,a) + \gamma_i^R G^{(1)}_{V,i}(x,a) + \delta_i^R G^{(0)}_{V,i}(x,a) \right] \end{aligned} \tag{A.3}$$

Finally, the total elastic-plastic COD that accounts for residual stress is obtained as:

$$V(x) = V^P(x) + V^R(x) - V^Y(x) \tag{A.4}$$

B. Sneddon's Solutions for Elastic-Plastic COD of a 3D Penny-Shaped Crack under Axisymmetric Loading

The coordinate system and configuration of a 3D penny-shaped are shown in **Fig. 4.1**. When an annular loading $t^P(x)$ acts on the crack of radius a, the normal displacement u_0 at the crack surface is given by the following equation [78].

$$u_0(x) = \frac{4(1-\nu^2)a}{\pi E}\int_\rho^1 \frac{\mu d\mu}{\sqrt{\mu^2-\rho^2}}\int_0^1 \frac{\xi t^P(\xi\mu a)d\xi}{\sqrt{1-\xi^2}}, \quad \rho = \frac{x}{a} \text{ and } \xi = \frac{\rho}{\mu} \tag{B.1}$$

where ν is Poisson's ratio, E is Young's Modulus and t^P is a function of $x = \xi\mu a$.

When a uniform axisymmetric traction stress $t^P = \sigma^P$ acts on the entire crack face ($0 \le x \le a$), the displacement u^P, can be obtained by solving the integral in **Eq. (B.1)** [100]:

$$u^P(x) = \frac{8(1-\nu^2)\sigma^P a}{\pi E}\sqrt{1-\rho^2} \tag{B.2}$$

Similarly, when the traction stress $t^Y = \lambda\sigma^Y$ is applied over the region $c \le x \le a$, the corresponding displacement u^Y, is given by:

$$u^Y(x) = \frac{8(1-\nu^2)\lambda\sigma^Y a}{\pi E}\begin{cases}\sqrt{\dfrac{1-m^2}{1-\rho^2}} - mE\left(\varphi_1, \dfrac{\rho}{m}\right), & 0 \le x \le c \\ \sqrt{\dfrac{1-\rho^2}{1-m^2}} + \dfrac{\rho^2-m^2}{\rho}F\left(\varphi_2, \dfrac{m}{\rho}\right) - \rho E\left(\varphi_2, \dfrac{m}{\rho}\right), & c \le x \le a\end{cases} \tag{B.3}$$

where $m = \dfrac{c}{a}$, $\varphi_1 = \arcsin\sqrt{\dfrac{1-m^2}{1-\rho^2}}$, $\varphi_2 = \arcsin\sqrt{\dfrac{1-\rho^2}{1-m^2}}$, λ is the plastic constraint factor, $F(\varphi,k)$ and $E(\varphi,k)$ are the elliptic integrals of first and second kind, respectively.

The elastic-plastic COD, denoted as $u(x)$, for the 3D penny-shaped crack can then be expressed as:

$$u(x) = u^P(x) - u^Y(x) \tag{B.4}$$

C. SIFs for External and Cohesive Stresses Calculated Using WARP3D

Figs. C.1 – C.5 present the SIFs K^P and K^Y for unit CFT, calculated using WARP3D and plotted along the crack front of the analyzed cracks. To provide a detailed characterization of the SIF distribution, the results are also tabulated at 0.05 mm increments of fictitious crack extension, up to 0.2 mm beyond the physical crack front.

The results show that at the corner points (0 and 180 deg), K^Y is not significantly different from K^P for cracks with low aspect ratios. As the aspect ratio c_1/c_2 increases, the difference between K^P and K^Y becomes more pronounced.

Notably, for $c_1/c_2 = 1.0$, K^P reaches its maximum at the corner point. For other aspect ratios—$c_1/c_2 = 0.2$, 0.4, 0.6 and 0.8—the deepest point (90 deg) exhibits higher K^P values than the corner, indicating that the dominant crack-driving location is the deepest point in these cases. In contrast, for $c_1/c_2 = 1.0$, the corner point becomes the most critical location for crack growth.

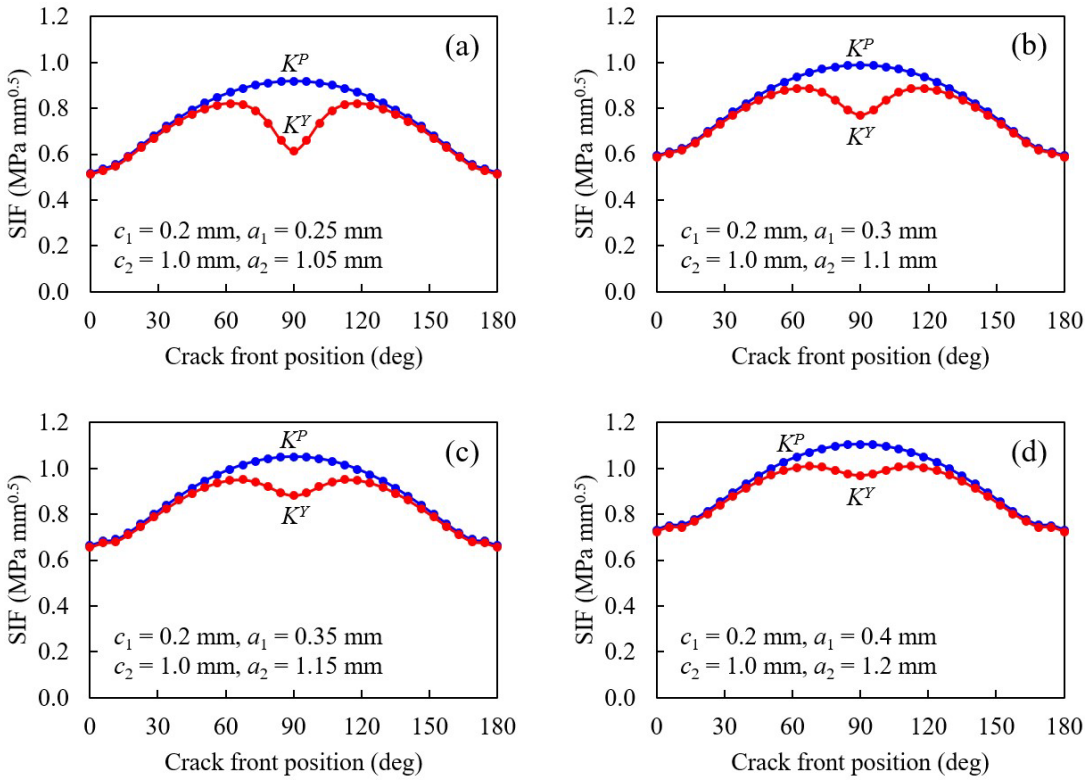

Fig. C.1 K^P and K^Y for unit CFT along the crack front of a surface crack with $c_1/c_2 = 0.2$: **(a)** 0.05 mm; **(b)** 0.1 mm; **(c)** 0.15 mm; **(d)** 0.2 mm extensions of the fictitious crack front

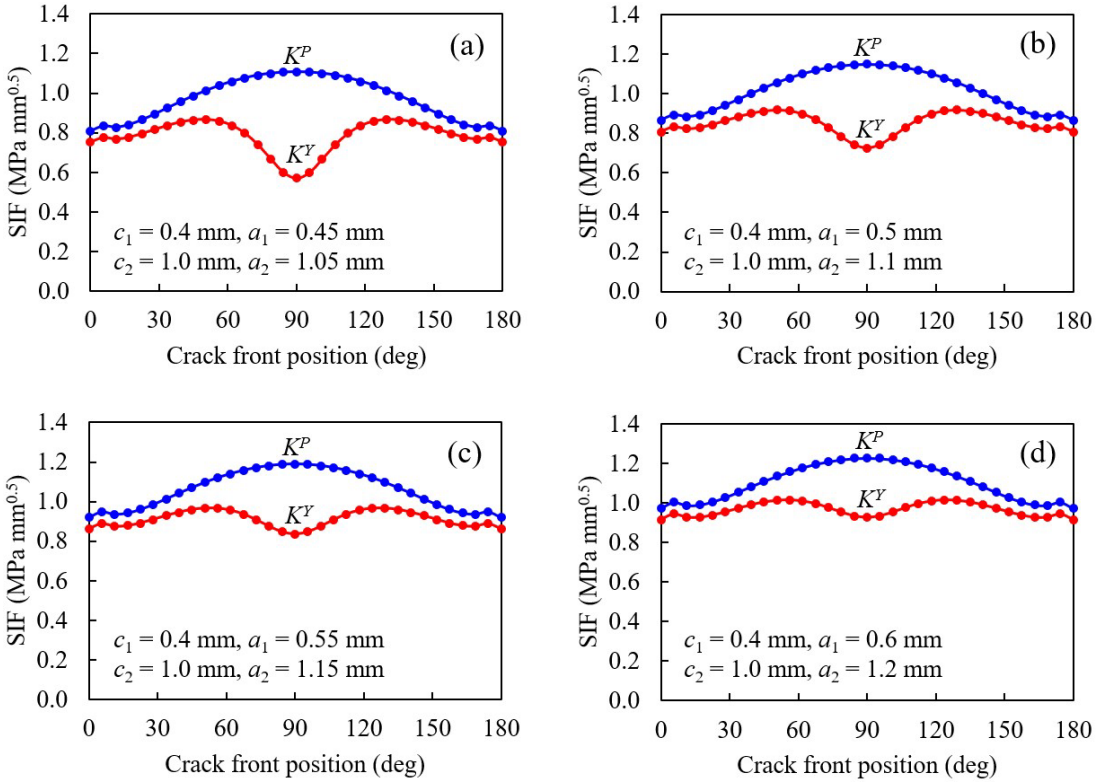

Fig. C.2 K^P and K^Y for unit CFT along the crack front of a surface crack with $c_1/c_2 = 0.4$: **(a)** 0.05 mm; **(b)** 0.1 mm; **(c)** 0.15 mm; **(d)** 0.2 mm extensions of the fictitious crack front

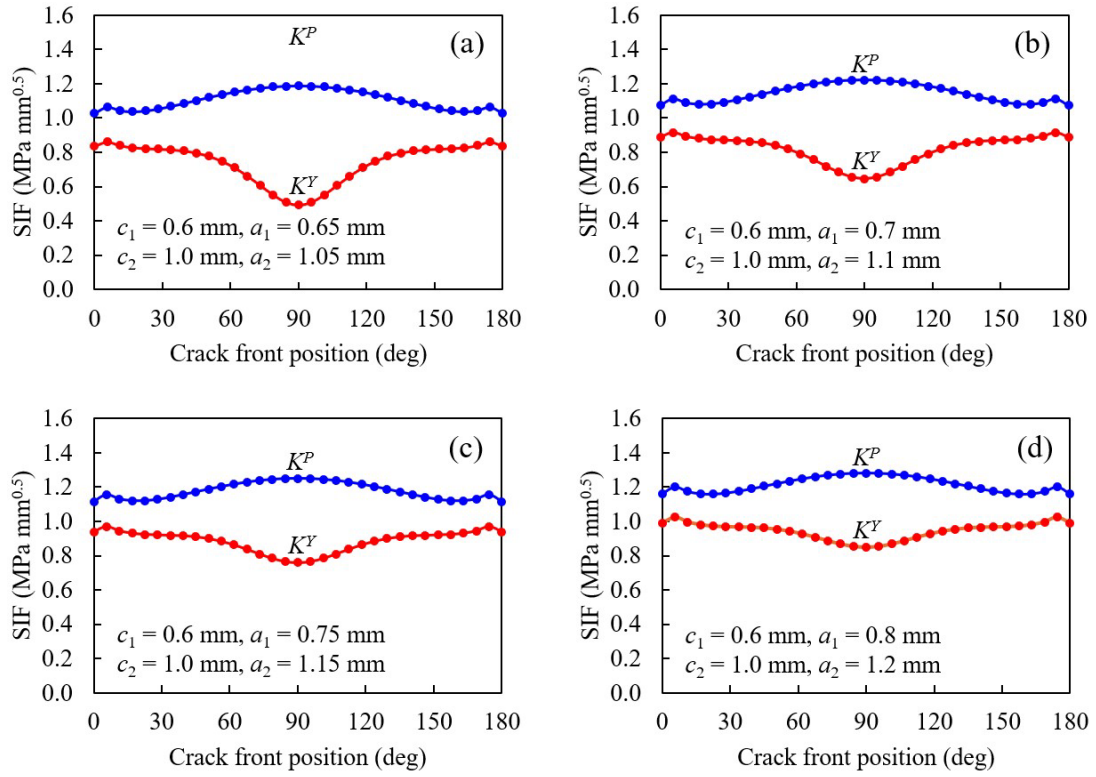

Fig. C.3 K^P and K^Y for unit CFT along the crack front of a surface crack with $c_1/c_2 = 0.6$: **(a)** 0.05 mm; **(b)** 0.1 mm; **(c)** 0.15 mm; **(d)** 0.2 mm extensions of the fictitious crack front

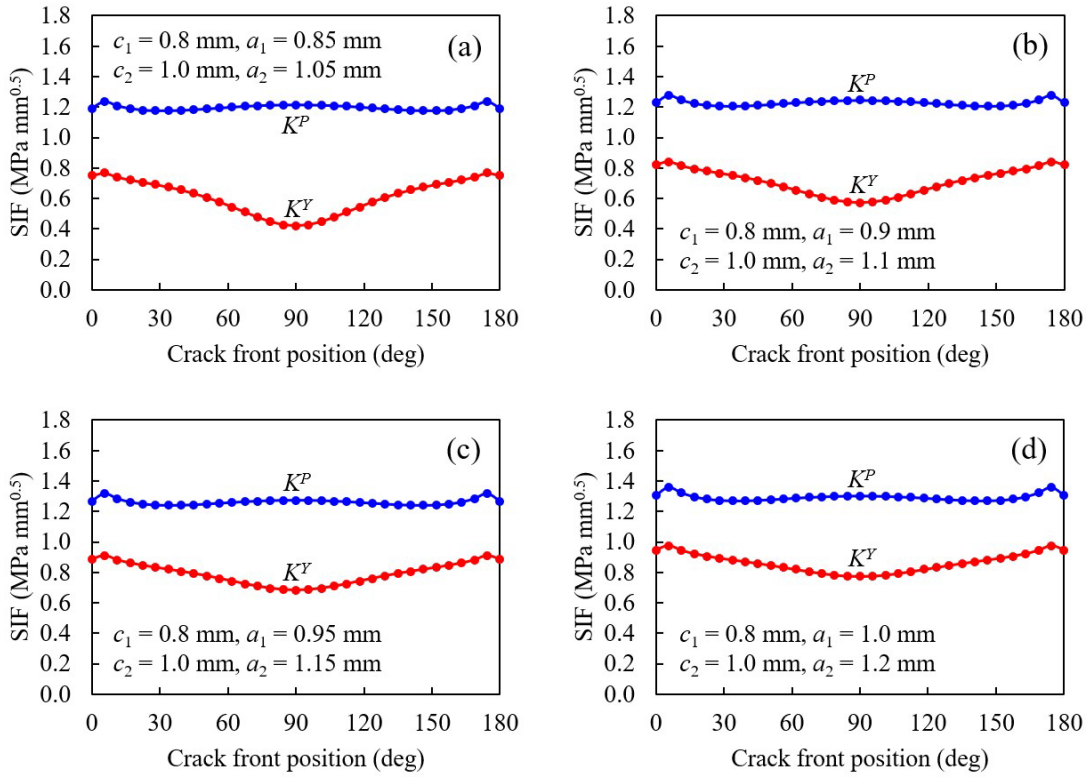

Fig. C.4 K^P and K^Y for unit CFT along the crack front of a surface crack with c_1/c_2 = 0.8: **(a)** 0.05 mm; **(b)** 0.1 mm; **(c)** 0.15 mm; **(d)** 0.2 mm extensions of the fictitious crack front

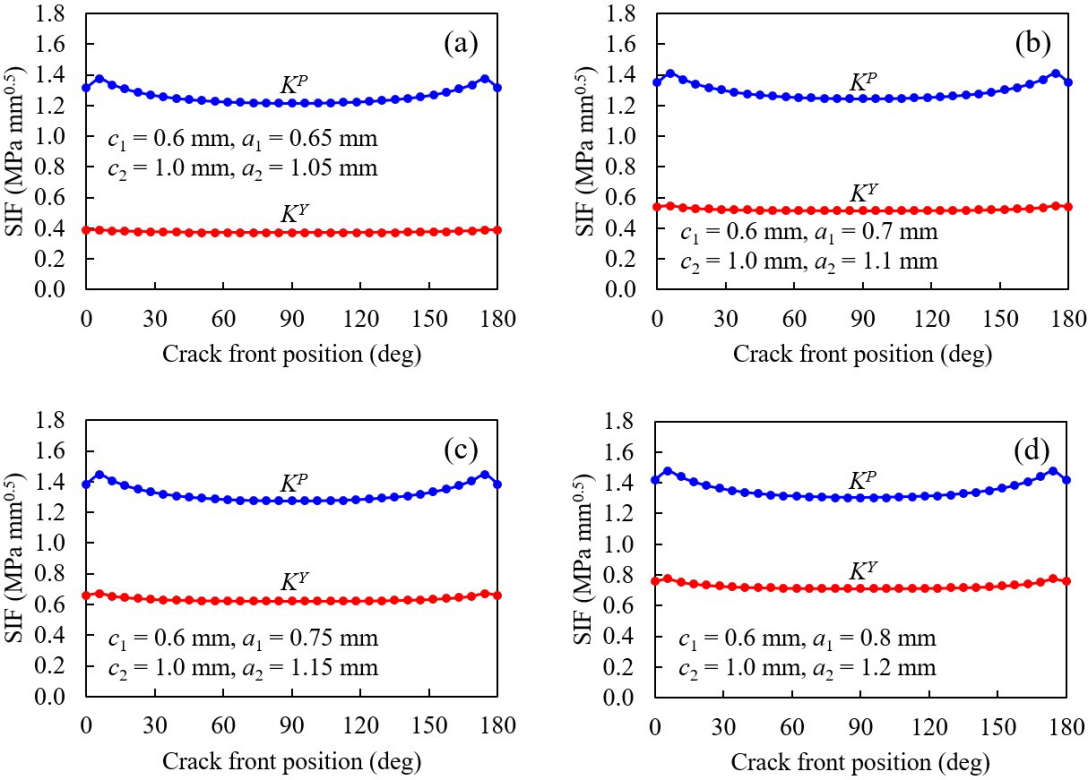

Fig. C.5 K^P and K^Y for unit CFT along the crack front of a surface crack with c_1/c_2 = 1.0: **(a)** 0.05 mm; **(b)** 0.1 mm; **(c)** 0.15 mm; **(d)** 0.2 mm extensions of the fictitious crack front

REFERENCES

[1] Williams ML, Ellinger GA. Investigation of structural failures of welded ships. Weld J 1953;32:498–528.

[2] Almar-Naess A, Haagensen PJ, Lian B, Moan T, Simonsen T. Investigation of the Alexander L. Kielland failure—metallurgical and fracture analysis. J Energy Resour Technol 1984;106:24–31. https://doi.org/10.1115/1.3231014.

[3] Anderson TL. Fracture mechanics. CRC Press; 2005. https://doi.org/10.1201/9781420058215.

[4] Inglis CE. Stresses in a plate due to the presence of cracks and sharp corners. Trans Inst Nav Archit 1913;55:219–41.

[5] Griffith AA. The phenomena of rupture and flow in solids. Philos Trans R Soc A 1921;221:163–98. https://doi.org/10.1098/rsta.1921.0006.

[6] Irwin GR. Fracture dynamics. Fracturing of Metals, Cleveland, OH: American Society for Metals; 1948, p. 147–66.

[7] Orowan E. Fracture and strength of solids. Rep Prog Phys 1949;12:309. https://doi.org/10.1088/0034-4885/12/1/309.

[8] Mott NF. Fracture of metals: Theoretical considerations. Engineering 1948;165:16–8.

[9] Irwin GR. Onset of fast crack propagation in high strength steel and aluminum alloys. Sagamore Res Conf Proc, vol. 2, 1956, p. 289–305.

[10] Westergaard HM. Bearing pressures and cracks: Bearing pressures through a slightly waved surface or through a nearly flat part of a cylinder, and related problems of cracks. J Appl Mech 1939;6:A49–53. https://doi.org/10.1115/1.4008919.

[11] Irwin GR. Analysis of stresses and strains near the end of a crack traversing a plate. J Appl Mech 1957;24:361–4. https://doi.org/10.1115/1.4011547.

[12] Williams ML. On the stress distribution at the base of a stationary crack. J Appl Mech 1957;24:109–14.

[13] Wells AA. The condition of fast fracture in aluminum alloys with particular reference to comet failures. Br Weld Res Assoc Rep, 1955.

[14] Winne DH, Wundt BM. Application of the Griffith-Irwin theory of crack propagation to the bursting behavior of disks, including analytical and experimental studies. J Fluids Eng 1958;80:1643–55. https://doi.org/10.1115/1.4012835.

[15] Paris PC, Gomez MP, Anderson WP. A rational analytic theory of fatigue. Trend Eng 1961;13:9–14.

[16] Irwin GR. Plastic zone near a crack and fracture toughness. Sagamore Res Conf Proc, Syracuse University Research Institute, Syracuse, NY: 1961, p. 63–78.

[17] Dugdale DS. Yielding of steel sheets containing slits. J Mech Phys Solids 1960;8:100–4. https://doi.org/10.1016/0022-5096(60)90013-2.

[18] Barenblatt GI. The mathematical theory of equilibrium cracks in brittle fracture, 1962, p. 55–129. https://doi.org/10.1016/S0065-2156(08)70121-2.

[19] Wells AA. Unstable crack propagation in metals: Cleavage and fast fracture. Proc Crack Propag Symp, Cranfield, UK: 1961.

[20] Rice JR. A path independent integral and the approximate analysis of strain concentration by notches and cracks. J Appl Mech 1968;35:379–86.

[21] Eshelby JD. The continuum theory of lattice defects, 1956, p. 79–144. https://doi.org/10.1016/S0081-1947(08)60132-0.

[22] Hutchinson JW. Singular behaviour at the end of a tensile crack in a hardening material. J Mech Phys Solids 1968;16:13–31. https://doi.org/10.1016/0022-5096(68)90014-8.

[23] Rice JR, Rosengren GF. Plane strain deformation near a crack tip in a power-law hardening material. J Mech Phys Solids 1968;16:1–12. https://doi.org/10.1016/0022-5096(68)90013-6.

[24] Begley JA, Landes JD. The J-integral as a fracture criterion. ASTM STP 514, Am Soc Test Mater, Philadelphia, PA: 1972, p. 1–20.

[25] ASTM E813-81: Standard test method for JIC, a measure of fracture toughness 1981.

[26] Shih CF, Hutchinson JW. Fully plastic solutions and large scale yielding estimates for plane stress crack problems. J Eng Mater Technol 1976;98:289–95. https://doi.org/10.1115/1.3443380.

[27] Kumar V, German MD, Shih CF. An engineering approach for elastic-plastic fracture analysis. Palo Alto, CA: 1981.

[28] Burdekin FM, Dawes MG. Practical use of linear elastic and yielding fracture mechanics with particular reference to pressure vessels. Proc Inst Mech Eng Conf, London: 1971, p. 28–37.

[29] Shih CF. Relationships between the J-integral and the crack opening displacement for stationary and extending cracks. J Mech Phys Solids 1981;29:305–26. https://doi.org/10.1016/0022-5096(81)90003-X.

[30] ASTM E1820-99a: Standard test method for measurement of fracture toughness 1999. https://doi.org/10.1520/E1820-99A.

[31] Belytschko T, Black T. Elastic crack growth in finite elements with minimal remeshing. Int J Numer Methods Eng 1999;45:601–20. https://doi.org/10.1002/(SICI)1097-0207(19990620)45:5<601::AID-NME598>3.0.CO;2-S.

[32] Dolbow J, Moës N, Belytschko T. An extended finite element method for modeling crack growth with frictional contact. Comput Methods Appl Mech Eng 2001;190:6825–46. https://doi.org/10.1016/S0045-7825(01)00260-2.

[33] Li H, Yang Z, Li B, Wu J. A phase-field regularized cohesive zone model for quasi-brittle materials with spatially varying fracture properties. Eng Fract Mech 2021;256:107977. https://doi.org/10.1016/j.engfracmech.2021.107977.

[34] Baktheer A, Martínez-Pañeda E, Aldakheel F. Phase field cohesive zone modeling for fatigue crack propagation in quasi-brittle materials. Comput Methods Appl Mech Eng 2024;422:116834. https://doi.org/10.1016/j.cma.2024.116834.

[35] Sorić J, Wriggers P, Allix O. Multiscale modeling of heterogeneous structures. vol. 86. Cham: Springer International Publishing; 2018. https://doi.org/10.1007/978-3-319-65463-8.

[36] Budden PJ, Sharples JK, Dowling AR. The R6 procedure: Recent developments and comparison with alternative approaches. Int J Press Vessels Pip 2000;77:895–903. https://doi.org/10.1016/S0308-0161(01)00012-6.

[37] Gorji MB, de Pannemaecker A, Spevack S. Machine learning predicts fretting and fatigue key mechanical properties. Int J Mech Sci 2022;215:106949. https://doi.org/10.1016/j.ijmecsci.2021.106949.

[38] Wang H, Li B, Gong J, Xuan F-Z. Machine learning-based fatigue life prediction of metal materials: Perspectives of physics-informed and data-driven hybrid methods. Eng Fract Mech 2023;284:109242. https://doi.org/10.1016/j.engfracmech.2023.109242.

[39] Elber W. The significance of fatigue crack closure. Damage Tolerance in Aircraft Structures, 100 Barr Harbor Drive, PO Box C700, West Conshohocken, PA 19428-2959: ASTM International; 1971, p. 230–42. https://doi.org/10.1520/STP26680S.

[40] BS 7448-1: Fracture mechanics toughness tests - Method for determination of KIc, critical CTOD and critical J values of metallic materials 1991.

[41] ASTM E1820-18: Standard test method for measurement of fracture toughness 2018. https://doi.org/10.1520/E1820-18.

[42] Gómez Gonzáles GL, Antunes FV, Sérgio ER, Vasco-Olmo JM, Díaz FA, Neto DM. A comparison between FEM predictions and DIC results of crack tip displacement field in CT specimens made of titanium. Theor Appl Fract Mech 2023;127:104055. https://doi.org/10.1016/j.tafmec.2023.104055.

[43] Armentani E, Caputo F, Esposito R, Soprano A. Plastic zone size as EPFM parameter. Key Eng Mater 2003;251–252:173–80. https://doi.org/10.4028/www.scientific.net/KEM.251-252.173.

[44] Caputo F, Lamanna G, Soprano A. On the evaluation of the plastic zone size at the crack tip. Eng Fract Mech 2013;103:162–73. https://doi.org/10.1016/j.engfracmech.2012.09.030.

[45] Antunes FV, Ferreira MSC, Branco R, Prates P, Gardin C, Sarrazin-Baudoux C. Fatigue crack growth versus plastic CTOD in the 304L stainless steel. Eng Fract Mech 2019;214:487–503. https://doi.org/10.1016/j.engfracmech.2019.04.013.

[46] Escalero M, Muniz-Calvente M, Zabala H, Urresti I, Branco R, Antunes FV. A methodology for simulating plasticity induced crack closure and crack shape evolution based on elastic-plastic fracture parameters. Eng Fract Mech 2021;241:107412. https://doi.org/10.1016/j.engfracmech.2020.107412.

[47] Zhang W, Chai L, Ren L, Cai L. A unified prediction model for physically small crack and long crack growth based on modified CTOD. Eng Fract Mech 2022;271:108650. https://doi.org/10.1016/j.engfracmech.2022.108650.

[48] Huang X. Constraint-corrected failure assessment diagrams based on crack tip plastic zone size. Eng Fract Mech 2024;309:110403. https://doi.org/10.1016/j.engfracmech.2024.110403.

[49] Newman JC. A crack closure model for predicting fatigue crack growth under aircraft spectrum loading. NASA-TM-81941 1981.

[50] Newman JC. FASTRAN II - A fatigue crack growth structural analysis program. NASA-TM-104159 1992.

[51] Kuhn C, Müller R. A continuum phase field model for fracture. Eng Fract Mech 2010;77:3625–34. https://doi.org/10.1016/j.engfracmech.2010.08.009.

[52] Simoes M, Martínez-Pañeda E. Phase field modelling of fracture and fatigue in shape memory alloys. Comput Methods Appl Mech Eng 2021;373:113504. https://doi.org/10.1016/j.cma.2020.113504.

[53] Li P, Li W, Li B, Yang S, Shen Y, Wang Q, et al. A review on phase field models for fracture and fatigue. Eng Fract Mech 2023;289:109419. https://doi.org/10.1016/j.engfracmech.2023.109419.

[54] Cheng P, Zhuang X, Zhu H, Fish J. Application of s-version finite element method to phase field modeling for localized fractures. Comput Geotech 2023;156:105204. https://doi.org/10.1016/j.compgeo.2022.105204.

[55] Bui TQ, Hu X. A review of phase-field models, fundamentals and their applications to composite laminates. Eng Fract Mech 2021;248:107705. https://doi.org/10.1016/j.engfracmech.2021.107705.

[56] Tang S, Zhang G, Guo TF, Guo X, Liu WK. Phase field modeling of fracture in nonlinearly elastic solids via energy decomposition. Comput Methods Appl Mech Eng 2019;347:477–94. https://doi.org/10.1016/j.cma.2018.12.035.

[57] Tian F, Tang X, Xu T, Li L. An adaptive edge-based smoothed finite element method (ES-FEM) for phase-field modeling of fractures at large deformations. Comput Methods Appl Mech Eng 2020;372:113376. https://doi.org/10.1016/j.cma.2020.113376.

[58] Xing C, Yu T, Sun Y, Wang Y. An adaptive phase-field model with variable-node elements for fracture of hyperelastic materials at large deformations. Eng Fract Mech 2023;281:109115. https://doi.org/10.1016/j.engfracmech.2023.109115.

[59] Kelly PA. Three-dimensional cracks with Dugdale-type plastic zones. Int J Fract 2000;106:291–309. https://doi.org/10.1023/A:1026557509000.

[60] Yamashita K, Gotoh K. A study on the strip yield model for a surface crack. Jpn Soc Nav Archit Ocean Eng 2016;22:433–8. (in Japanese)

[61] Jin Z, Wang X. Point load weight functions for semi-elliptical cracks in finite thickness plate. J ASTM Int 2012;9:1–14. https://doi.org/10.1520/JAI103962.

[62] Wang X, Glinka G. Determination of approximate point load weight functions for embedded elliptical cracks. Int J Fatigue 2009;31:1816–27. https://doi.org/10.1016/j.ijfatigue.2008.12.002.

[63] Toyosada M, Niwa T. Fatigue life prediction of steel structures. Kyoritsu Shuppan Co., Ltd.; 2001. (in Japanese)

[64] Toyosada M, Tanaka K, Matsumoto K, Tanaka S, Osawa N. Study on equivalent distributed stress determination technique based on generalized matrix inversion (part 1): Analysis of two-dimensional edge cracks based on the center cracked plate's weight function. Jpn Soc Nav Archit Ocean Eng 2020;31:213–28. (in Japanese) https://doi.org/10.2534/jjasnaoe.31.213.

[65] Glinka G. Development of weight functions and computer integration procedures for calculating stress intensity factors around cracks subjected to complex stress fields. Hampton, VA 23666, USA: 1996.

[66] Sih GC. Handbook of stress-intensity factors: Stress-intensity factor solutions and formulas for reference. vol. 2. Lehigh University, Institute of Fracture and Solid Mechanics; 1973.

[67] Adi Ben-Israel, Thomas NE Greville. Generalized inverses. New York: Springer-Verlag; 2003. https://doi.org/10.1007/b97366.

[68] Golub GH, Reinsch C. Singular value decomposition and least squares solutions. Numer Math (Heidelb) 1970;14:403–20. https://doi.org/10.1007/BF02163027.

[69] Paris PC. The mechanics of fracture propagation and solutions to fracture arrestor problems. Document D2-2195, The Boeing Company 1957.

[70] Kronrod AS. Nodes and weights of quadrature formulas. Sixteen-place tables, New York: Consultants Bureau; 1965.

[71] Favati P, Lotti G, Romani F. Algorithm 691: Improving QUADPACK automatic integration routines. ACM Transactions on Mathematical Software 1991;17:218–32.

[72] Htut ZL, Osawa N, Tanaka S, Kyaw PM, Toyosada M. Study on equivalent distributed stress determination technique based on generalized matrix inversion (part 2). Proc Jpn Soc Nav Archit Ocean Eng, Kobe: 2022, p. 757–63.

[73] Htut ZL, Osawa N, Tanaka S, Toyosada M. Efficient technique for evaluation of three-dimensional elastic-plastic fracture mechanics parameters based on equivalent distributed stress concept. Theor Appl Fract Mech 2024;131:104357. https://doi.org/10.1016/j.tafmec.2024.104357.

[74] Wang CH, Rose LRF, Newman JC. Closure of plane-strain cracks under large-scale yielding conditions. Fatigue Fract Eng Mater Struct 2002;25:127–39. https://doi.org/10.1046/j.8756-758x.2002.00483.x.

[75] Sneddon IN. The distribution of stress in the neighbourhood of a crack in an elastic solid. Proc R Soc Lond A Math Phys Sci 1946;187:229–60. https://doi.org/10.1098/rspa.1946.0077.

[76] Keer LM, Mura T. Stationary crack and continuous distributions of dislocations. Proc First Int Conf Fract, Sendai, Japan: The Japanese Society for Strength and Fracture of Materials (JSFM); 1965.

[77] Akiniwa Y, Tanaka K, Kimura H, Kogoshi M. Evaluation of fatigue strength of cracked components based on analysis of plasticity-induced crack closure. Trans Jpn Soc Mech Eng, Ser A 2001;67:1364–71. (in Japanese) https://doi.org/10.1299/kikaia.67.1364.

[78] Sneddon IN. Fourier transforms. McGraw-Hill, New York: 1951.

[79] Lin XB, Smith RA. Finite element modelling of fatigue crack growth of surface cracked plates. Eng Fract Mech 1999;63:523–40. https://doi.org/10.1016/S0013-7944(99)00041-7.

[80] Brighenti R, Carpinteri A. Surface cracks in fatigued structural components: A review. Fatigue Fract Eng Mater Struct 2013;36:1209–22. https://doi.org/10.1111/ffe.12100.

[81] Li Z, Jiang X, Hopman H. Surface crack growth in offshore metallic pipes under cyclic loads: A literature review. J Mar Sci Eng 2020;8:339. https://doi.org/10.3390/jmse8050339.

[82] Müller H, Müller S, Munz D, Neumann J. Extension of surface cracks during cyclic loading. Fracture Mechanics: Seventeenth Volume, ASTM International100 Barr Harbor Drive, PO Box C700, West Conshohocken, PA 19428-2959; 1986, p. 625–43. https://doi.org/10.1520/STP17420S.

[83] Brickstad B, Sattari-Far I. Crack shape developments for LBB applications. Eng Fract Mech 2000;67:625–46. https://doi.org/10.1016/S0013-7944(00)00077-1.

[84] Feng L, Qian X. An adaptive learning approach to determine and update crack sizes from strain relaxation data for welded plate joints. Eng Fract Mech 2022;259:108165. https://doi.org/10.1016/j.engfracmech.2021.108165.

[85] Huang C, Chen T, Xia Z, Jiang L. Numerical study of surface fatigue crack growth in steel plates repaired with CFRP. Eng Struct 2022;268:114743. https://doi.org/10.1016/j.engstruct.2022.114743.

[86] Healy B, Gullerud A, Koppenhoefer K, Roy A, RoyChowdhury S, Petti J, et al. WARP3D-release 18.2.0: 3-D dynamic nonlinear fracture analyses of solids using parallel computers. 2020.

[87] Htut ZL, Osawa N, Tanaka S. Modified enhanced approach for determining the elastic-plastic fracture mechanics parameters of 3D surface cracks. Proc 36th Asian-Pac Tech Exch Advis Meet Mar Struct (TEAM), Busan, South Korea: 2023.

[88] Htut ZL, Osawa N, Tanaka S, Toyosada M. Application of equivalent distributed stress concept and modified cohesive zone model in elastic-plastic fracture mechanics analysis of surface cracks. Eng Fract Mech 2025;315:110813. https://doi.org/10.1016/j.engfracmech.2025.110813.

[89] MSC. Marc 2021 User's Guide. Hexagon Co., Ltd.; 2021.

[90] TSV-Crack V6.6 Manual Rev1. TechnoStar Co., Ltd.; 2016.

[91] Okada H, Kawai H, Araki K. A virtual crack closure-integral method (VCCM) to compute the energy release rates and stress intensity factors based on quadratic tetrahedral finite elements. Eng Fract Mech 2008;75:4466–85. https://doi.org/10.1016/j.engfracmech.2008.04.014.

[92] Okada H, Kawai H, Tokuda T, Fukui Y. Fully automated mixed mode crack propagation analyses based on tetrahedral finite element and VCCM (virtual crack closure-integral method). Int J Fatigue 2013;50:33–9. https://doi.org/10.1016/j.ijfatigue.2012.04.009.

[93] Newman JC, Raju IS. Stress-intensity factor equations for cracks in three-dimensional finite bodies subjected to tension and bending loads. NASA-TM-85793 1984.

[94] Toyosada M, Gotoh K. Physical meaning of the fictitious crack opening displacement in Dugdale model. 11th Int Conf Fract, ICF11, Turin, Italy: 2005.

[95] Walters MC, Paulino GH, Dodds RH. Interaction integral procedures for 3-D curved cracks including surface tractions. Eng Fract Mech 2005;72:1635–63. https://doi.org/10.1016/j.engfracmech.2005.01.002.

[96] Gadallah R, Osawa N, Tanaka S. Evaluation of stress intensity factor for a surface cracked butt welded joint based on real welding residual stress. Ocean Eng 2017;138:123–39. https://doi.org/10.1016/j.oceaneng.2017.04.034.

[97] Kyaw PM, Osawa N, Gadallah R, Tanaka S. Accurate and efficient method for analyzing mixed-mode SIFs for inclined surface cracks in semi-infinite bodies by using numerical influence function method. Theor Appl Fract Mech 2020;106:102471. https://doi.org/10.1016/j.tafmec.2019.102471.

[98] Htut ZL, Osawa N, Tanaka S. Comprehensive investigation of plastic zone size and crack tip opening displacement of surface cracks at the corner point using the equivalent distributed stress-based cohesive zone model. Proc 35th Int Ocean Polar Eng Conf (ISOPE), Seoul, South Korea: 2025, p. 3504–11.

[99] Htut ZL, Osawa N, Tanaka S. Introduction of crack closure assessment of surface cracks in butt joints based on equivalent distributed stress concept considering residual stress. Proc 77th IIW Annu Assem Int Conf, Rhodes, Greece: 2024.

[100] Olesiak Z, Wnuk M. Plastic energy dissipation due to a penny-shaped crack. Int J Fract Mech 1968;4:383–96. https://doi.org/10.1007/BF00186804.

PUBLICATIONS

Publications with Full or Peer Review

1. **Htut ZL**, Osawa N, Tanaka S, Toyosada M. Efficient technique for evaluation of three-dimensional elastic-plastic fracture mechanics parameters based on equivalent distributed stress concept. Theor Appl Fract Mech 2024;131:104357.

2. **Htut ZL**, Osawa N, Tanaka S, Toyosada M. Application of equivalent distributed stress concept and modified cohesive zone model in elastic-plastic fracture mechanics analysis of surface cracks. Eng Fract Mech 2025;315:110813.

3. **Htut ZL,** Osawa N, Tanaka S. Comprehensive investigation of plastic zone size and crack tip opening displacement of surface cracks at the corner point using the equivalent distributed stress-based cohesive zone model. Proc 35th Int Ocean Polar Eng Conf (ISOPE), Seoul, South Korea: 2025, p. 3504–11.

Conference Proceedings

1. **Htut ZL**, Osawa N, Tanaka S, Kyaw PM, Toyosada M. Study on equivalent distributed stress determination technique based on generalized matrix inversion (part 2). Proc Jpn Soc Nav Archit Ocean Eng, Kobe: 2022, p. 757–63.

2. **Htut ZL**, Osawa N, Tanaka S. Modified enhanced approach for determining the elastic-plastic fracture mechanics parameters of 3D surface cracks. Proc 36th Asian-Pac Tech Exch Advis Meet Mar Struct (TEAM), Busan, South Korea: 2023.

3. **Htut ZL**, Osawa N, Tanaka S. Introduction of crack closure assessment of surface cracks in butt joints based on equivalent distributed stress concept considering residual stress. Proc 77th IIW Annu Assem Int Conf, Rhodes, Greece: 2024.